DUCTILE PHASE REINFORCED BULK METALLIC GLASS COMPOSITES FORMED BY CHEMICAL PARTITIONING

Thesis by

Choongnyun Paul Kim

In Partial Fulfillment of the Requirements

for the Degree of

Doctor of Philosophy

California Institute of Technology

Pasadena, California

2001

(Defended May 25, 2001)

To my parent,

and

Jessica and Nicole

ACKNOWLEDGEMENTS

First of all, I give all my thanks to God for everything.

Then I give my deepest appreciation to my research advisor, Professor William L. Johnson, for giving me continuous inspiration and encouragement during my entire life at Caltech. I am so thankful to him for giving me a chance to join his group and support me in many ways. His exceptional scientific enthusiasm and optimism always kept me moving ahead. He has always been my unending source of inspiration, support, and encouragement. Also, I couldn't forget the precious moments shared together daily on the roof of Keck laboratory building.

My work would not be possible without the support from many individuals. I owe lots of love to all of my professors, colleagues, and friends at Caltech. Professors Fultz, Ustundag, McGill, and Ravichandran were on my Ph.D candidacy exam committee, and I thank them for guidance on research and academic discussions as well as class lectures. I appreciate all of Professor Johnson's group members and other people in the Keck laboratory for their friendship, cooperation in the labs and many discussions on various topics. A partial list would include Drs. Jan Schroers, Sven Bossuyt, Haein Choi-Yim, Joerg Loeffler, Ralf Busch, Stephen Glade, and Andy Waniuk, Hyonjee Lee, Seungyub Lee, Pam Albertson, and many others. I appreciate Dr. Choi-Yim for friendship and fruitful discussions on various topics.

Drs. Peker, Lin, Tenhover, and Lee are the ones who gave me challenging projects and fruitful academic advises and discussions while I was working with them at Liquidmetal Technologies. Dr. Peker first introduced me to metallic glasses in 1995. He influenced me to change my career path from electrical engineer to material scientist. It has been a great time working with him.

I appreciate the co-authors on published papers; Dr. Frigyes Szuecs on mechanical tests, Dr. Evgenia Pekarskaya on TEM works, and Dr. Chuck Hays on composite development. I thank them for their friendship and cooperation.

Also, I would like to express my extreme gratitude to the staff and management of Liquidmetal Technologies and Liquidmetal Golf, especially Mr. James Kang and his family. I appreciate James Kang for helping me in many ways and for his patience in finishing my thesis.

The financial support from the U.S. Army Research Office under grant number DAAG55-98-1-0305, the Air Force Office of Scientific Research under grant number F49620-97-1-0323, the U.S. Department of Energy under grant number DEFG-03-86ER45242, and the National Science Foundation under grant number DMR-0080065 are greatly appreciated.

Finally, I would like to express my deepest gratitude to my family. I would not be where I am today without the support of them. Especially, I thank my lovely wife, Jessica, for being with me and sharing together all the moments. I thank my parents for unconditional love and support. My daughter, Nicole, makes my life more meaningful and thankful. Also, I thank my mother-in-law for taking care of Nicole.

ABSTRACT

A new class of ductile metal reinforced bulk metallic glass matrix composite material has been prepared that demonstrates improved mechanical properties. This newly designed material exhibits both improved toughness and large plastic strain to failure. Primary dendrite growth accompanied by solute partitioning in the molten state yields an equilibrium microstructure consisting of a ductile crystalline Ti-Zr-Nb β phase, with the bcc-structure, in a Zr-Ti-Nb-Cu-Ni-Be bulk metallic glass matrix processed via in situ processing. Under mechanical loading, the microstructure imposes constraints on the glassy matrix that leads to the generation of highly organized shear band patterns throughout the sample. This results in a dramatic increase in the plastic strain to failure, impact resistance, and toughness of the metallic glass. This thesis shows how microstructural inhomogeneity can be used to control the initiation and propagation of localized shear bands in metallic glasses under a variety of unconstrained loading conditions. A series of mechanical property tests were conducted on composite materials. These include quasi-static tensile and compression tests, Charpy impact, and three point bend tests on specimens prepared according to ASTM standards. Also, *in situ* straining transmission electron microscopy (TEM) experiments were performed to study the propagation of the shear bands in the bulk metallic glass based composite.

TABLE OF CONTENTS

LIST OF FIGURES

LIST OF TABLES

Chapter 1. Introduction

1.1 Metallic Glasses

1.1.1 Definition of Metallic Glasses

There are two completely distinct mechanisms by which a liquid can solidify upon cooling: it can crystallize and form a crystalline solid, or it can vitrify and form a glass. Crystallization is accompanied by a sharp volume change as the atoms rearrange themselves into a periodic array. As the temperature is reduced, the volume contracts continuously until the equilibrium melting temperature T_m is reached; at this point isothermal crystallization may occur as heat is extracted from the material. When crystallization is complete, the temperature can continue to fall, resulting in a further volume decrease due to thermal contraction.

If crystallization does not occur at T_m, then the liquid can simply continue to cool as a supercooled liquid. The volume of the liquid continues to decrease in a smooth fashion as the temperature is lowered below T_m. The viscosity increases as the liquid is cooled further. Eventually a temperature range is reached at which the viscosity of the liquid increases very sharply to a value so high (~ 10^{13} poises) that viscous flow or atoms rearrangement in the glass is negligible.[1] Below this temperature, called glass transition temperature T_g, the supercooled liquid acts like a solid and is referred to as a glass even though the internal structure is still completely amorphous and liquidlike. Once the atoms are effectively frozen into position, the thermal contraction of the glass is about the same as that of the crystalline solid, since

now upon further cooling there is no atom rearrangement in the glass similar to that taking place in the liquid. The value T_g depends on the rate of cooling. Fig. 1.1. shows the volume-temperature relationship for the solidification of a liquid into either a crystal or a glass.[2]

Metallic glasses are metastable alloys which have the atomic structure of the liquid alloys and can be formed when crystallization is suppressed. Metallic glass is a noncrystalline metallic solid lacking long-range periodicity of the atomic arrangement. The atomic structure of metallic glasses has the randomness similar to that of a liquid. Extremely high cooling rates (on the order of 10^6 K/sec) or control of potent heterogeneous nucleation sites at slow cooling are normally required to produce metallic glasses, so that the disordered atomic configuration of the liquid state can be frozen in.

The thermodynamic variables such as volume, entropy and enthalpy are continuous through the glass transition, but exhibit a change of slope there. This implies that at T_g there should be a discontinuity in derivative variables such as heat capacity ($C_p = (\partial H/\partial T)_p$) and thermal expansivity ($\alpha_T = \partial \ln V/\partial T$). Fig. 1.2 shows the heat capacity curves of a glass, the corresponding liquid and crystalline solid as a function of temperature.[3] The sudden increase in the heat capacity of the glass upon heating is the thermal manifestation of the glass transition. The glass transition is the phenomenon in which a solid amorphous phase exhibits a more or less abrupt change in derivative thermodynamic properties such as heat capacity or thermal expansivity, from the crystalline state values to those values for the liquid state with change of temperature.

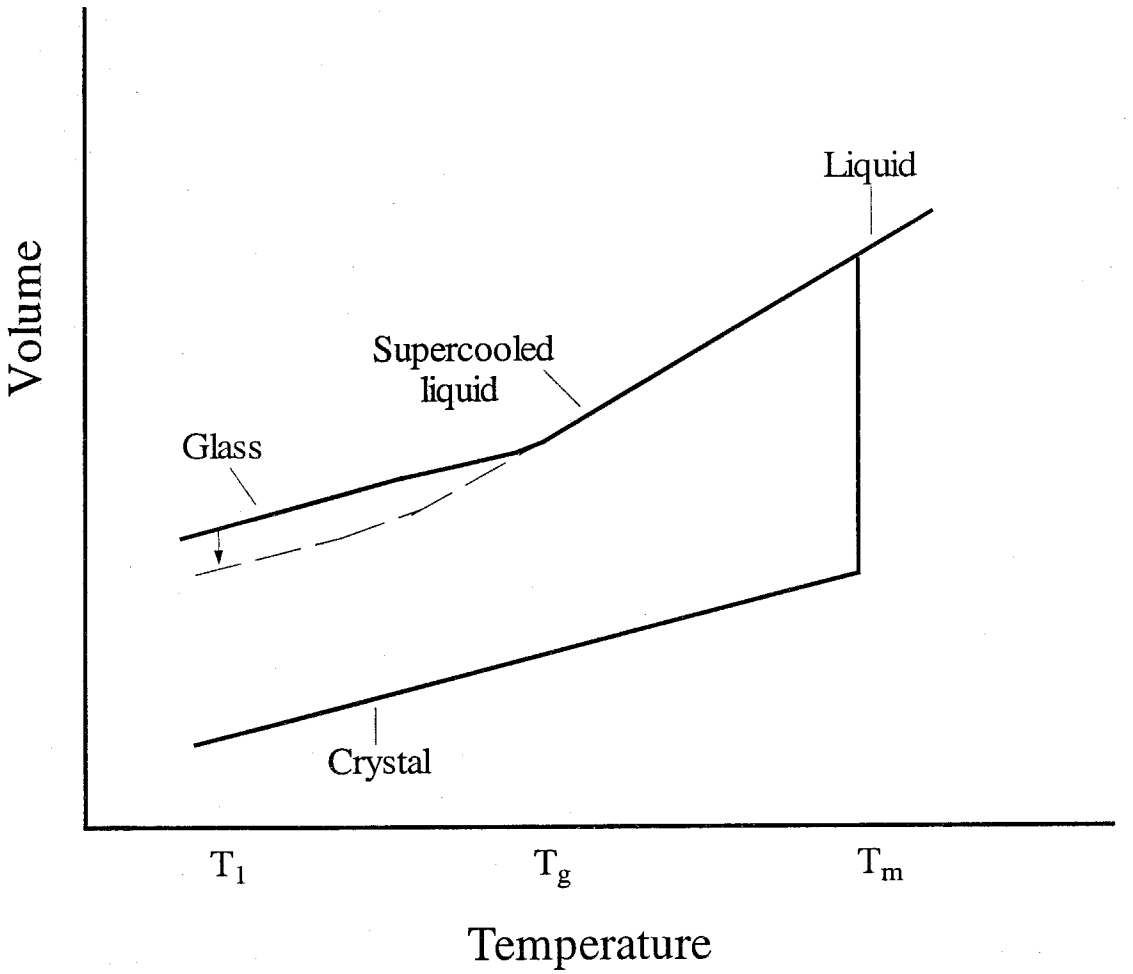

Fig. 1.1. Schematic illustration of the change in volume with temperature as an undercooled liquid is cooled through the glass transition temperature T_g. The vertical arrow illustrates the volume change accompanying the structural relaxation or stabilization of the glass if held at temperature T_l. Reproduced from ref. 2.

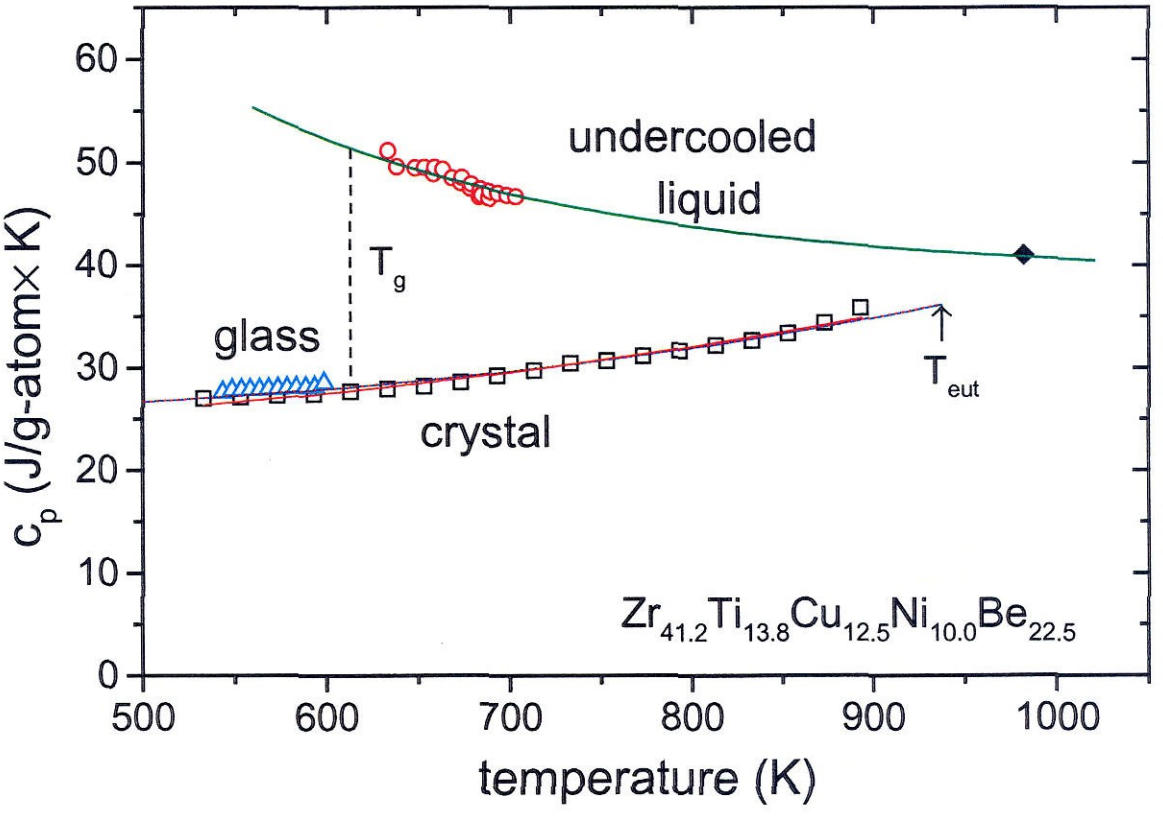

Fig. 1.2. Heat capacity curves of the $Zr_{41.2}Ti_{13.8}Cu_{12.5}Ni_{10}Be_{22.5}$ "Vitreloy 1" alloy. The corresponding liquid and crystalline solid represented as a function of temperature. Reproduced from ref. 3.

The glass transition temperature, T_g[4], is defined as the point of inflection of the rising heat capacity. The temperature of the glass transition is not a constant of the material, but is a function of experimental conditions. Thus, slower cooling rates will move the glass transition temperature to a lower temperature.

When the viscosity is about 10^{13} poise at the glass transition temperature T_g, the atomic configuration of the liquid becomes homogeneously frozen. Above the glass transition region and the below the melting point, the material is an undercooled liquid which is metastable with respect to crystallization, but is in internal equilibrium. Below this region, it is a glass which is in a nonequilibrium state. Fig. 1.3 shows the viscosity of the undercooled liquid as a function of temperature.[1] It depicts the viscosity in the entire range from glass transition to the melting point. At T_g, viscosity reaches 10^{13} poise.

1.1.2 Historical Background and Development of Bulk Metallic Glasses

The first liquid-metal alloy vitrified by cooling from the molten state to the glass transition as a result of developing rapid quenching techniques for chilling metallic liquids at very high rates of 10^5 ~ 10^6 K/sec was Au_{75} Si_{25}, as reported by Klement, Willens, and Duwez at Caltech in 1960.[5] Since Duwez et al. first reported the metallic glass formation from the liquid state, numerous glass forming alloys have been discovered. These metallic glasses result from their amorphous structure have unique mechanical, electrical, magnetic, and corrosion behavior.[6]

These metallic glasses have unique properties which are different from corresponding crystalline materials. Low coercive magnetic force and relative high

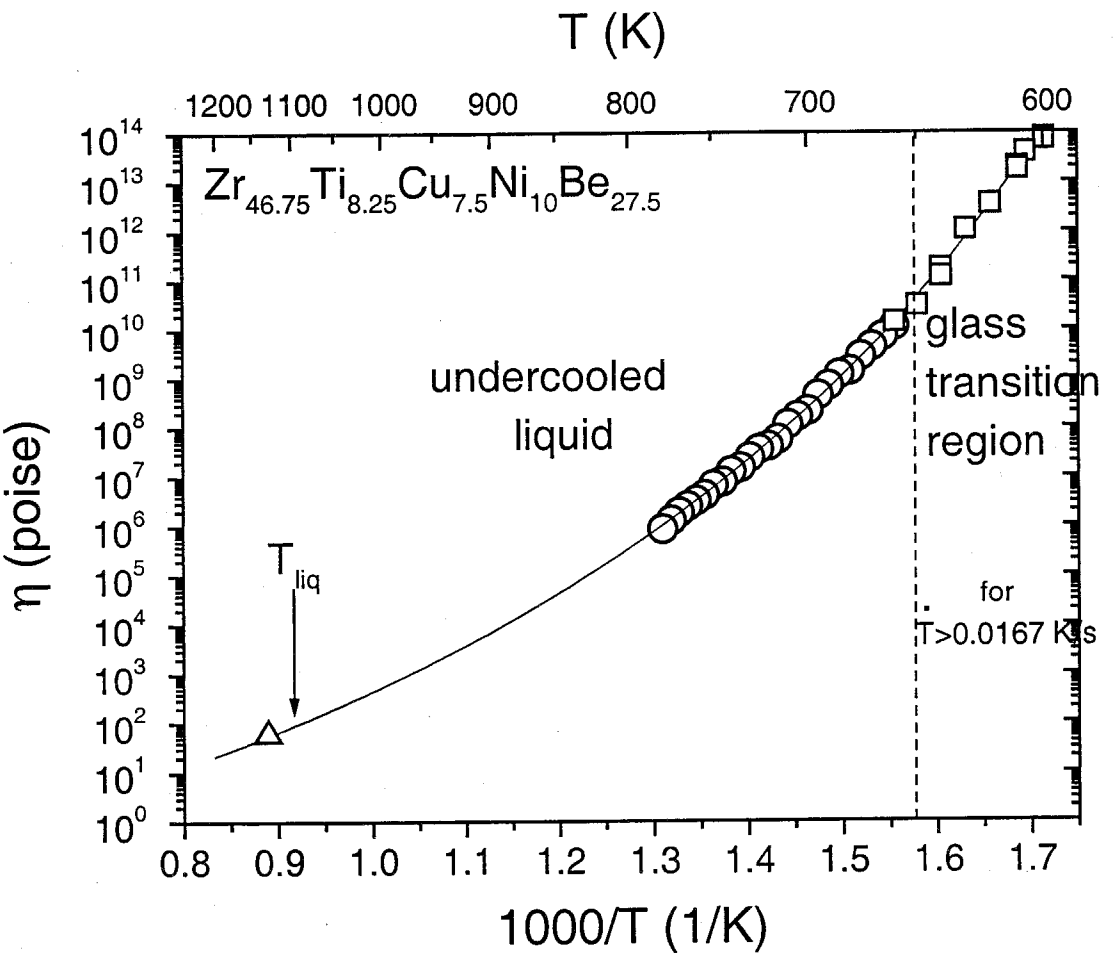

Fig. 1.3. Equilibrium viscosity as a function of temperature for the undercooled liquid of $Zr_{46.75}Ti_{8.25}Cu_{7.5}Ni_{10}Be_{27.5}$ "Vitreloy 4" alloy. Reproduced from ref. 1.

permeability, combined with very high mechanical hardness and tensile strength, make Fe and Ni based glasses excellent material for power transformer cores and transducers.[7] The particular Fe-Cr-P-C alloy have extraordinarily high corrosion resistance in a hostile environment.[8] This makes them excellent coating materials. The low melting temperatures of glass forming alloys make ductile amorphous foil excellent filler for accurate brazing and hardness, and close-to-theoretical-limit high strength attract applications as structure materials. However, these alloys required very high cooling rates of 10^5 ~ 10^6 K/sec to suppress crystallization and form a glass. The high critical cooling rates limit the dimension of the samples to thin sheets or ribbons. The field of metallic glasses gained momentum in the early 1970's when researchers at Allied Chemical Corporation developed continuous casting processes for commercial manufacture of metallic glass ribbons and sheets.[9] The small thickness of the metallic glass sheets limited the number of practical applications.

In 1974, Chen and collaborators used simple suction casting methods to form millimeter rods of ternary Pd-Cu-Si alloys at significantly lower cooling rates in the range of 10^3 K/sec.[10] In 1982, Drehman, Greer, and Turnbull reported the formation of a metallic glass as a bulk sample carrying out experiments on Pd-Ni-P alloy melts using a boron oxide fluxing to dissolve heterogeneous nucleants into a glassy surface coating.[11,12] The fluxing experiments showed that when heterogeneous nucleation was suppressed, this ternary alloy would form bulk glass ingots of a centimeter size at cooling rates in the 10 K/sec ranges.

In early 1990's, bulk metallic glass formation without fluxing became possible

by judicious choice of the compositions at deep eutectics in multicomponent alloy systems. Inoue and his coworkers investigated the fabrication of a large variety of alloys such as La-Ni-Al[13], Mg-Cu-Y[14], and Zr-Cu-Ni-Al.[15] These alloy systems have critical cooling rates of 100 K/sec for glass formation and exhibit good thermal stability above the glass transition. By casting the alloys into copper molds, glassy rods and bars with cast thickness of several mm's. These multicomponent glass forming alloys illustrated that bulk glass forming was far more ubiquitous than previously thought, and not confined to exotic Pd-base alloys. The work opened the door to the development of broad range of bulk metallic glasses.

In 1993, Peker and Johnson at Caltech discovered the exceptionally good glass forming alloy systems based on higher order alloys of Zr-Ti-Cu-Ni-Be.[16] This particular $Zr_{41.2}Ti_{13.8}Cu_{12.5}Ni_{10}Be_{22.5}$, "Vitreloy 1" alloy, exhibits a critical cooling rate of 1 K/sec, and direct measurements of the TTT diagram of this alloy placed the "nose" of the nucleation curve for bulk samples at time scales of the order of 100 seconds.[17] The alloys can be cast by conventional metallurgical casting methods in the form of fully glassy rods with diameters ranging up to 5 ~ 10 cm without fluxing or special processing treatments. Also, the remarkable glass forming ability of Vitreloy 1 alloy enables casting commercially large plates and golf products at Howmet Corporation in Michigan, and Liquidmetal Technologies in Lake Forest, California, and has led to commercialization of bulk metallic glasses and metallic glass matrix composites in many applications. Fig. 1.4 shows the T-T-T diagram of Vitreloy 1.

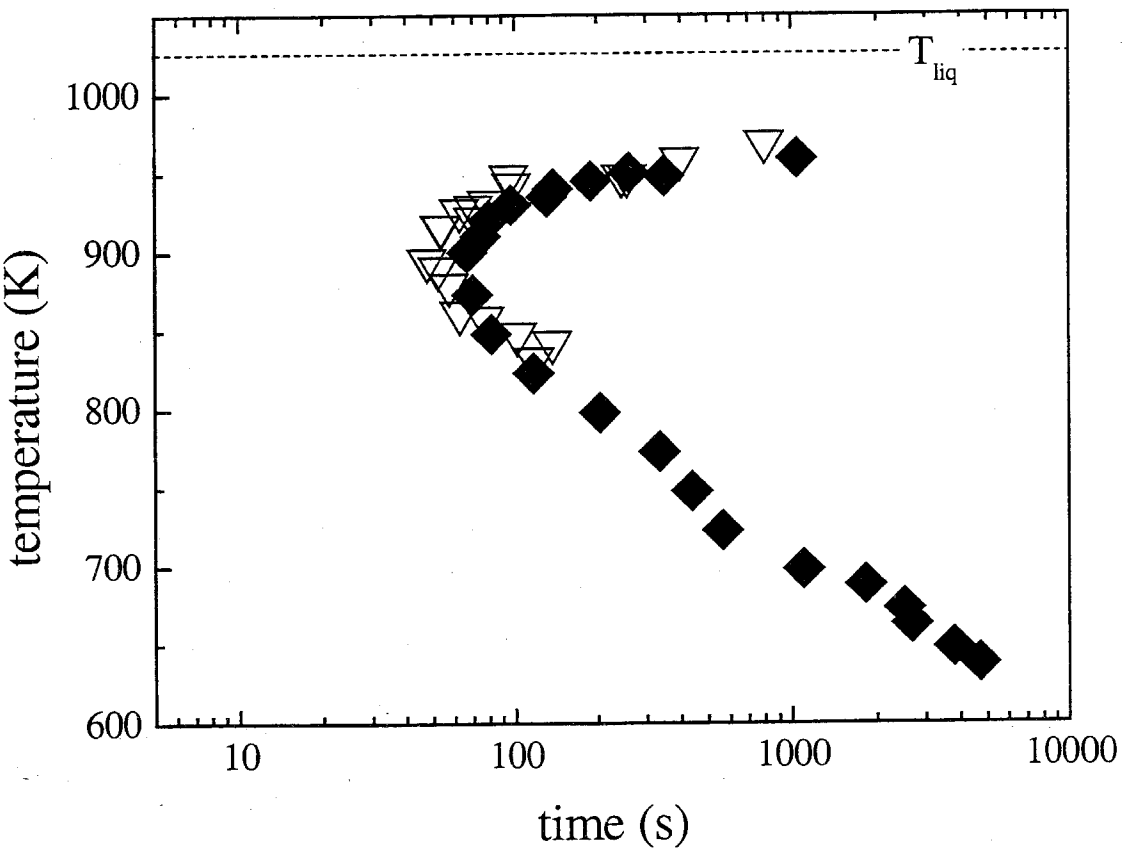

Fig. 1.4. T-T-T diagram of $Zr_{41.2}Ti_{13.8}Cu_{12.5}Ni_{10}Be_{22.5}$ "Vitreloy 1" alloy.

Reproduced from ref. 17.

More recently, Lin and Johnson found new bulk metallic glasses such as Cu-Ti-Zr-Ni[18] and Zr-Ti(Nb)-Cu-Ni-Al[19] with critical thickness of amorphous samples near 1 centimeter. The best Cu-Ti-Zr-Ni amorphous alloy is $Cu_{47}Ti_{34}Zr_{11}Ni_8$, Vit 101. It can be cast at least 4 ~ 6 mm thick. Two of the most highly processible of the Zr-Ti(Nb)-Cu-Ni-Al amorphous alloys are $Zr_{52.5}Ti_5Cu_{17.9}Ni_{14.6}Al_{10}$, Vit105 and $Zr_{57}Nb_5Cu_{15.4}Ni_{12.6}Al_{10}$, Vit106. Glassy ingots of 1 cm thickness can be produced with the estimated critical cooling rate of 10 K/s.[19]

1.2 History of Metallic Glass Matrix Composites

Metallic glass ribbon has been used as a reinforcement in a composite material because of its high strength and high elastic strain limit. An amorphous metal ribbon reinforced resin-matrix composite was fabricated and mechanically tested by Strife et al.[20] These composites are found to have high strength and good fracture toughness, but poor fatigue resistance. Metallic glass ribbon has also been used as a reinforcement in polymer and glass ceramic matrices.[21,22] The first metallic glass ribbon reinforced metal matrix composites were reported by Cytron.[23] $Ni_{60}Nb_{40}$ metallic glass ribbon was chosen as a reinforcement because of its ductility and high crystallization temperature (650 °C). This metallic glass ribbon was hot pressed between wafers of superplastic aluminum alloy at 450-500 °C to form the composite.

Metallic glass ribbon has also been used as a matrix. Usually the melt spinning technique is used to make composites in a ribbon form. Adding tungsten carbide particles to $Ni_{78}Si_{10}B_{12}$ metallic glass ribbon during the melt-spinning process was done by Kimura et al.[24]

In addition to being used to fabricate particulate reinforced metallic glass ribbons, melt spinning process has been used to make discontinuous fiber reinforced composites.[25] However, the resulting fiber distribution was poor. Williford et al. described the technique to make continuous fiber reinforced metallic glass ribbons.[26] They arranged fibers in contact with the meniscus of molten metal protruding from the crucible orifice. The fibers were then drawn out along with the melt onto the moving substrate. The combination was chilled to form the composite. However, the best results were ribbons reinforced by a few tungsten wires. In addition, small dimension of these metallic glass ribbon composites limits a number of practical applications.

Recently bulk metallic glasses were used as matrices reinforced with refractory ceramics, ductile metal particles, or short wires.[27-31] Those reinforcements include ceramics such as SiC, TiC, or WC. Ductility in compression and tension as well as fracture toughness was improved substantially by adding metallic particles and wires into the metallic glass. Metals like W and Ta were also used. Improvements of the mechanical properties are obtained by hindering propagation of shear bands and encouraging the formation of multiple shear bands due to the existence of the second crystalline phase. This was made possible by the use of recently reported multicomponent alloys that exhibit an extremely high glass forming ability. Bulk glassy material with thickness up to several cm could be produced, since they have low critical cooling rates. They usually are at deep eutectic composition. That means they have low melting temperature. Accordingly, these alloys can be used in liquid-phase processing at lower temperature. This lowers the cost of processing and reduces the chemical interactions between the reinforcement and the glass. This makes for an easy control of interfacial reactions. In addition, the low glass transition temperature decreases

differential thermal stresses which arise between the reinforcement and the matrix during cooling. Further, these alloys are stable against crystallization above the glass transition temperature as an undercooled liquid. This allows for the processing at even lower temperatures slightly above the glass transition, although higher pressures would be required due to the higher viscosity.

1.3 Kinetics of Phase Transformation

1.3.1 Nucleation

An understanding of the mechanism of solidification and how it is affected by such parameters as temperature distribution, cooling rate and alloying, is important in the control of mechanical properties of cast alloys.

The liquid has a higher Gibbs free energy than the crystal below the equilibrium melting temperature (T_m) as shown on Fig.1.5. If a liquid is cooled below its equilibrium melting temperature, there is a driving force for the nucleation of crystal (G_L - G_S), and it might be expected that the liquid phase would spontaneously solidify. However, this is not always the case if a liquid is undercooled (or supercooled) to below T_m and held there indefinitely without any transformation occurring. The reason for this behavior is that the transformation begins by the

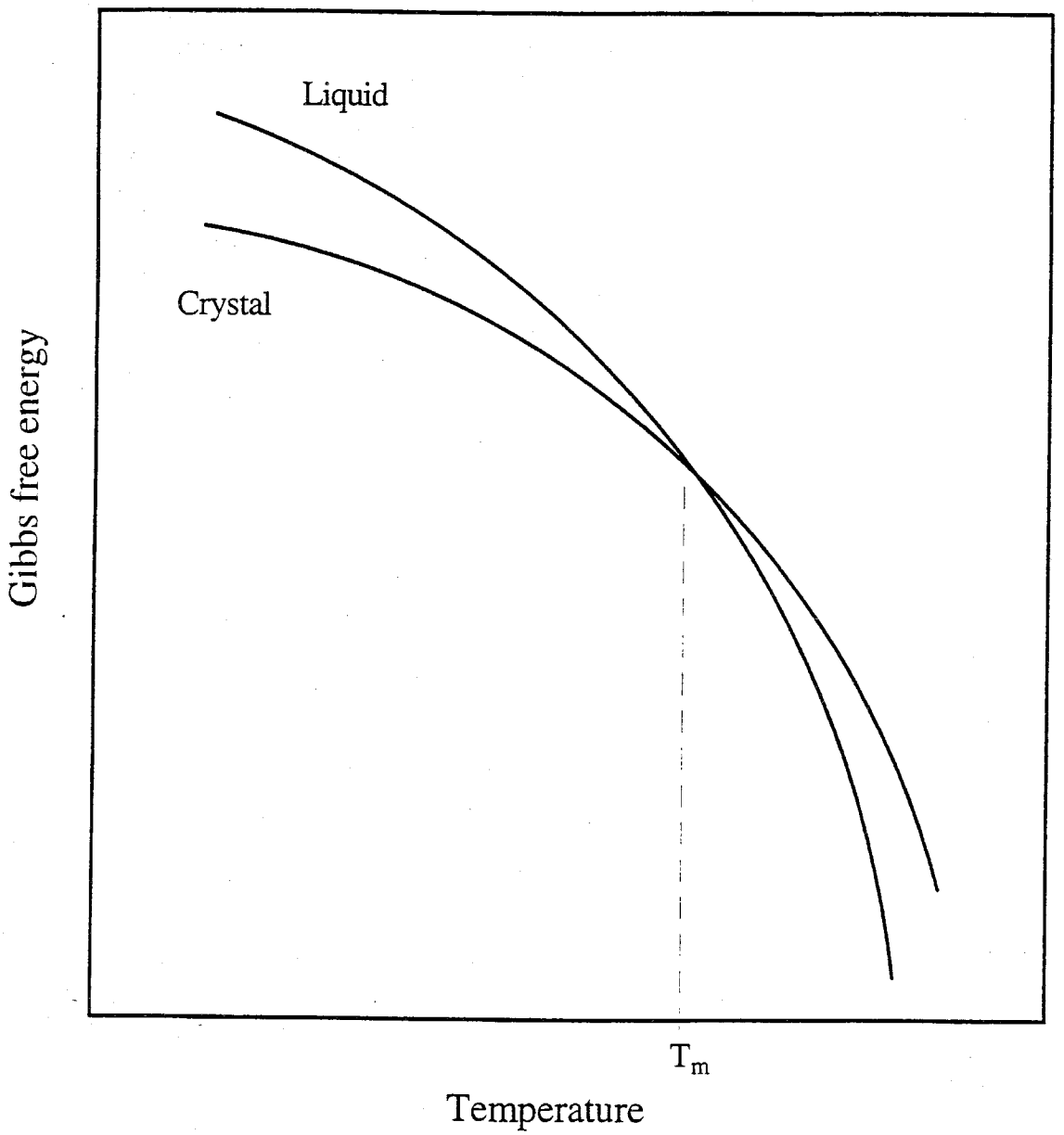

Fig. 1.5. Gibbs free energy curves for liquid and corresponding crystal with respect to the temperature.

formation of very small solid particles or nuclei. The large undercooling is only obtained when no heterogeneous nucleation sites are available, i.e., when solid nuclei must form homogeneously from the liquid.

An undercooled liquid is a thermodynamically metastable phase comparing to the corresponding equilibrium crystalline phases. This undercooled liquid is not in the lowest energy state and it will crystallize at a high enough temperature and/or given long enough time. According to the classical homogeneous nucleation theory,[32,33] the free energy change upon nucleation is given by the following two terms: (1) the free energy decrease due to the transformation of the liquid to crystal which is proportional to the volume of the embryo; (2) the free energy increase due to the creation of a liquid-crystal interface, which is proportional to the surface area of the embryo.

1.3.2 Homogeneous Nucleation

Consider a given volume of liquid at a temperature ΔT below T_m with a free energy G_1, Fig. 1.6.a.[34] If some of the atoms of the liquid cluster together to form a small sphere of solid, Fig. 1.6.b, the free energy of the system will change to G_2 given by

$$G_2 = V_S G_V^S + V_L G_V^L + A_{SL}\sigma$$

where V_S is the volume of the solid sphere, V_L the volume of liquid, A_{SL} is the solid/liquid interfacial area, G_V^S and G_V^L are the free energies per unit volume of solid and liquid respectively, and σ the solid/liquid interfacial free energy. The free energy

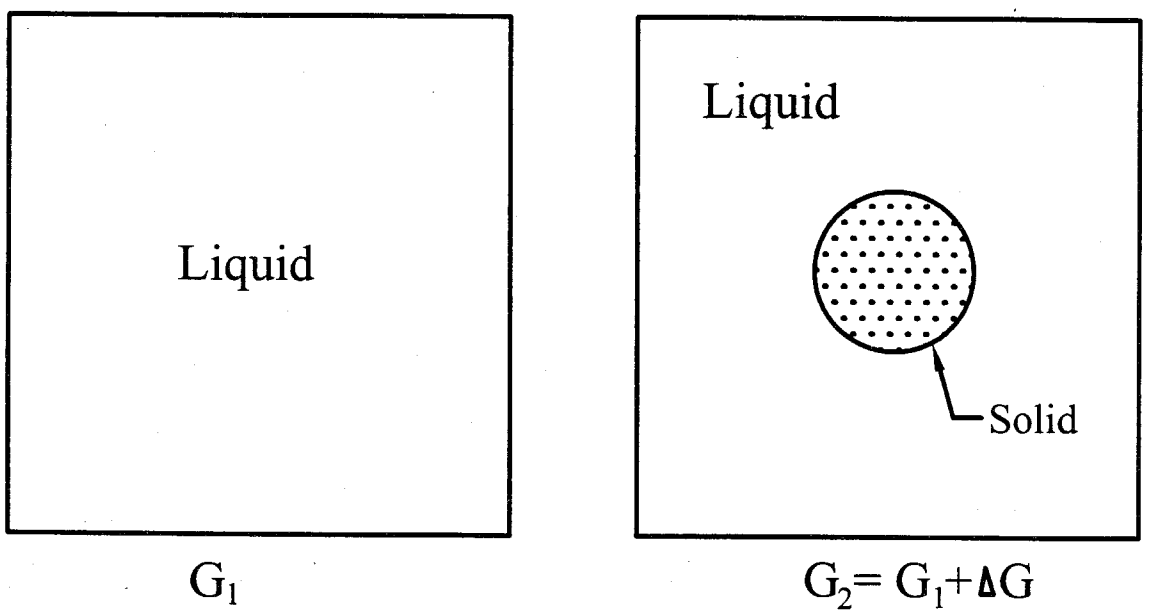

Fig. 1.6. Homogeneous nucleation. Reproduced from ref. 34.

of the system without any solid present is given by $G_1 = (V_S + V_L)\, G_V^L$. The formation of solid therefore results in a free energy change $\Delta G = G_2 - G_1$, where

$$\Delta G = - V_S \Delta G_V + A_{SL}\sigma \text{ and } \Delta G_V = G_V^L - G_V^S.$$

For an undercooling ΔT, $\Delta G_V = L_V \Delta T / T_m$ where L_V is the latent heat of fusion per unit volume. Below T_m, ΔG_V is positive so that the free energy change associated with the formation of a small volume of solid has a negative contribution due to the lower free energy of a bulk solid. However, there is also a positive contribution due to the creation of a solid/liquid interface. The excess free energy associated with the solid particle can be minimized by the correct choice of particle shape. The total Gibbs' free energy change associated with the formation of a spherical crystalline embryo with radius r is given by

$$\Delta G = 4\pi r^2 \sigma + \frac{4\pi}{3} r^3 \Delta G_v$$

In Fig.1.7, ΔG is shown as a function of embryo radius r. Below the melting point, interfacial energy σ and volume free energy ΔG_V will compete as r increases. Since the interfacial term increases as r^2 whereas the volume free energy released only increases as r^3, the creation of small particles of solid always leads to a free energy increase. It is this increase that is able to maintain the liquid phase in a metastable state almost indefinitely at temperature below T_m.

Since $dG = 0$ when $r = r^*$, the critical nucleus is effectively in equilibrium with the surrounding liquid.

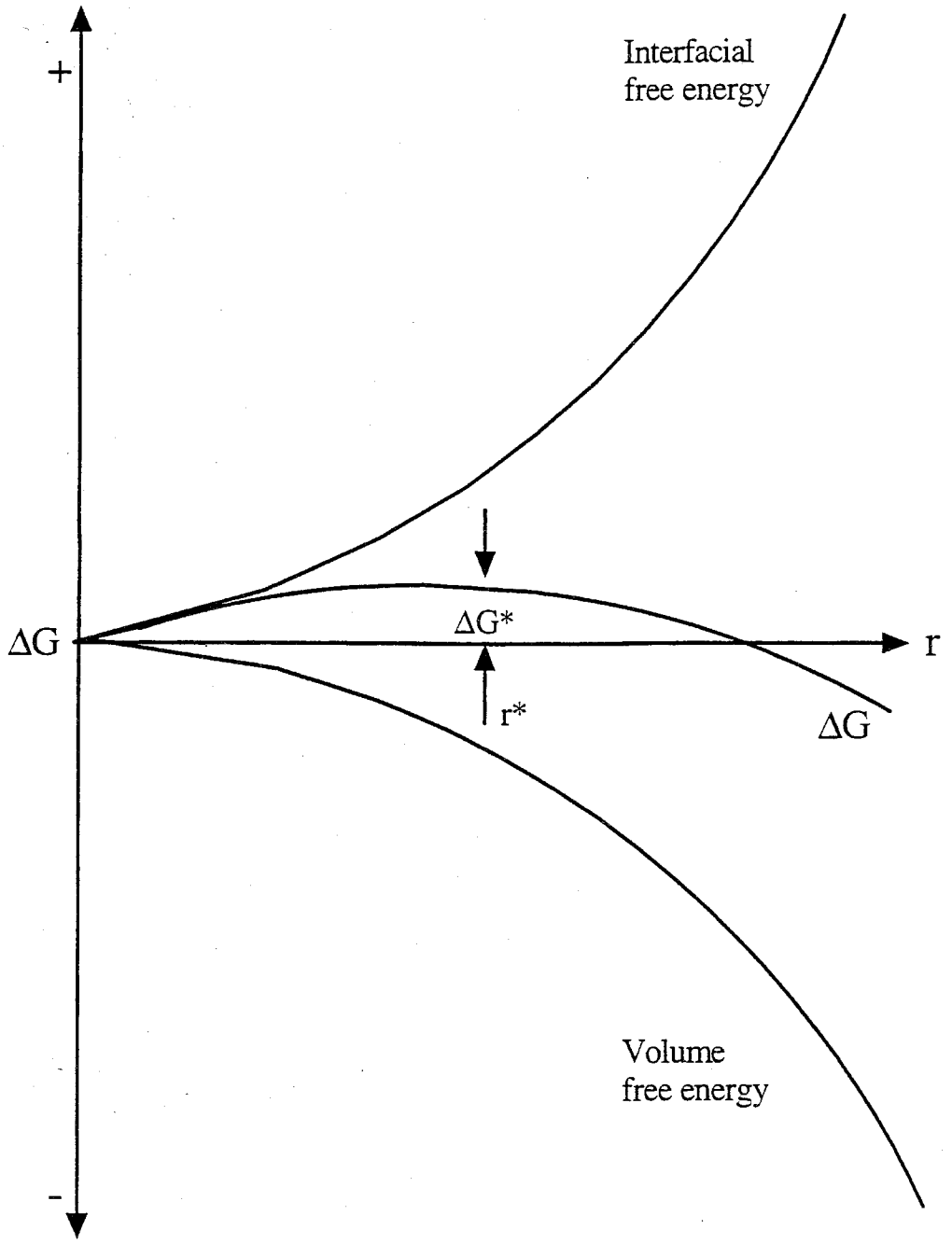

Fig. 1.7. Gibbs free energy ΔG_v associated with the nucleation of a crystalline embryo as a function of its radius.

The competition between these two terms gives a free energy maxima:

$$\Delta G^* = \frac{16\pi}{3}\left(\frac{\sigma^3}{\Delta G_v^2}\right)$$

at a critical nucleus radius

$$r^* = -\frac{2\sigma}{\Delta G_v}.$$

The ΔG^* is the nucleation energy barrier. Thus, the crystalline nuclei larger than critical nucleus radius r^* will grow with decreasing free energy and be stabilized. Crystalline nuclei smaller than r^* will tend to remelt with increasing free energy. The number of embryos that have reached the critical radius r^* can be obtained from the Boltzmann distribution:

$$n^* = n\exp\left(-\frac{\Delta G^*}{kT}\right)$$

where n is total number of atoms in the system, k is the Boltzmann constant, and T is the absolute temperature. Below the melting point T_m, the equation $n^* = n\exp\left(-\frac{\Delta G^*}{kT}\right)$ only applies for $r \leq r^*$ because embryos greater than the critical size are stable nuclei of solid and no longer part of the liquid. Then the nucleation rate I is governed by the rate at which smaller embryos can grow to the critical size. For the small embryos to grow, atoms need to transport from the liquid side of the interface to the crystal side so that the embryos growth rate is determined by the rate of atom transport which is described by the atomic diffusivity D. The diffusivity is related to the viscosity by the Stokes-Einstein relation,

$$D = \frac{kT}{3\pi a_0 \eta}$$

where a_0 is the interatomic distance, k is Boltzmann constant.

Therefore, the homogeneous nucleation rate contains two terms, one results from free energy difference between liquid and crystal, the other from the atomic mobility. It is given by

$$I = \frac{k_n}{\eta(T)} \exp\left(-\frac{\Delta G^*}{kT}\right)$$

where k_n is a kinetic constant, η is the viscosity. As the liquid is cooled below the melting point, the driving force for nucleation is continuously increasing. This is opposed by the rapidly decreasing atomic mobility at very high undercoolings. The overall nucleation rate reflects these two factors by increasing from zero at the transformation temperature T_m to a maximum value somewhere below T_m and then decreasing with further decreases in temperature as shown in Fig. 1.8.[35]

The viscosity of undercooled melts has been found to be well described by the Vogel-Fulcher equation:

$$\eta(T) = A \exp\left(\frac{B}{T - T_0}\right)$$

where A,B and T_0 are constants.

Using the linear approximation, the expression for ΔG becomes

$$\Delta G = -\frac{L\Delta T_r}{V_m}$$

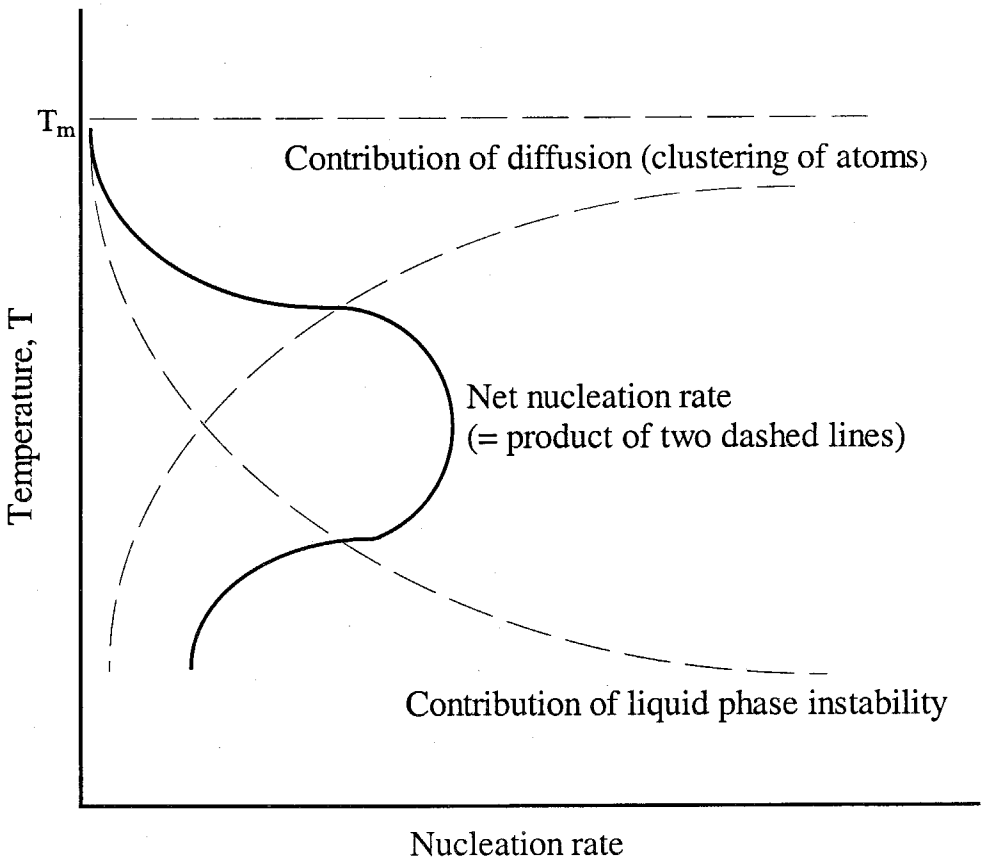

Fig. 1.8. The rate of nucleation is a product of two curves that present two opposing factors (instability and diffusivity). Reproduced from ref. 35.

and the homogeneous nucleation frequency becomes

$$I = \frac{k_n}{\eta(T)} \exp\left(-\frac{16\pi}{3} \frac{\alpha^3 \beta}{\Delta T_r^2 T_r} \right)$$

where L is the molar latent heat of fusion, V_m is molar volume of the crystal, $T_r = T/T_m$, $\Delta T_r = 1\text{-}T_r$ and α and β are dimensionless constants defined by

$$\alpha = \frac{(N_A V_m^2)^{1/3} \sigma}{L} \; ; \qquad \beta = \frac{L}{RT_m}$$

where N is Avogardro's number.

1.3.3 Heterogenous Nucleation

The formation of a nucleus of the critical size can be catalyzed by a solid particle suspended in the liquid, the surface of the container, or a solid film, such as oxide, on the surface of the liquid. This nucleation which is catalyzed by a suitable surface in contact with the liquid is called heterogeneous nucleation.

Consider a solid embryo forming in contact with a perfectly flat substrate as shown in Fig. 1.9. Assuming that the interface is stable and in equilibrium, the balance for the horizontal components of the surface tension requires[36]

$$\sigma_{SL} = \sigma_{SC} + \sigma_{LC} \cos\theta$$

where σ_{SL}, σ_{SC}, and σ_{LC} are the interfacial energies between substrate and liquid, substrate and crystal, and liquid and crystal, respectively. θ is the angle of contact between the crystalline embryo and the substrate, also known as the wetting angle.

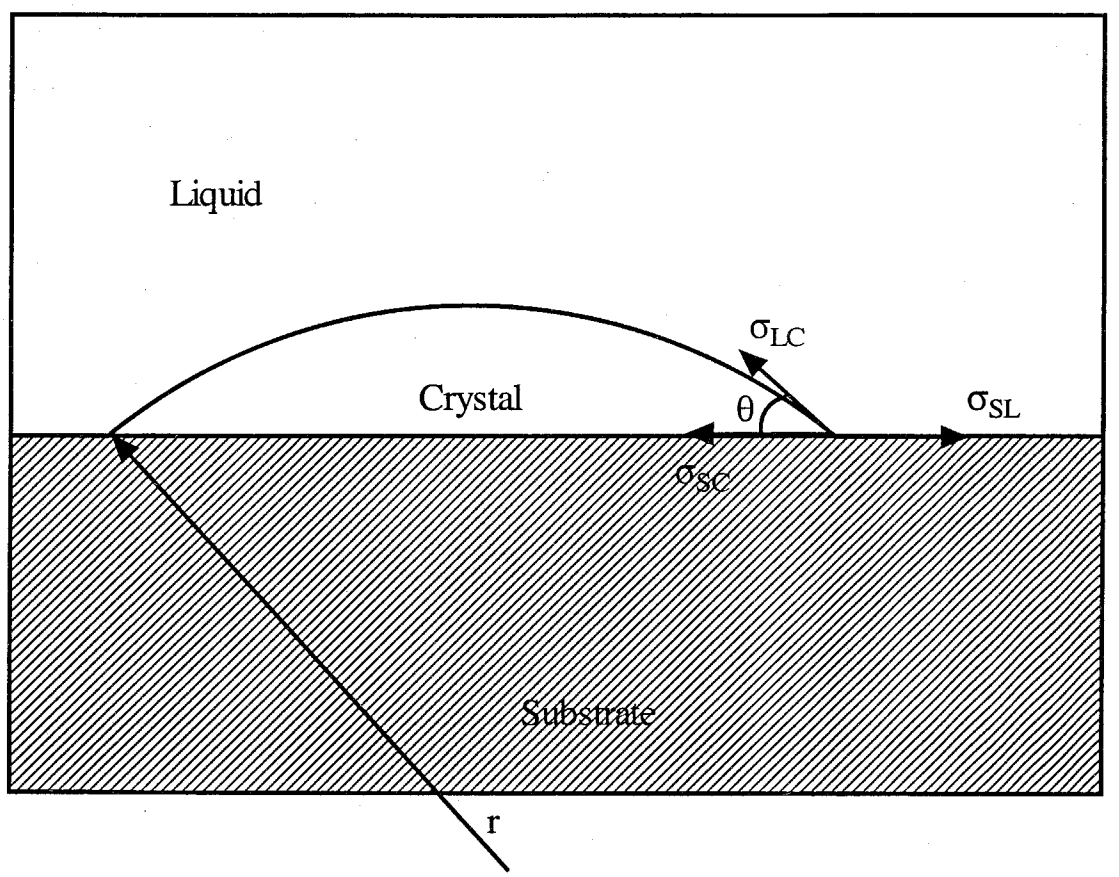

Fig. 1.9. Stability of a spherical cap shaped embryo on a substrate. Reproduced from ref. 36.

It is convenient to represent the surface energy relationship by the parameter m which is defined as

$$m = \frac{\sigma_{SL} - \sigma_{SC}}{\sigma_{LC}}$$

If $m>1$, then there is complete contact. The crystal spreads completely across the surface of the substrate. If $m<-1$, then no contact occurs, and any contact between embryo and substrate causes increase in interfacial energy. A spherical cap forms for any value of m between +1 and –1.

For a spherical cap, the surface area representing the interface between the liquid and the embryo is

$$A = 2\pi(1-\cos\theta)\, r^2$$

And the volume is given by

$$V = \frac{1}{3}\pi(1-\cos\theta)^2(2+\cos\theta)r^3$$

The Gibbs' free energy change associated with the formation of a spherical cap shaped crystalline embryo is given by

$$\Delta G_{hetero} = 2\pi(1-\cos\theta)r^2\sigma_{LC} + \pi(r\sin\theta)^2(\sigma_{SC} - \sigma_{SL})$$

$$+\frac{\pi}{3}(1-\cos\theta)^2(2+\cos\theta)r^3\Delta G_v$$

The first term represents the interfacial energy between the liquid and the crystalline embryo. The second term is the energy of replacing the interface between substrate and liquid by one between substrate and crystal, and the third term is the

energy of converting the volume of liquid to crystal. This can be rewritten using the energy change for homogeneous nucleation ΔG.

$$\Delta G_{hetero} = f(\theta)\Delta G$$

$$= \frac{(1-\cos\theta)^2(2+\cos\theta)}{4}\Delta G$$

Differentiating with respect to r, we find that ΔG_{hetero} has maximum at the same point as ΔG. Thus, the radius of critical spherical cap for heterogeneous nucleation is the same as the radius of critical nucleus for homogeneous nucleation. However, the energy of formation is reduced by the factor $f(\theta)$. Similar to the equation of the homogeneous nucleation rate, the heterogeneous nucleation rate is given by

$$I_{hetero} = \frac{k_n}{\eta(T)}\exp\left(-\frac{f(\theta)\Delta G^*}{kT}\right)$$

Since a $f(\theta)$ is between 0 and 1, it increases heterogeneous nucleation rates that are orders of magnitude larger than homogeneous nucleation rates. A smaller amount of undercooling is necessary to obtain a given rate of heterogeneous nucleation compared to homogeneous nucleation. Fig. 1.10 shows the differences between homogeneous and heterogeneous nucleation.[37]

1.4 Growth

The growth of a stable nucleus ($r > r^*$) will be dertermined by the rate at which atoms can move and attach themselves to the nucleus. Since both these processes require atom movements, the growth rate is diffusion-controlled. Analogous to Fick's first law, there are two important factors that affect the diffusive

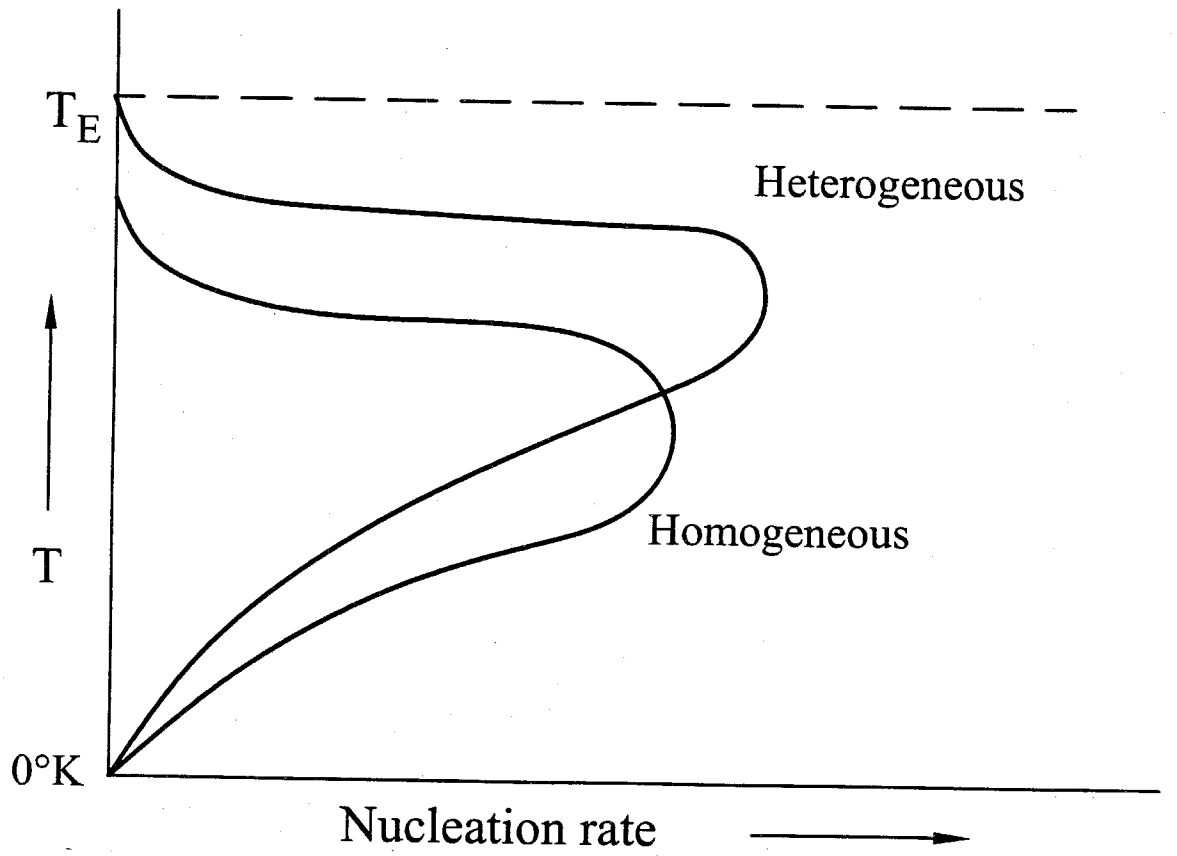

Fig. 1.10. The differences between homogeneous and heterogeneous nucleation. Reproduced from ref. 37.

motion of atoms to the nucleus: (1) the driving force for the transformation (equivalent to the free energy change associated with the transformation that is proportional to ΔT, the amount of undercooling), and (2) the diffusion coefficient of the atoms, proportional to $exp\ (-\Delta E_D/kT)$, where ΔE_D is the activation energy for diffusion. At low temperatures and at temperatures just below the equilibrium temperature the total transformation rate is small because both the nucleation and growth rates are small. In the temperature range in between, the transformation rate increases to a maximum. Since the time required for the trasformation process to proceed to a certain extent (say, 10% of the total volume is transformed) is inversely proportional to the transformation rate, the transformation time will vary as shown in Fig. 1.11.[37] Actually, for any trasnsformation, there will be a family of C curves that mark the start (0%), finish (100%), and intermediate points of the insotermal transformation, conducted at a constant temperature. The minimum time intercept on the "start" curve is called the nose of the curve. The functional form of the time dependent of the transformation is complicated and is beyond the scope of this thesis. Since these curves contain time, temperature, and extent of transformation, they are commonly referred to as T-T-T curves. In practice, the isothermal transformation temperature or the cooling rate will play an important role in determining the size of the particles. When the nucleation rate is low but the growth rate is high, only a relatively few nuclei will form before the trasformation is complete, so that the particles will be large. This would be the case for an alloy quenched from $T < T_E$ to

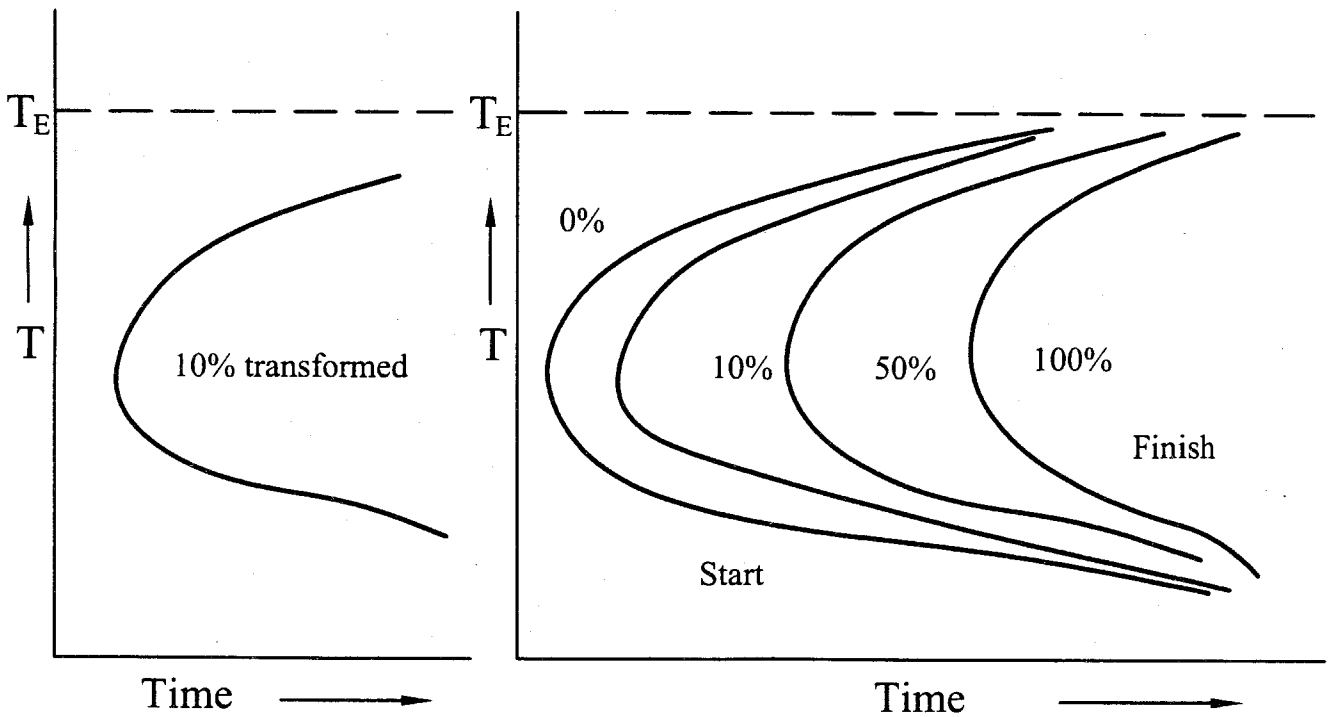

Fig. 1.11. Time-temperature-transformation curves for a hypothetical transformation.

Reproduced from ref. 37.

T_1 (Fig. 1.12)[37] and then isothermally transformed. Alternatively, when the nucleation rate is high and the growth rate is low, many nuclei form before the transformation is complete, so that the average size of the particles will be small. This would be the case for an alloy that was isothermally transformed at $T = T_2$. Similarly, when a material is continuously and slowly cooled from $T > T_E$ (curve S, Fig. 1.12)[37] most of the transformation occurs at high temperatures, where the nucleation rate is low and the particles are then large. When the continuous cooling rate is fast (curve F) most of the transformation occurs at low temperatures, where the nucleation rate is high and the particles are then small.

1.4.1 Heat of Flow and Interface Stability

Once solid nuclei form, growth occurs as atoms are attached to the solid surface. The nature of the growth of the solid depends on how heat is removed from the system. Two types of heat must be removed; the specific heat of the liquid and the latent heat of fusion. The specific heat is the heat required to change the temperature of a unit weight of the material by one degree. The specific heat must be removed first, either by radiation into the surrounding atmosphere or by conduction into the surrounding mold, until the liquid cools to its freezing temperature. The latent heat of fusion must be removed from the solid-liquid interface before solidification is completed. The manner in which we remove the latent heat of fusion determines the growth mechanism and final structure.

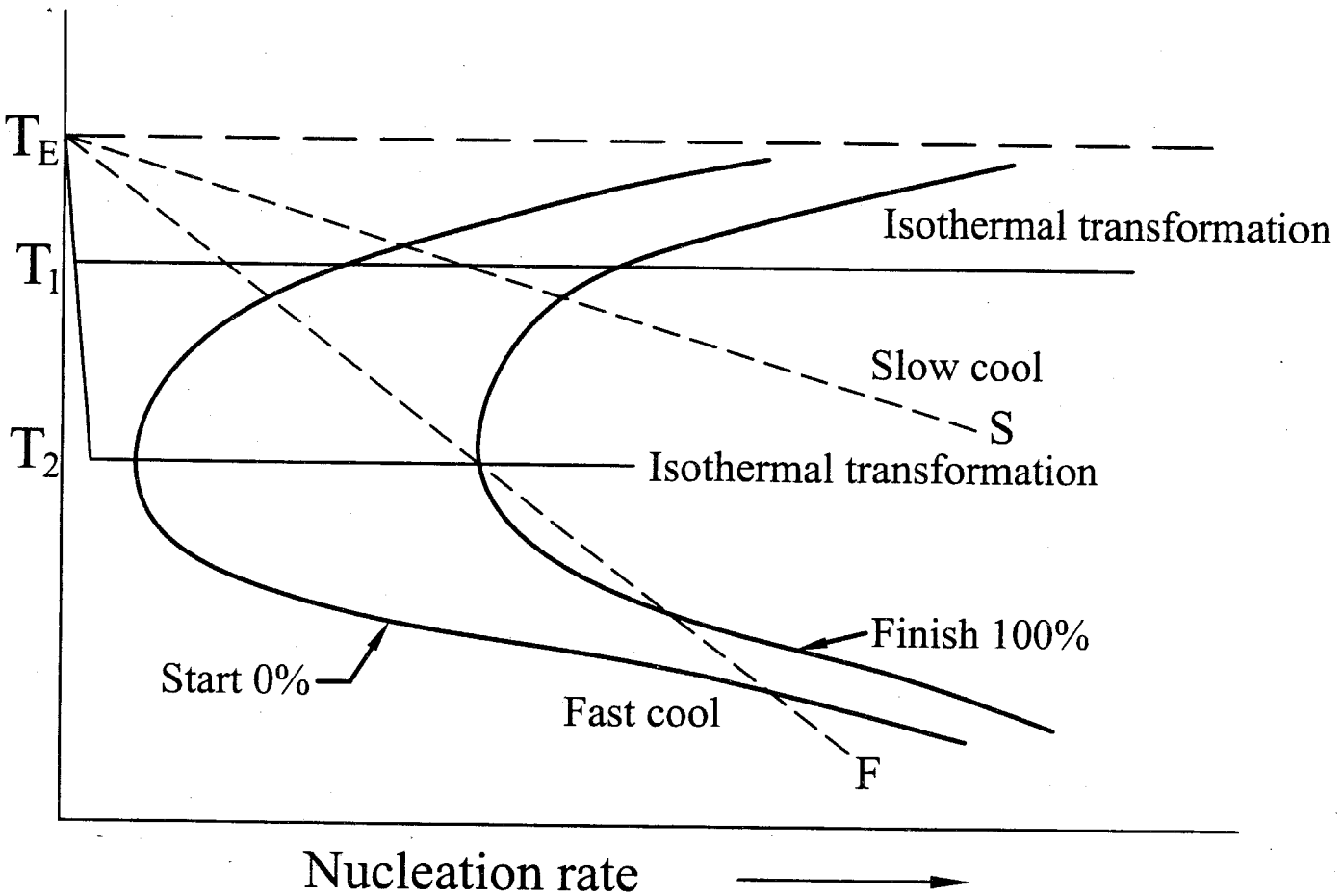

Fig. 1.12. Effects of cooling rate and temperature of transformation on the rates of transformation. Reproduced from ref. 37.

1.4.2 Planar Growth

When a well-inoculated liquid cools under equilibrium conditions, the temperature of the liquid is greater than the freezing temperature and the temperature of the solid is at or below the freezing temperature. During solidification, the latent heat of fusion is removed by conduction from the solid-liquid interface through the solid to the surroundings. Any small protuberance that begins to grow on the interface is surrounded by liquid above the freezing temperature. The growth of the protuberance then stops until the remainder of the interface catches up. This growth mechanism, known as planar growth, occurs by the movement of a smooth solid-liquid interface into the liquid.

Solidification is controlled by the rate at which the latent heat of solidification can be conducted away from the solid/liquid interface. Conduction can take place either through the solid or the liquid depending on the temperature gradients at the interface. Consider solid growing at a velocity υ with a planar interface into a superheated liquid, Fig. 1.13(a).[34] The heat flow away from the interface through the solid must balance that from the liquid plus the latent heat generated at the interface, i.e.,

$$K_S T'_S = K_L T'_L + \upsilon L_V$$

where K is the thermal conductivity, T' is the temperature gradient (dT/dx), the subscripts S and L stand for solid and liquid, υ is the rate of growth of the solid, and L_V is the latent heat of fusion per unit volume. This equation is quite general for a

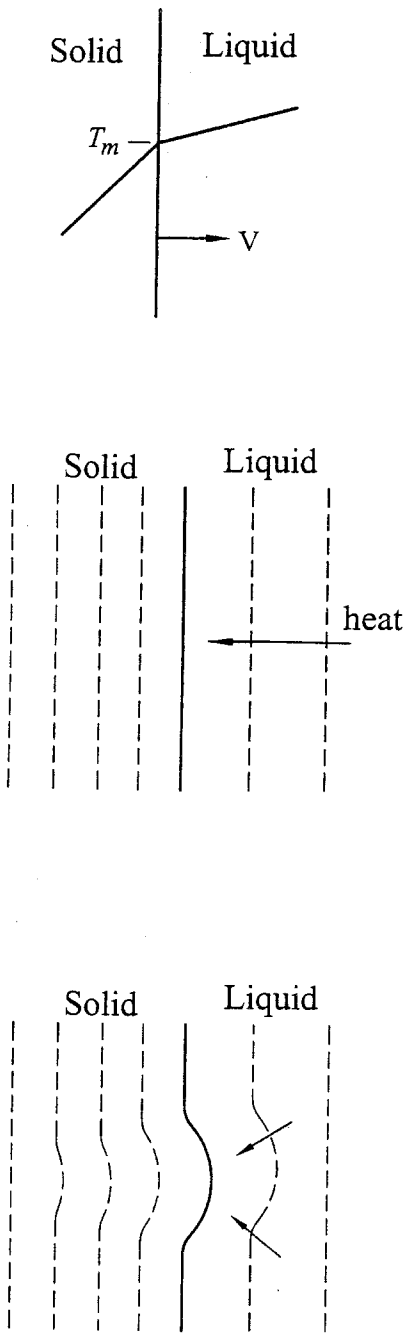

Fig. 1.13. (a) Temperature distribution for solidification when heat is extracted through the solid. Isoterms (b) for a planar S/L interface, and (c) for a protrusion. Reproduced from ref. 34.

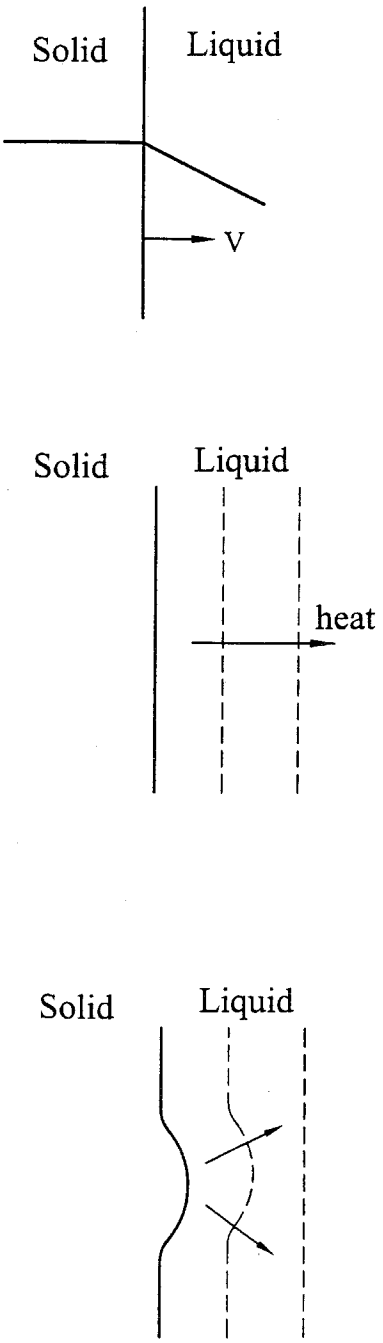

Fig. 1.14. As Fig. 1.13, but for heat conduction into the liquid. Reproduced from ref. 34.

planar interface and even holds when heat is conducted into the liquid ($T'_L < 0$), Fig. 1.14(a).[34] When a solid grows into a superheated liquid, a planar solid/liquid interface is stable. This can be shown as follows. Suppose that as a result of a local increase in v a small protrusion forms at the interface, Fig. 1-13(c). If the radius of curvature of the protrusion is so large that the Gibbs-Thomson effect can be ignored the solid/liquid interface remains isothermal at essentially T_m. Therefore, the temperature gradient in the liquid ahead of the nodule will increase while that in the solid decreases. Consequently more heat will be conducted into the protruding solid and less away so that the growth rate will decrease below that of the planar regions and the protrusion will disappear.

1.5.2 Dendritic Growth

When nucleation is poor, the liquid undercools before the solid forms. Under these conditions, a small solid protuberance called a dendrite which forms at the interface, is encouraged to grow. As the solid dendrite grows, the latent heat of fusion is conducted into the undercooled liquid, raising the temperature of the liquid toward the freezing temperature. Secondary and tertiary dendrite arms can also form on the primary stalks to speed the evolution of the latent heat. Dendritic growth continues until the undercooled liquid warms to the freezing temperature. Any remaining liquid then solidifies by planar growth. The difference between planar and dendritic growth arises because of the different sinks for the latent heat. The container or mold must absorb the heat in planar growth, but the undercooled liquid absorbs the heat in dendritic growth.

In pure metals, dendritic growth normally represents only a small fraction of the total growth:

$$\text{Dendritic fraction:} \quad f = \frac{c\Delta T}{\Delta H_f}$$

where c is the specific heat of the liquid, ΔT is the undercooling, and ΔH_f is the latent heat of fusion.[38] The numerator represents the heat that the undercooled liquid can absorb, and the latent heat in the denominator represents the total heat that must be given up during solidification. As the undercooling ΔT increases, more dendrite growth occurs.

If a protrusion forms on the solid in this case, the negative temperature gradient in the liquid becomes even more negative. Therefore, heat is removed more effectively from the tip of the protrusion than from the surrounding regions allowing it to grow preferentially. A solid/liquid interface advancing into supercooled liquid is thus inherently unstable.

Heat conduction through the solid as depicted in Fig. 1.13, arises when solidification takes place from mould walls which are cooler than the melt. Heat flow into the liquid, however, can only arise if the liquid is supercooled below T_m. Such a situation can arise at the beginning of solidification if nucleation occurs at impurity particles in the bulk of the liquid. Since a certain supercooling is required before nucleation can occur, the first solid particles will grow into supercooled liquid and the latent heat of solidification will be conducted away into the liquid. An originally spherical solid particle will therefore develop arms in many directions. As the primary

arms elongate their surfaces will also become unstable and break up into secondary and even tertiary arms. This shape of solid is known as a dentrite.

Let us now take a closer look at the tip of a growing dendrite. The situation is different from that of a planar interface because heat can be conducted away from the tip in three dimensions. If we assume the solid is isothermal ($T'_S = 0$) the growth rate of the tip υ will be given by a similar equation to $K_S T'_S = K_L T'_L + \upsilon L_V$ provided T'_L is measured in the direction of υ. A solution to the heat-flow equations for a hemispherical tip shows that the (negative) temperature gradient T'_L is approximately given by $\Delta T_C / r$ where ΔT_C is the difference between the interface temperature (T_i) and the temperature of the supercooled liquid far from the dendrite (T_∞) as shown in Fig. 1.15.[34] Equation $K_S T'_S = K_L T'_L + \upsilon L_V$ therefore gives

$$\upsilon = \frac{-K_L T'_L}{L_V} \cong \frac{K_L}{L_V} \cdot \frac{\Delta T}{r}$$

Thus for a given ΔT, rapid growth will be favored by small values of r due to the increasing effectiveness of heat conduction as r diminishes. However ΔT is not independent of r. As a result of the Gibbs-Thompson effect equilibrium across a curved interface occurs at an undercooling ΔT_r below T_m given by

$$\Delta T_r = \frac{2\sigma T_m}{L_V r}$$

The minimum possible radius of curvature of the tip is when ΔT_r equals the total undercooling $\Delta T_0 = T_m - T_\infty$. This is just the critical nucleus radius r^* given by $(2\sigma T_m / L_V \Delta T_0)$. Therefore, in general ΔT_r is given by $\Delta T_0 r^* / r$.

Finally since $\Delta T_0 = \Delta T_C + \Delta T_r$, equation $v = \frac{-K_L T'_L}{L_V} \cong \frac{K_L}{L_V} \cdot \frac{\Delta T}{r}$ becomes

$$v = \frac{K_L}{L_V} \cdot \frac{1}{r}(1 - \frac{r^*}{r})$$

It can thus be seen that the tip velocity tends to zero as $r \rightarrow r^*$ due to the Gibbs-Thompson effect and as $r \rightarrow \infty$ due to slower heat conduction. The maximum velocity is obtained when $r = 2r^*$.

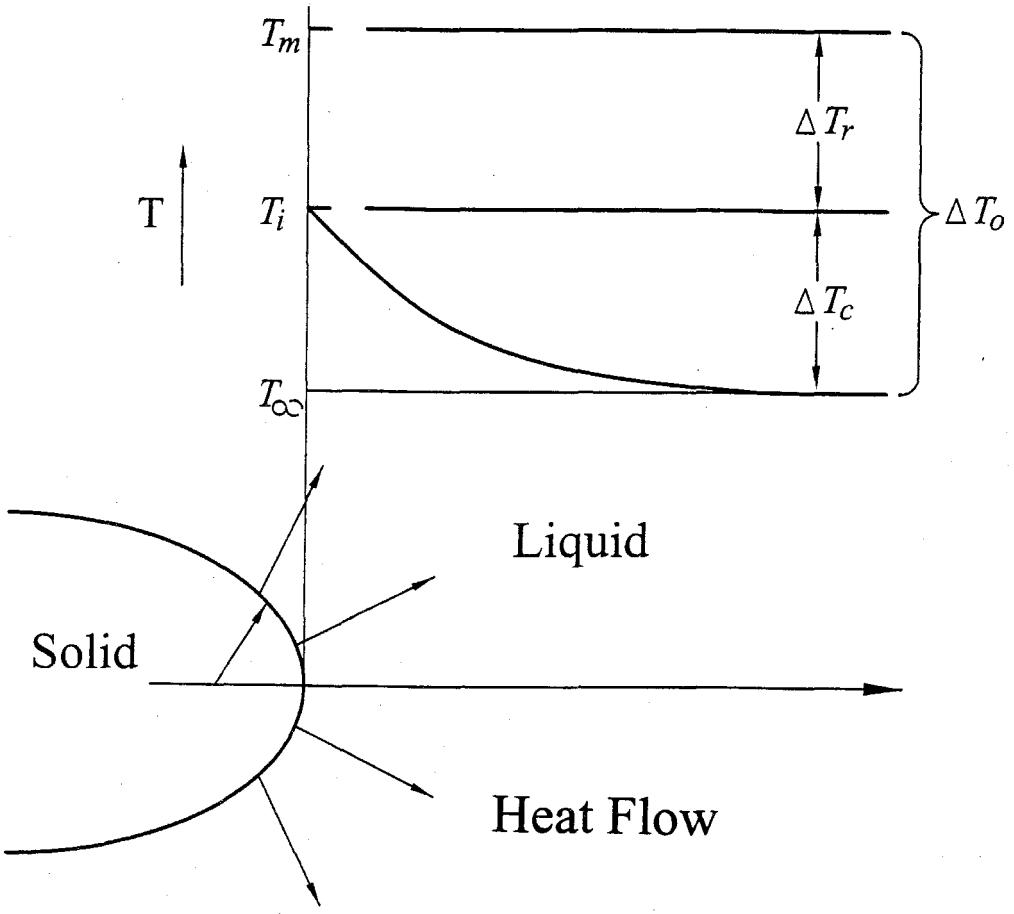

Fig. 1.15. Temperature distribution at the tip of a growing thermal dendrite. Reproduced from ref. 34.

REFERENCES

1. R. Busch, E. Bakke, and W.L. Johnson, Materials Science Forum. **235-238**, 327 (1997).
2. W. Kurz, Fundamentals of Solidification, Transtec, Switzerland (1986).
3. R. Busch, Y.J. Kim, and W.L. Johnson, J. Appl. Phys. **77**, 4039 (1995).
4. T.R. Anantharaman, in Metallic Glasses: Production, Properites, and Applications (edited by T.R. Anantharaman), Transtec, Switzerland (1984).
5. W. Klement IV, R.H. Willens, and P. Duwez, Nature. **187**, 869 (1960).
6. F.E. Luborsky (ed.), Amorphous Metallic Alloys, Butterworth, London (1983).
7. C.H. Smith, in Rapid Solidified Alloys, edited by H.H. Liebermann (Marcel Dekker, New York), 617 (1993).
8. M. Naka, K. Hashimoto, and T. Masumoto, *J. Japan Inst. Metals*. **38**, 835 (1974).
9. S. Kavesh, Metallic Glasses, Chapter 2, edited by J.J. Gillman and H.J. Leamy (ASM International, Metals Park, OH), 36 (1978).
10. H.S. Chen, Acta Metall. **22**, 1505 (1974).
11. A.J. Drehman, A.L. Greer, and D. Turnbull, Appl. Phys. Lett.**41**, 716 (1982).
12. H.W. Kui, A.L. Greer, and D. Turnbull, Appl. Phys. Lett. **45**, 615 (1984).
13. A. Inoue, T. Zhang, and T. Masumoto, Mater. Trans. JIM. **31**, 425 (1991).
14. A. Inoue, T. Nakamura, N. Nishiyama, and T. Masumoto, Mater. Trans. Acta metall. Mater. **41**, 915 (1993).

15. T. Zhang, A. Inoue, and T. Masumoto, Mater. Trans. JIM. **32**, 1005 (1991).

16. A. Peker and W.L. Johnson, Appl. Phys. Lett. **63**, 2342 (1993).

17. Y.J. Kim, R. Busch, W.L. Johnson, A.J. Rulison, and W.K. Rhim, Appl. Phys. Lett. **65**, 2136 (1994).

18. X.H. Lin and W.L. Johnson, J. Appl. Phys. **78**(11), 6514 (1995).

19. X.H. Lin, PhD thesis, California Institute of Technology; X.H. Lin and W.L. Johnson, Mater. Trans. JIM. **38**, 475 (1997).

20. J.R. Strife and K.M. Prewo, J. Mat.Sci. **17**, 359 (1982).

21. R.U. Vaidya and K.N. Subramanian, J. Mat. Sci. L. **9**, 1397 (1990).

22. R.U. Vaidya, C. Norris, and K.N. Subramanian, J. Mat. Sci. **27**, 4957 (1992).

23. S.J. Cytron, *J. Mat. Sci. Lett.* **1**, 211 (1982).

24. H. Kimura, B. Cunningham, and D.G. Ast, Proc. 4th Int. Conf. On Rapidly Quenched Metals (edited by T. Masumoto and K. Suzuki), 1385, Japan Instit. Metals, Sendai (1982).

25. P.G. Zielinski and D.G. Ast, MRS Symposia Proc.: Rapidly Solidified Metastable Materials (edited by B.H. Kear and B.C. Giessen), 189, Elsevier, New York (1984).

26. J.F. Williford and J.P. Pilger, US patent 3, 776, 297 (1973).

27. H. Choi-Yim and W.L. Johnson, Appl. Phys. Lett. **71**, 3808 (1997).

28. R.D. Conner, R.B. Dandliker, and W.L. Johnson, Acta Mater. **46**, 6089 (1998).

29. H. Choi-Yim, R. Busch, U. Koster, and W.L. Johnson, Acta Materialia, **47**(8), 2355 (1999).

30. R.B. Dandliker, R.D. Conner, and W.L. Johnson, J.Mater. Res. **13**, 2896 (1998).

31. H. Choi-Yim, R. Busch, and W.L. Johnson, J. Appl. Phys. **83**, 7993 (1998).

32. J.H. Holloman and D. Turnbull, Prog. In Met. Phys. **4**, 333 (1953).

33. D. Turnbull, Solid State Physic, Vol. **3**, Academic Press, New York, (1956).

34. D.A. Porter and K.E. Eastering, Phase Transformations in Metals and Alloys, Van Nostrand Reinhold Company, New York, (1981).

35. J.F. Shackelford, Introduction to Mat. Sci for Engineers, MacMillan Publishing, New York, (1992).

36. B. Chalmers, Principles of Solidification, Wiley & Sons, New York, (1964).

37. C.R. Barret, W.D. Nix, and A.S. Tetelman, The Principles of Engineering Materials, Prentice-Hall, New Jersey, (1973).

38. P.R. Askeland, The Science and Engineering of Materials, PWS Publishing Company, Boston (1994).

Chapter 2. Composite Development

2.1 Introduction

The discovery of bulk metallic glasses (BMG's) with critical cooling rates as low as 10^1 to 10^3 K/s allows for the preparation of ductile metal reinforced composites. The $Zr_{41.2}Ti_{13.8}Cu_{12.5}Ni_{10}Be_{22.5}$ (Vit1 or Vitreloy1) has a critical cooling rate of about 1 K/s.[1] However, Vit1, as all other metallic glasses, fails by the formation of highly localized shear bands, which leads to catastrophic failure under unconstraint conditions without much macroscopic plasticity.[2-4] This has motivated composite material development to improve the mechanical properties.

Bulk metallic glasses such as Vit1 have been recently used as a matrix material for composites.[5-11] The second phase in the composite is referred to as the reinforcement. The reinforcement is a crystalline phase which is brought into physical contact with the glass forming melt during processing and subsequently quenched as a two-phase glass/reinforcement mixture. The two-phase liquid/reinforcement mixture created at high temperature is not in thermodynamic equilibrium. Chemical reaction of the two phases causes formation of a third phase (typically at the melt/reinforcement interface), and also leads to composition changes in the remaining melt and reinforcement. Often, it is necessary to suppress this chemical reactivity in order to successfully produce the desired composite.

A new class of ductile metal reinforced bulk metallic glass matrix composites via *in situ* processing was developed.[12] The reinforcement is a crystalline phase which

is precipitated from a molten alloy by nucleation and growth. The mixture is subsequently quenched and freezes into a two phase mixture of glass and crystalline reinforcement. The incorporation of a ductile metal phase into a metallic glass matrix yields a constraint that allows for the generation of multiple shear bands in the metallic glass matrix. This stabilizes crack growth in the matrix and extends the amount of strain to failure of the composite. Specifically, by control of chemical composition and processing conditions, a stable two-phase composite (ductile crystalline metal in a bulk metallic glass matrix) is obtained on cooling from the liquid state. This composite material exhibits both improved toughness and a large plastic strain to failure.[13]

2.2 Processing a Bulk Metallic Glass Matrix Composite via *in situ* Method.

To produce a composite having a crystalline reinforcing phase and an amorphous matrix, one may start with an alloy in the bulk glass forming zirconium-titanium-copper-nickel-beryllium system with added niobium, for example. Cu (99.999%), Ni (99.995%), and Ti (99.995%) from Cerac, Inc., Nb (99.8%) from Alfa Aesar, crystal bar Zr with less than 300 atomic ppm oxygen content from Teledyne Wah-Chang Inc., and Be (99.99%) from Electronic Space Products International were used as raw materials for arc melting. Alloy compositions were prepared in the form of 25g rods of roughly cylindrical cross section, diameter φ = 10 mm and length L = 50 mm, by plasma arc melting in a Ti-gettered argon atmosphere on a water-cooled copper plate. The melting procedure has to result in a homogeneous sample. The best

homogeneity of the final melt was reached after a four step melting procedure: First, elemental Nb and Zr was melted together, then the Be was added. Elemental Cu, Ni and Ti were melted together in a second batch. Finally both ingots were melted together and remelted several times until a homogeneous sample was formed. The molten alloy is then undercooled to a temperature range between the liquidus and solidus for a given composition. A bcc phase nucleates and growth in a dendrite structure. This causes chemical partitioning into a solid crystalline ductile metal dendrites and a liquid phase with different compositions. The liquid phase becomes depleted of the metals crystallizing into the crystalline phase and the composition shifts to a bulk metallic glass forming composition. Cooling of the remaining liquid results in formation of an amorphous matrix around the crystalline phase. From our experience with the arc melting setup, the water cooled copper plate provides a non constant cooling rate of approximately 1 ~ 100 K/s in the critical temperature range between T_g and T_l after turning the arc off. The temperature field under the arc has a steep gradient towards the copper plate, and therefore the actual temperatures and cooling rates could not be directly determined experimentally.

2.3 Understanding Metastable Liquid/Solid Equilibrium

Multidimensional phase diagrams are difficult to visualize and have liquidus and solidus "surfaces". When referring to the solidus in this thesis, it refers in part to a line (or surface) defining the boundary between a partially liquid metal and an entirely solid material. This is appropriate when referring to the boundary between the melt and a solid crystalline phase precipitated for forming the phase embedded in the

matrix.

Before considering alloy selection, we discuss the partitioning method in a pseudo-binary alloy system. Fig. 2.1 is a pseudo-binary phase diagram for alloys of M, refractory bcc metals (e.g., Tungsten or Niobium), and X, where X is a good glass forming composition (e.g., Vit1), i.e., a composition that forms an amorphous metal at reasonable low cooling rates. Compositions range from 100% M at the left margin to 100% of the alloy X at the right margin. An upper slightly curved line is a liquidus for M in the alloy and a steeply curving line near the left margin is a solidus for M with some solid solution of components of X in a body centered cubic M alloy. A horizontal or near horizontal line below the liquidus is, in effect, a solidus for an amorphous alloy. A vertical line in mid-diagram is an arbitrary alloy where there is an excess of M above a composition that is a good bulk glass forming alloy.

As one cools the alloy from the liquid, the temperature crosses the liquidus. Below the liquidus, the bcc M phase becomes thermodynamically stable and has therefore a probability of nucleation. A precipitation of bcc M (with some of the Vit1 components, principally titanium and/or zirconium, in solid solution) commences with a composition where a horizontal line from the liquidus encounters the solidus. With further cooling, there is dendritic growth of M crystals, depleting the liquid composition of M, so that the residual melt composition follows along the sloping liquidus line. Thus, there is a partitioning of the composition to a solid crystalline bcc, M-rich β phase and a liquid composition depleted in M. At an arbitrary processing temperature T_1 the proportion of solid M alloy scales with the distance "A" and the

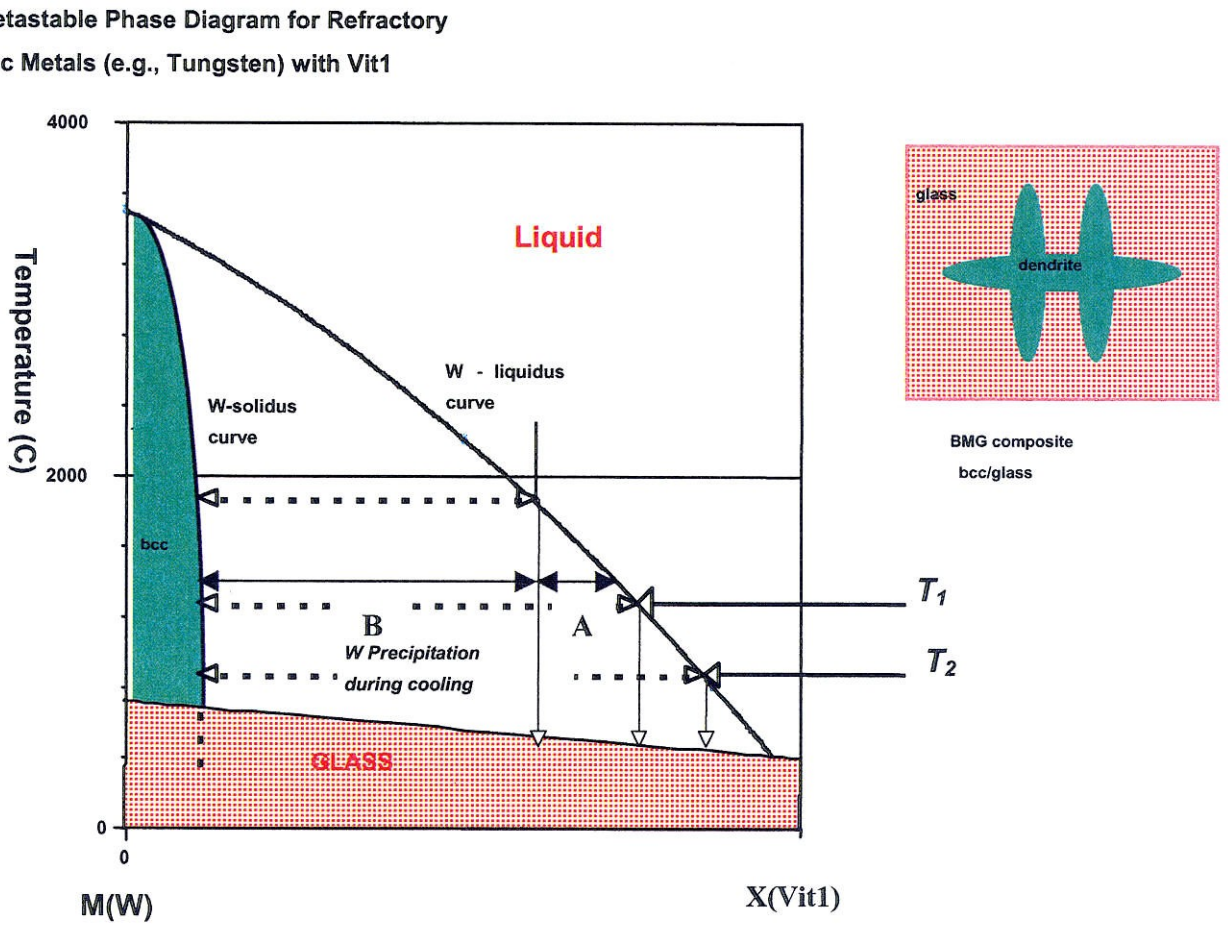

Fig. 2.1. Pseudo binary phase diagram for alloys of M and X, where X is a good glass forming composition (e.g., Vit1), and M is a body centered cubic alloy.

proportion of liquid remaining with the distance "B" in Fig. 2.1. In other words, about 1/4 of the composition is solid dendrites and the other 3/4 is liquid. At equilibrium at a second processing temperature T_2 somewhat lower than T_1, there is about 1/3 solid crystalline phase and 2/3 liquid phase.

If one cools the exemplary alloy to the first or higher processing temperature T_1 and holds at that temperature until equilibrium is reached, and then rapidly quenches the alloy, a composite is achieved having about 1/4 particles of bcc alloy distributed in a bulk metallic glass matrix having a composition corresponding to the liquidus at T_1. One can vary the proportion of crystalline and amorphous phases by holding the alloy at a selected temperature above the solidus to obtain a higher proportion of ductile metallic particles. This of course can be only done to a certain extend since the composition of the matrix might be shifted out of the good glass forming ranges.

The morphology, proportion, size and spacing of ductile metal dendrites in the amorphous metal matrix are also influenced by the cooling rate. Generally speaking, a faster cooling rate results in deeper undercooling prior to nucleation and causes higher nucleation rate. Therefore, the dendrites are smaller and more widely spaced than for slower cooling rates. The orientation of the dendrites is influenced by the local temperature gradient present during solidification.

2.4 Processing Ductile Phase Reinforced Bulk Metallic Glass Composite by Chemical Partitioning in Zr-Ti-M-Cu-Ni-Be System

In order to synthesis a composite with good mechanical properties consisting

of a crystalline reinforcing phase embedded in an amorphous matrix, one may start with compositions based on a bulk metallic glass forming compositions in the Zr-Ti-M-Cu-Ni-Be system, where M is niobium. Alloy selection can be exemplified by reference to Fig. 2.2, which is a section of a pseudo-ternary phase diagram with apexes of titanium, zirconium and X, where X is $Be_9Cu_5Ni_4$. A small circle is indicated near 42% Zr, 13% Ti and 45% X, which is a desirable bulk glass forming alloy composition, Vit1.

There are at least two strategies for designing a useful composite of crystalline metal particles distributed in an amorphous matrix in this alloy system. *Strategy 1 is* based on systematic manipulations of the chemical composition of bulk metallic glass forming compositions in the Zr-Ti-M-Cu-Ni-Be system. *Strategy 2* is based on the preparation of chemical compositions which comprise the mixture of additional pure metal or metal alloys with a good bulk metallic glass forming composition in the Zr-Ti-Cu-Ni-Be system.

2.4.1 *Strategy 1*: Systematic Manipulation of Bulk Metallic Glass Forming Compositions

An excellent bulk metallic glass forming composition has been developed with the following chemical composition: $(Zr_{75}Ti_{25})_{55}X_{45} = Zr_{41.2}Ti_{13.8}Cu_{12.5}Ni_{10}Be_{22.5}$ expressed in atomic percent, and herein labeled as alloy Vit1.[1] This alloy composition has a proportion of Zr to Ti of 75:25. It is represented on the ternary diagram at the small circle in the large oval.

The Vit1 alloy and other neighboring compositions in the phase diagram have

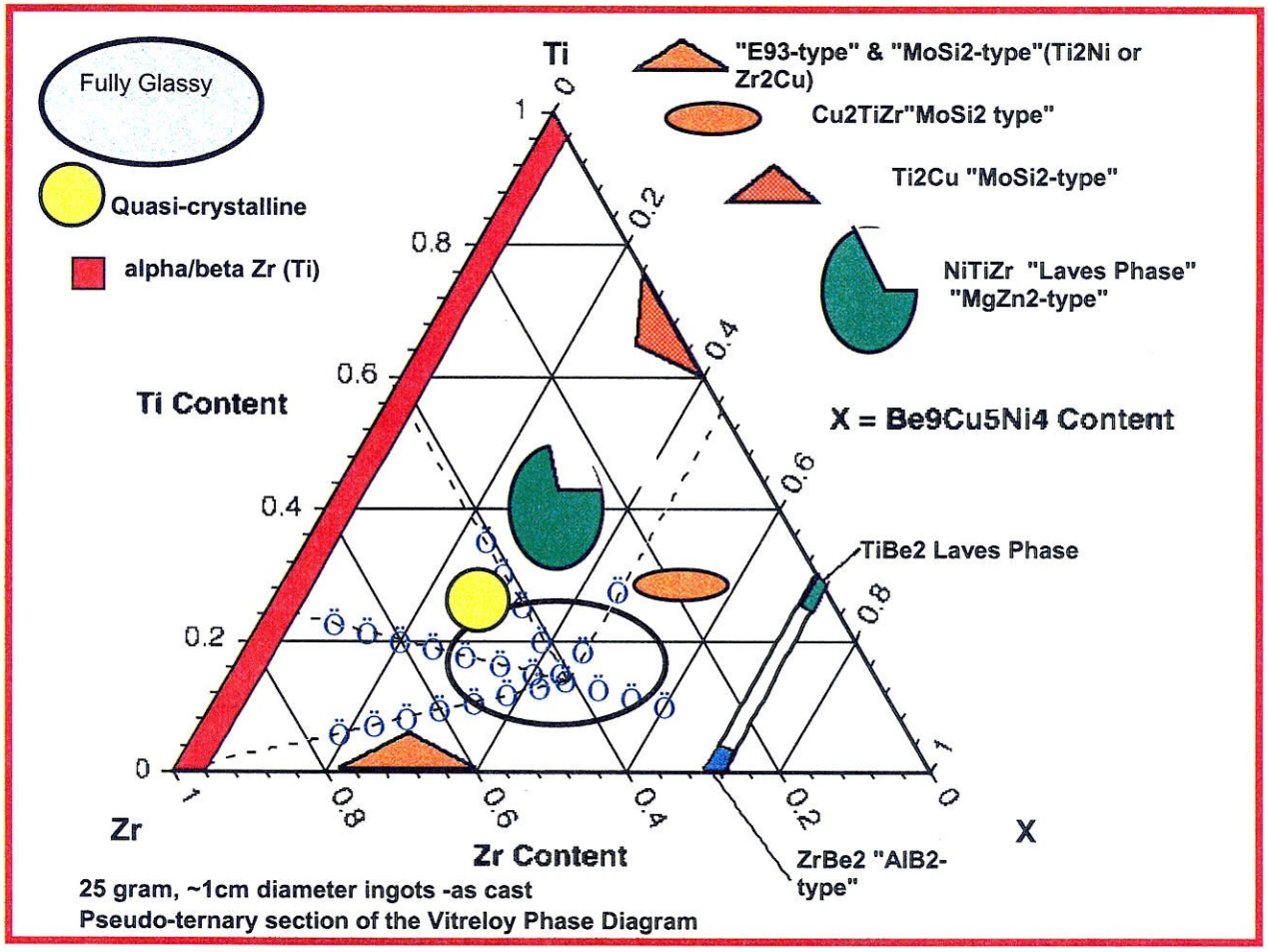

Fig. 2.2. Pseudo ternary phase diagram with apexes of titanium, zirconium, and X, where X is $Be_9Cu_5Ni_4$.

a glass forming ability (GFA) such that they are easily prepared in the amorphous state by arc melting 25g rods of roughly cylindrical cross section, diameter ϕ = 10 mm, and length L = 50 mm. The alloy prepared in this manner is fully amorphous except for a thin crystalline "skull" (less than 1 mm thick) present on the bottom of the as-cast rod. Upon removing the skull layer, the fully amorphous condition is consistently confirmed by the absence of any detectable Bragg peaks in high resolution X-ray scans on cross sectioned specimens as well as by SEM. This bulk glass forming region (GFR) is defined by the oval labeled as GFR in Fig. 2.2. When cooled from the liquid state, chemical compositions that lie within this region are fully amorphous when cooled below the glass transition temperature. Fig. 2.3 shows DSC scans of selected alloys in the GFR region.

The pseudo-ternary diagram also shows a number of competing crystalline or quasi-crystalline phases which limit the bulk metallic glass forming ability. Within the GFR, these competing crystalline phases are destabilized, and hence do not prevent the vitrification of the liquid on cooling from the molten state. However, for compositions outside the GFR, on cooling from the high temperature liquid state, the molten liquid chemically partitions. There are compositions outside GFR where alloying is inappropriate and the partitioned composite may have a mixture of brittle crystalline phases embedded in an amorphous matrix. The presence of these brittle crystalline phases seriously degrades the mechanical properties of the composite material formed. For example, toward the upper right of the larger GFR oval, there is a smaller oval partially overlapping the edge of the larger oval, and in this region a

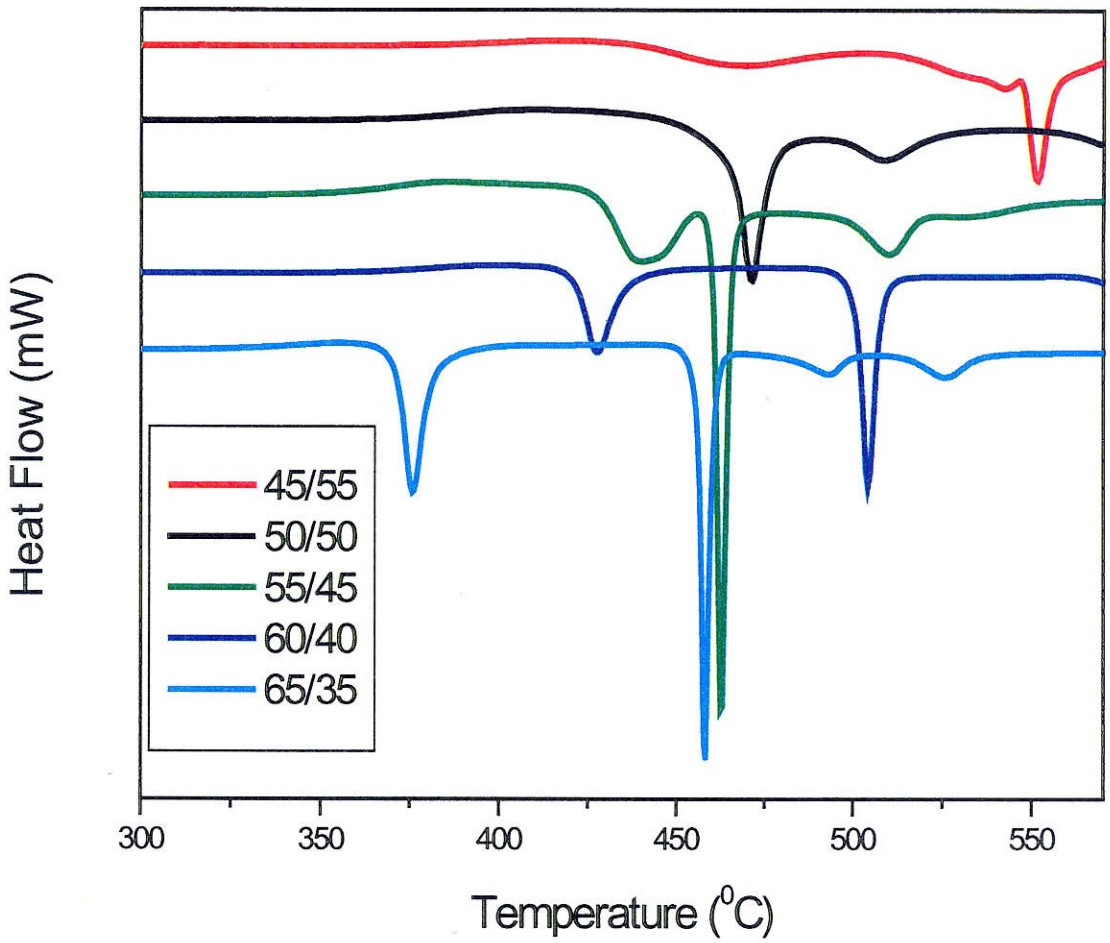

Fig. 2.3. DSC scans of selected alloys in the Glass Forming Region (GFR) shown in Fig. 2.2. All DSC scans are performed at a heating rate of 20K/min. Each scan represent the ratio of 100-x / x on $(Zr_3Ti_1)_{100-x}(Cu_5Ni_4Be_9)_x$ alloy series. The 55/45 is the Vit1 alloy.

brittle Cu_2ZrTi phase may form on cooling the liquid alloy. This is an embrittling phenomenon and such alloys are not suitable for a composite material. The regions indicated on this pseudo-ternary diagram are approximate and schematic for illustrating development of composite materials. Above the left part of large GFR oval, as illustrated in Fig. 2.2, there is a smaller circle representing a region where a quasi-crystalline phase forms leading to embrittlement of the alloy. An upper partial oval represents another region where a NiTiZr Laves phase forms. A small triangular region along the Zr-X margin represents formation of intermetallic $TiZrCu_2$ and/or Ti_2Cu phases. Small regions near 70% X are compositions where a $ZrBe_2$ intermetallic or a $TiBe_2$ Laves phase forms. Along the Zr-Ti margin a mixture of α and β Zr or Zr-Ti alloy may be present.

Consider the composition $(Zr_{75}Ti_{25})_{75}$ X_{25} ($X = Be_9Cu_5Ni_4$) which lies just outside of the oval region where bulk glass is formed in 10 mm cast rods. At this composition, precipitation of α-Zr-Ti (hcp) and β-Zr-Ti (bcc) phases were observed in a vitrified matrix following casting. X-ray diffraction patterns were obtained with an INEL diffractometer using Co K_α radiation (λ = 0.179 nm), a CPS-120 position sensitive detector and Si as an internal standard. Fig. 2.4 shows the x-ray diffraction patterns of $(Zr_{75}Ti_{25})_{75}$ X_{25} alloy containing α-Zr-Ti (hcp) and β-Zr-Ti (bcc) phases and two of fully amorphous alloys in the GFR region.

To form a composite with good mechanical properties, the brittle second phases identified in the pseudo-ternary diagram are to be avoided. This leaves a

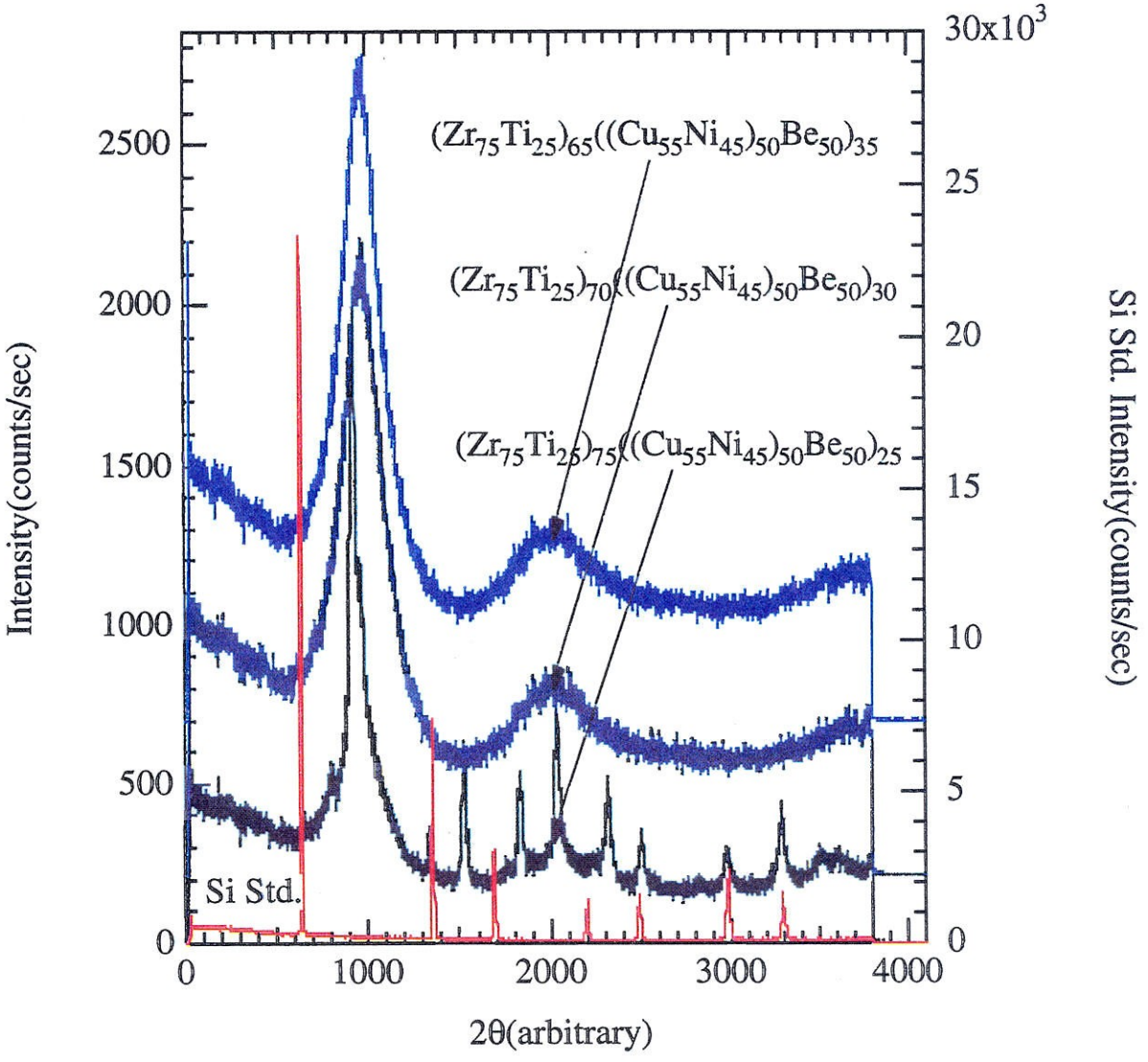

Fig. 2.4. X-ray diffraction patterns of $(Zr_{75}Ti_{25})_{75}X_{25}$ alloy before the β phase is stabilized and two of fully amorphous alloys in the GFR region.

generally triangular region toward the upper left from the $Zr_{42}Ti_{14}X_{44}$ circle where another metal M may be substituted for some of the zirconium and/or titanium to provide a composite with desirable properties. This is reviewed for a substitution of niobium for some of the titanium to avoid brittle crystalline phases and stabilize the ductile β phase.

It is important that the secondary crystalline phase, preferentially nucleated on cooling from the high temperature liquid, be a ductile phase. An example of an *in situ* prepared bulk metallic glass matrix composite which has exhibited outstanding mechanical properties has the nominal composition $(Zr_{100-X}Ti_{X-Z}M_Z)_{100-Y}$ $(Be_9Cu_5Ni_4)_Y$; i.e., an alloy with M = Nb, Z= 6.66, X = 25 and Y = 25. This is along the dashed line of alloys in Fig. 2.2. It has been shown that β phase is formed when Z = 3, extending up to Z = 20 with Y values surrounding 25. Excellent mechanical properties have been found for compositions in the range of Z = *5* to Z = 10, with a premier composition where Z = about 6.66 along this 75:25 line when M is niobium.

Peaks on an X-ray diffraction pattern for the composition, $(Zr_{75}Ti_{18.34}$ $Nb_{6.66})_{75}X_{25}$, show that the secondary phase present has a body-centered-cubic (bcc) or β phase crystalline symmetry, and that the x-ray pattern peaks are due to the β phase only. A Nelson-Riley extrapolation yields a β phase lattice parameter a = 3.496 Å.[14] Addition of small amounts of Nb (replacing Ti) in these alloys results in destabilization of the brittle α-phase and stabilization of the β-phase as shown in Fig. 2.5.

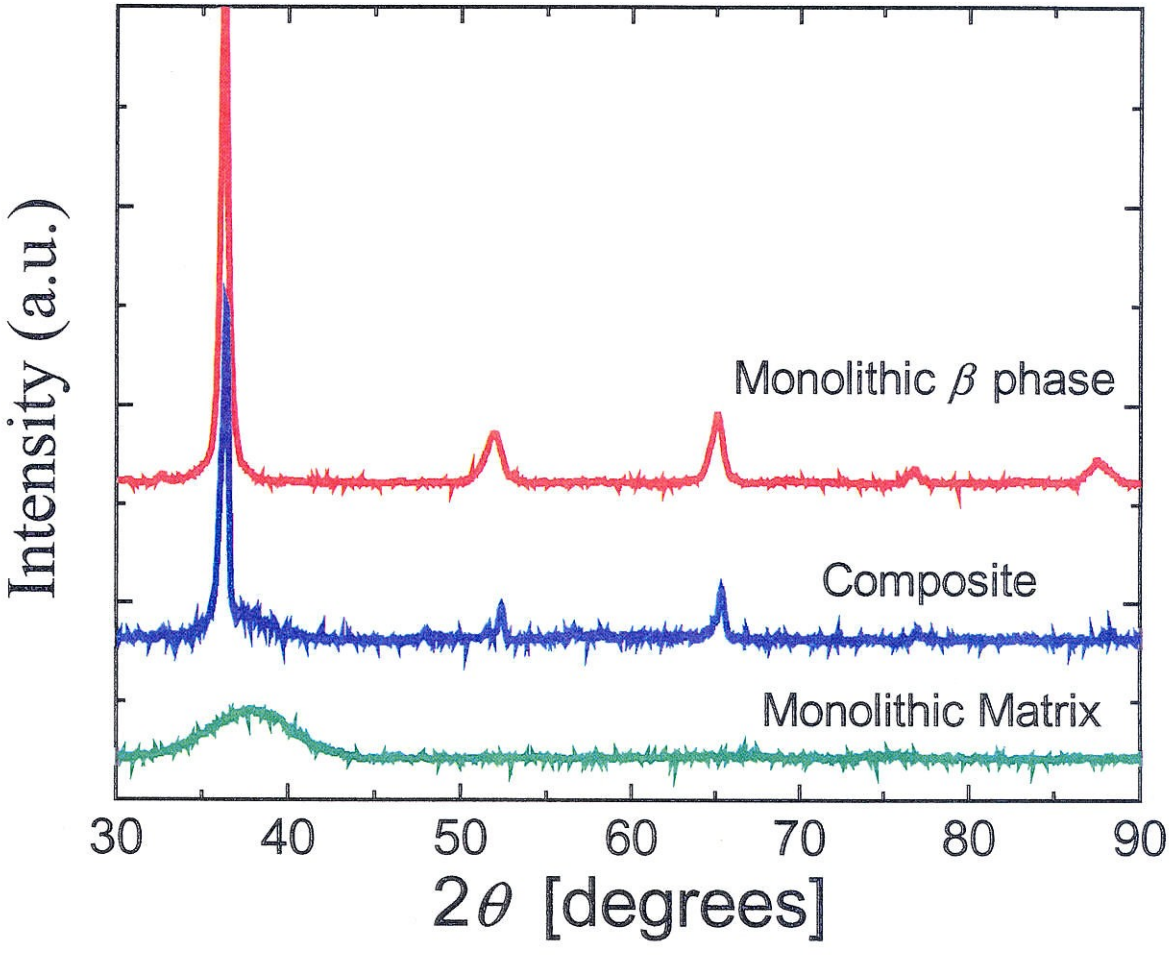

Fig. 2.5. X-ray diffraction patterns of $(Zr_{75}Ti_{18.34}Nb_{6.66})_{75}X_{25}$ composite material together with the monolithic matrix and the β phase. Addition of 5% Nb (replacing Ti) in $(Zr_{75}Ti_{25})_{75}X_{25}$ (X = $Be_9Cu_5Ni_4$) alloy results in stabilization of the bcc-phase (β-phase).

Thus, upon cooling from the high temperature melt, the alloy undergoes partial crystallization by nucleation and subsequent dendritic growth of the ductile crystalline metal phase in the remaining liquid. The remaining liquid subsequently freezes to the glassy state producing a two-phase microstructure containing β phase dendrites in an amorphous matrix.

Also, it should be noted that one should not extend along the 75:25 dashed line to less than about 5% beryllium, i.e., where Y is less than 10 in $(Zr_{100-X}Ti_{X-Z}Nb_Z)_{100-Y}(Be_9Cu_5Ni_4)_Y$. Below that there is only little amorphous phase left, and the alloy consists of mostly dendrites without the desirable properties of the composite. The SEM backscattering image shown in Fig. 2.6 depicts the microstructure of composite materials showing differences in dendrite size and its volume fraction changing Y values of $(Zr_{100-X}Ti_{X-Z}Nb_Z)_{100-Y}(Be_9Cu_5Ni_4)_Y$.

The microstructure of chemically etched $(Zr_{75}Ti_{18.34}\ Nb_{6.66})_{75}X_{25}$ specimen prepared by plasma arc melting shows fully developed dendritic structure of the β phase as shown on Fig. 2.7. This specimen was prepared at a cooling rate estimated at less than 50 K/s. The dendritic structures are characterized by primary dendrite axes with lengths of 50 to 150 μm and radius of about 1.5 ~ 2 μm. Regular patterns of secondary dendrite arms with spacing λ = 6-7 μm are observed having radii somewhat smaller than the primary axis. The dendrite "trees" have a very uniform and regular structure. The primary axes show some evidence of texturing over the sample as expected since dendritic growth tends to occur in the direction of the steepest

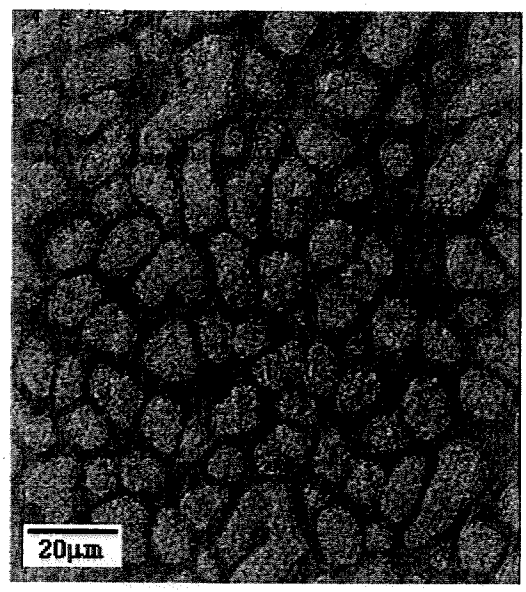

(a)

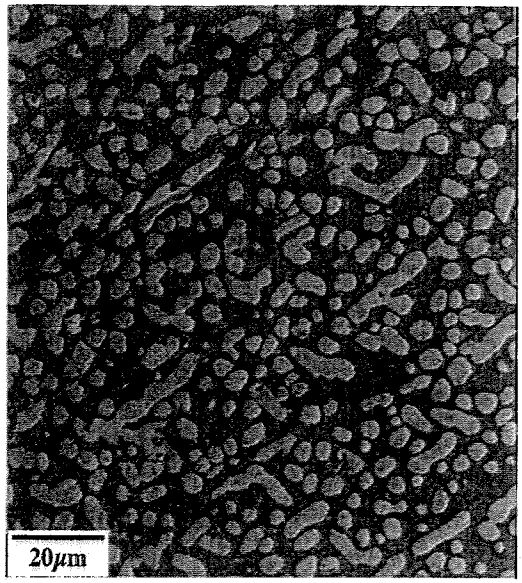

(b)

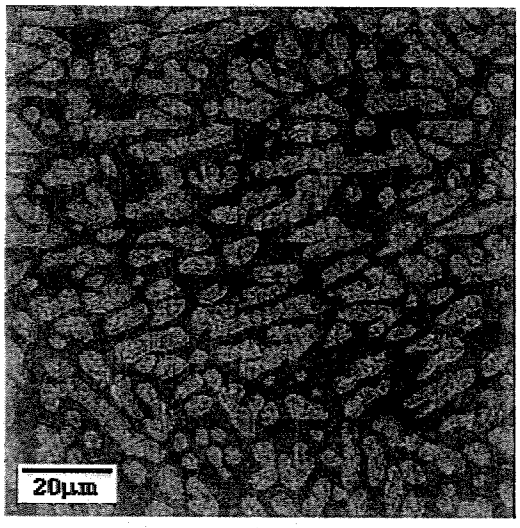

(c)

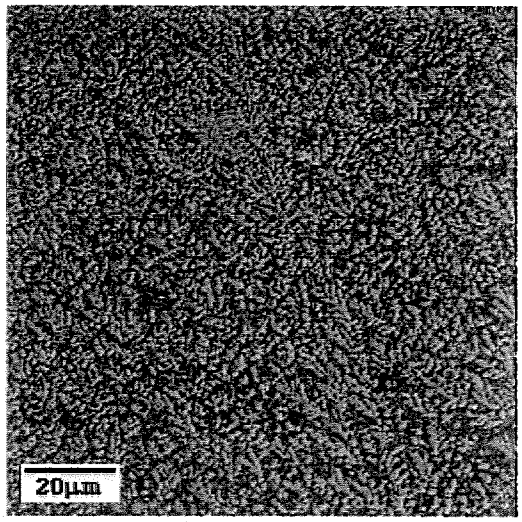

(d)

Fig. 2.6. SEM backscattering images of different microstructures obtained by changing the Y values of $(Zr_{100-X}Ti_{X-Z}Nb_Z)_{100-Y}(Be_9Cu_5Ni_4)_Y$. The Y value for (a) is 27.5, (b) is 25, (c) is 22.5, and (d) is 20. The Nb content is 5% on all of the alloys. The surface is chemically etched with the solution of 40% HF, 20% HNO_3, and 40% HCl in order to enhance the contrast.

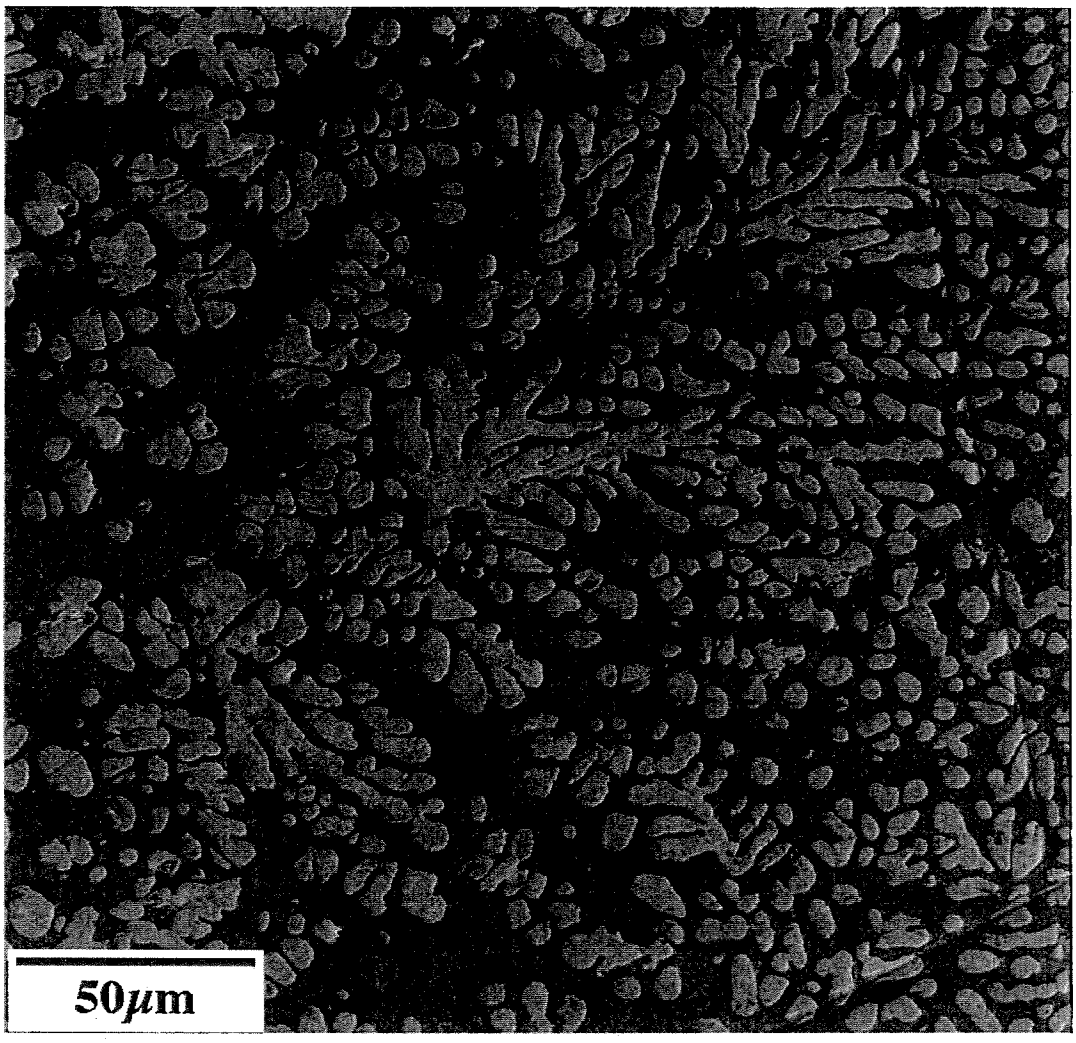

Fig. 2.7. Microstructure of chemically etched $(Zr_{75}Ti_{18.34}\ Nb_{6.66})_{75}X_{25}$ composite material showing fully developed dendritic structure of the β phase. The estimated cooling rate is about 50K/s. This material was made by plasma arc melting on the water-cooled copper mold under the argon environment.

temperature gradient during solidification. Also, the same composite material was cast at Howmet Corporation with a vacuum die casting technology. The size of casting plate is about 410 mm by 540 mm by 3.3 mm.

Since the cooling rate of Howmet specimen is significantly greater than the plasma arc melted specimen, probably at least 100 K/s, the dendrites are appreciably smaller, about five micrometers along the principal direction and with secondary arms spaced about one to two micrometers apart. The dendrites have more of a snowflake-like appearance than the more usual tree-like appearance. Dendrites seem less uniformly distributed and occupy less of the total volume of the composite (about 20%) than in the more slowly cooled composite, as shown in Fig. 2.8. (Cooling was from both faces of a body 3.3 mm thick.)

Electron microprobe analysis gives the average composition for the β phase dendrites (light phase in Fig. 2.7) to be $Zr_{71}Ti_{16.3}Nb_{10}Cu_{1.8}Ni_{0.9}$. Under the assumption that all of the beryllium in the alloy is partitioned into the matrix, the average composition of the amorphous matrix (dark phase) is $Zr_{47}Ti_{12.9}Nb_{2.8}Cu_{11}Ni_{9.6}Be_{16.7}$. Microprobe analysis also shows that within experimental error (about ± 1 at.%), the compositions within the two phases do not vary. This implies complete solute redistribution and the establishment of chemical equilibrium within and between the phases.

Fig. 2.9 shows the total integrated heat of crystallization of the amorphous matrix of composite is ΔH_x = 54 W/g. Analysis of the heat of crystallization of the remaining amorphous matrix compared with that of the fully amorphous sample

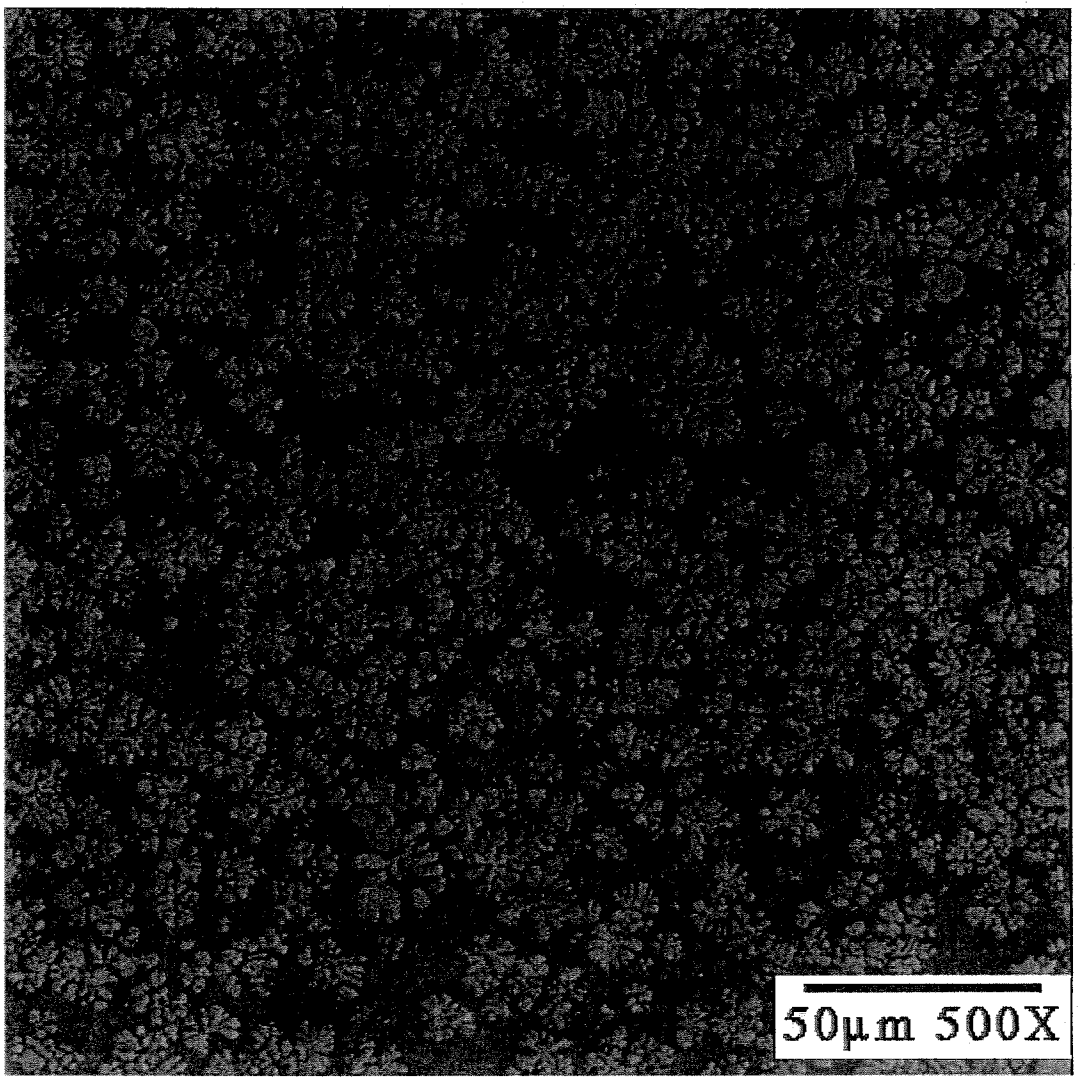

Fig. 2.8. The microstructure of chemically etched $(Zr_{75}Ti_{18.34}\ Nb_{6.66})_{75}X_{25}$ specimen supplied from Howmet Corporation showing snowflake-like dendritic structure of the β phase since the cooling rate was higher than the sample shown in Fig. 2.7.

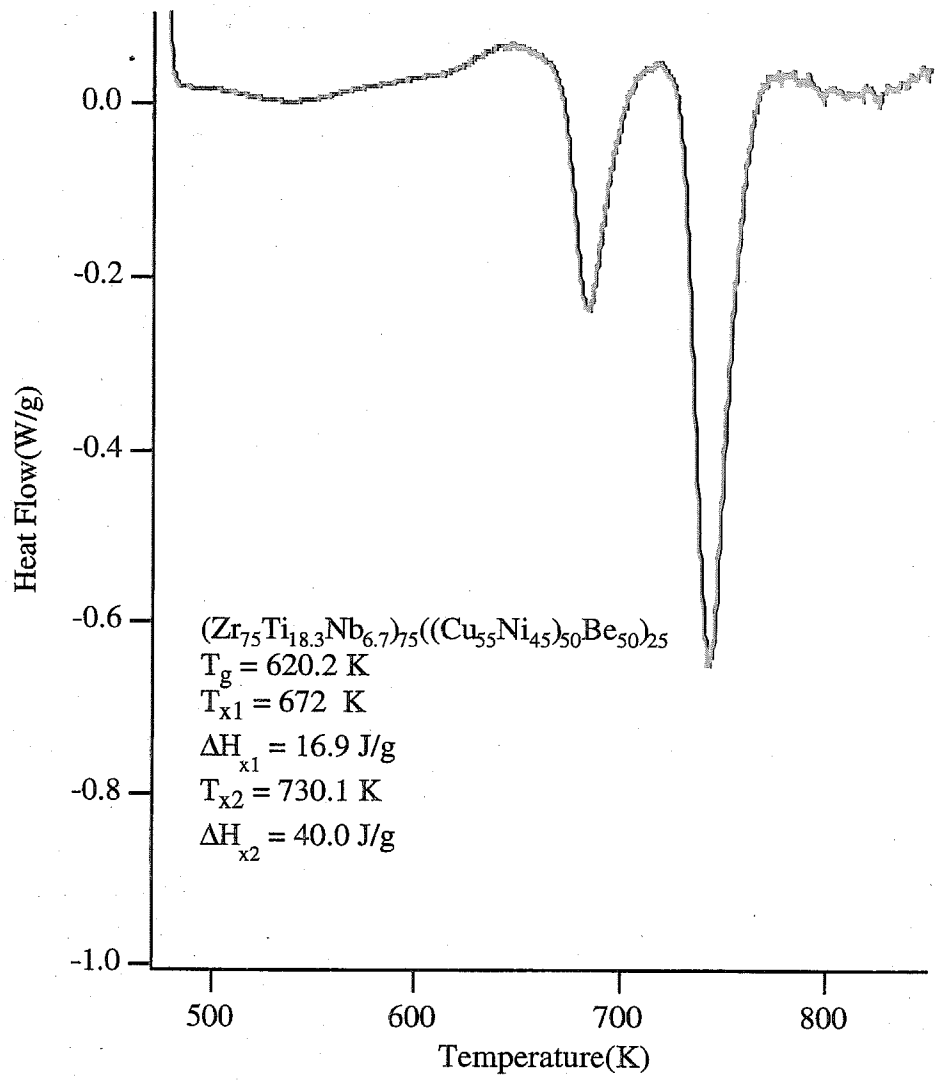

Fig. 2.9. DSC scan on the $Zr_{56.3}Ti_{13.8}Cu_{6.9}Ni_{5.6}Nb_{5.0}$ $Be_{12.5}$ composite material. DSC scans are performed at a heating rate of 20K/min.

(Vit1 $\Delta H_x \approx 73$ W/g) gives a direct estimate of the volume fractions of the two phases. This gives an estimated fraction of about 25% β phase by volume and about 75% amorphous phase. Direct measurement based on area analysis of the SEM image agrees well with this estimate.

Another factor in the improved behavior is the quality of the interface between the ductile metal β phase and the bulk metallic glass matrix. The structure of the reinforcing phase and the interface were analyzed with a Philips EM430 transmission electron microscope (TEM). The interface between particle and matrix is chemically homogeneous, atomically sharp and free of any third phases. It is an intimate amorphous/crystal interface. Fig. 2.10 shows TEM images of composite material. In other words, the materials on each side of the boundary are in chemical equilibrium due to formation of dendrites by chemical partitioning from a melt. This clean interface allows for an iso-strain boundary condition at the particle-matrix interface; this allows for stable deformation and for the propagation of shear bands through the β phase particles. In contrast, the interfaces of previous composite material made by embedding ductile refractory metal wires or particles in a matrix of glass forming alloy are chemically dissimilar and shear band propagation across the boundaries is inhibited. [9-11]

2.4.2 *Strategy 2*: The Preparation of In Situ Composites by the Mixture of Pure Metal or Metal Alloys With Bulk Metallic Glass Forming Compositions

As an additional example of the design of *in situ* composites by chemical

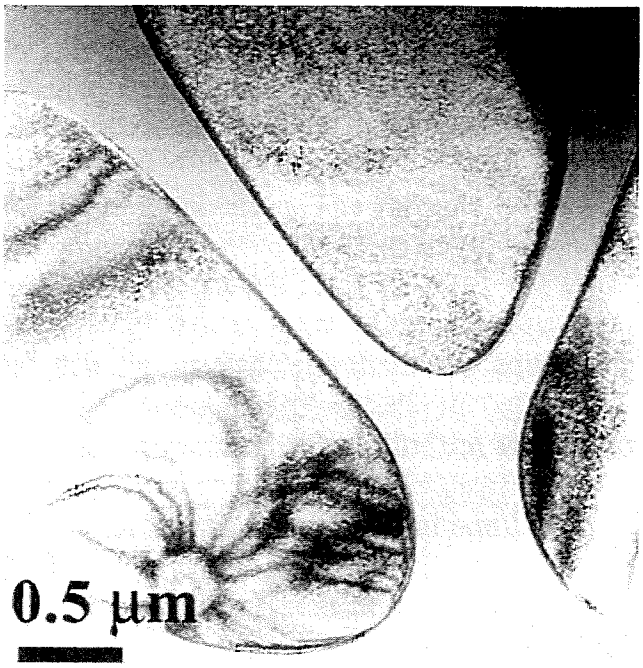

(a)

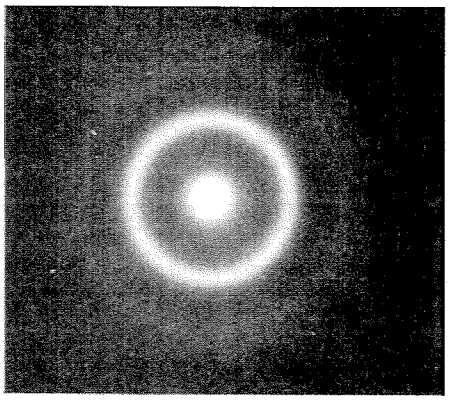

(b)

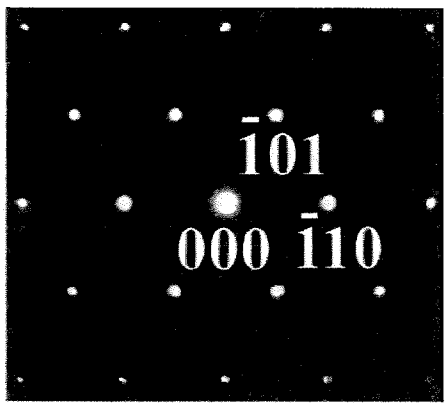

(c)

Fig. 2.10. (a) Dark field TEM image of interfacial region between amorphous matrix and β crystalline phase, (b) diffraction pattern of matrix, and (c) diffraction pattern of β crystalline phase with [111] zone axis.

partitioning, the following series of materials have been studied. These alloys are prepared by rule of mixture combinations of a metal or metal alloy with a good bulk metallic glass (Vit1) forming composition. The formula for such a mixture is given by $Vit1_{(100-X)} + M_{(X)}$, where M = Nb, Ta, Mo, and V.

Fig. 2.2 implied that liquid BMG, both in the equilibrium liquid and in the undercooled melts, can exist in metastable equilibrium with a bcc-M-based solution. The presence of the crystalline M phase in chemical equilibrium with the matrix does not catalyze the nucleation of other crystalline phases (from the Vit1 matrix). The system can be reversibly heated and cooled to alter the equilibrium volume fractions and compositions of the matrix/M phases according to a simple phase diagram and the "lever" rule. This diagram remains appropriate as long as no other crystalline phases nucleate from the melt.[15]

In situ composite alloys of this form are prepared by first melting the metal or metallic alloy with the early transition metal constituents of the BMG composition. Thus, pure Niobium metal is mixed via arc melting with Zr and Ti of the V1 alloy. This mixture is then arc melted with the remaining constituents; i.e., Cu, Ni, and Be, of the Vit1 alloy. This molten mixture, upon cooling from the high temperature melt, undergoes partial crystallization by nucleation and subsequent dendritic growth of nearly pure Nb dendrites, with a bcc structure, in the remaining liquid. The remaining liquid subsequently freezes to the glassy state producing a two-phase microstructure containing Nb rich β phase dendrites in an amorphous matrix. If one starts with an alloy composition with an excess of approximately 25 at. % niobium above a

preferred bulk metallic glass forming composition Vit1,($Zr_{41.2}Ti_{13.8}Cu_{12.4}Ni_{10.1}Be_{22.5}$), ductile niobium crystals are formed in an amorphous matrix upon cooling a melt through the region between the liquidus and solidus. Microprobe analysis shows the composition of the dendrites is about 82% (at. %) niobium, about 8% titanium, about 8.5% zirconium, and about 1.5% copper plus nickel. This is the composition found when the proportion of dendrites is about 1/4 bcc β phase and 3/4 amorphous matrix. Fig. 2.11 shows microstructure of composite of $Vit1_{75}Nb_{25}$ processed by plasma melting at temperatures ~2000 °C to produce a single phase melt.

Similar behaviors are observed when tantalum is the additional metal added to what would otherwise be a Vit1 alloy. Microprobe analysis shows the bcc-dendrite phase contains over 90 at. % of tantalum. The glassy matrix contains very low concentrations of tantalum in solid solution. Besides niobium and tantalum, suitable additional metals forming a composite via *in situ* processing include molybdenum, chromium, tungsten and vanadium. The proportion of ductile bcc forming elements in the composition can vary widely. Fig. 2.12 shows the SEM images of composite materials made of different substitution of Nb and Ta for M on $Vit1_{(100-X)} + M_{(X)}$.

This new concept of chemical partitioning is believed to be a global phenomenon in a number of bulk metallic glass forming alloy systems. For example, similar microstructure can be observed with non-Be containing alloy system. However, x-ray diffraction pattern of this composite shows that the sample contains not only ductile beta phase but also some brittle intermetallic phases.

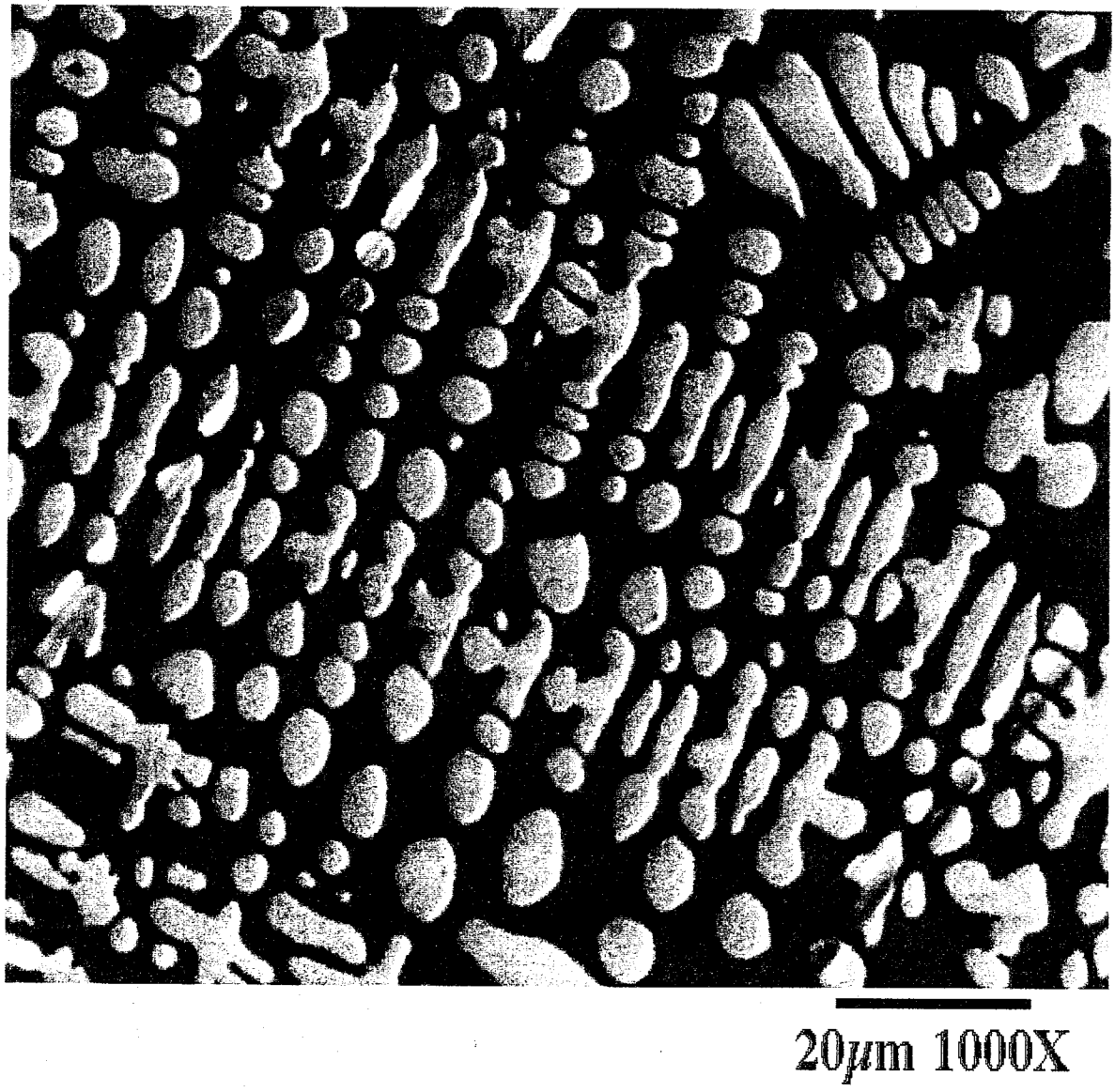

Fig. 2.11. Microstructure of chemically etched $(Vit1)_{75}(Nb)_{25}$ specimen processed by plasma arc melting.

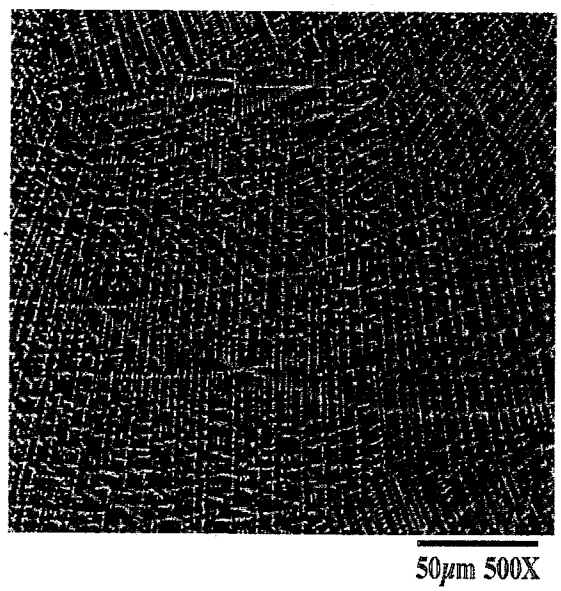

(a)

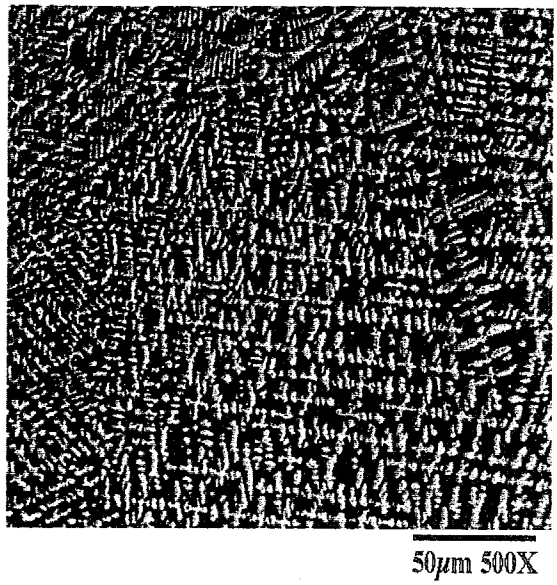

(b)

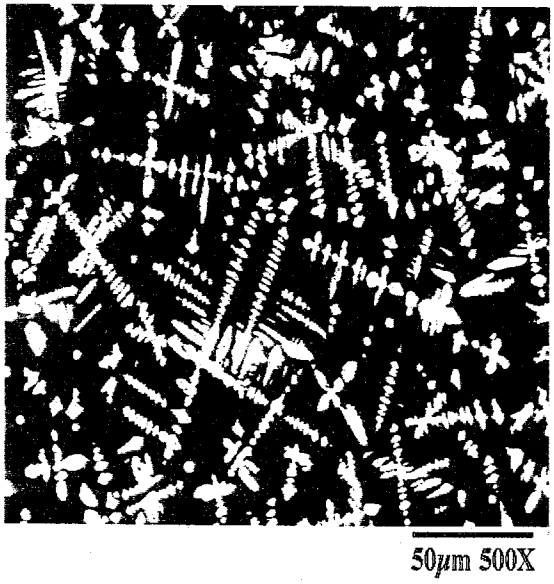

(c)

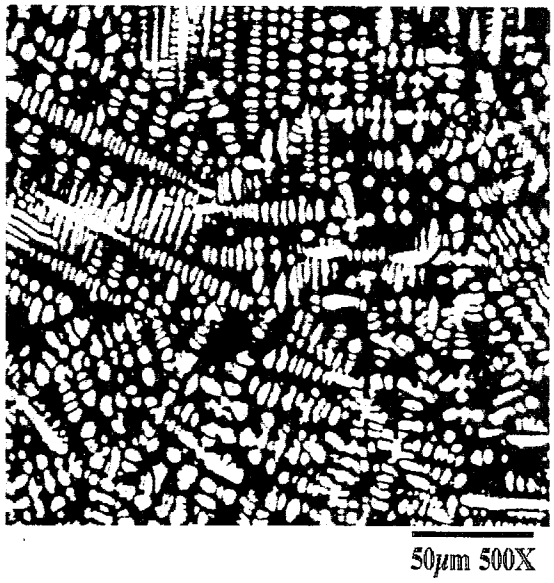

(d)

Fig. 2.12. Microstructure of chemically etched SEM images of composite materials followed by the formula $Vit1_{(100-x)}\ M_{(X)}$, where M = Nb and Ta. (a) $(Vit1)_{4/5}(Nb)_{1/5}$, (b) $(Vit1)_{2/3}(Nb)_{1/3}$, (c) $(Vit1)_{4/5}(Ta)_{1/5}$, and (d) $(Vit1)_{2/3}(Ta)_{1/3}$.

Using this method, composites with desired microstructures can be directly obtained by appropriate processing of a liquid alloy. The direction of a primary dendrite is determined by the local temperature gradient present during solidification. The principal dendrite axes extend in the direction of the steepest temperature gradient. Secondary arms form transverse to the principal axis and generally are skewed away from the cooler region. In other words, the dendrite is somewhat like the fletching on an arrow and the pointed end is toward the direction from which heat is extracted.

2.5 Designing A Technique For Controlling Orientation Of The Dendritic Structure

Fig. 2.13 illustrates schematically a technique for controlling orientation of the dendritic structure formed during chemical partitioning of a ductile metal phase in an amorphous matrix. In this embodiment a controlled temperature gradient is established by directional solidification from one end of an elongated member so that subsequently formed dendrites tend to be oriented similarly to previously formed dendrites. The process is conducted in a vacuum chamber to protect the reactive materials from oxidation or other contamination. An elongated vessel, such as a quartz tube, extends vertically in the vacuum chamber and is mounted on a feed mechanism for gradual lowering through the chamber. The tube descends through an RF induction coil, which is used to heat an alloy contained in the tube to a temperature above its melting point.

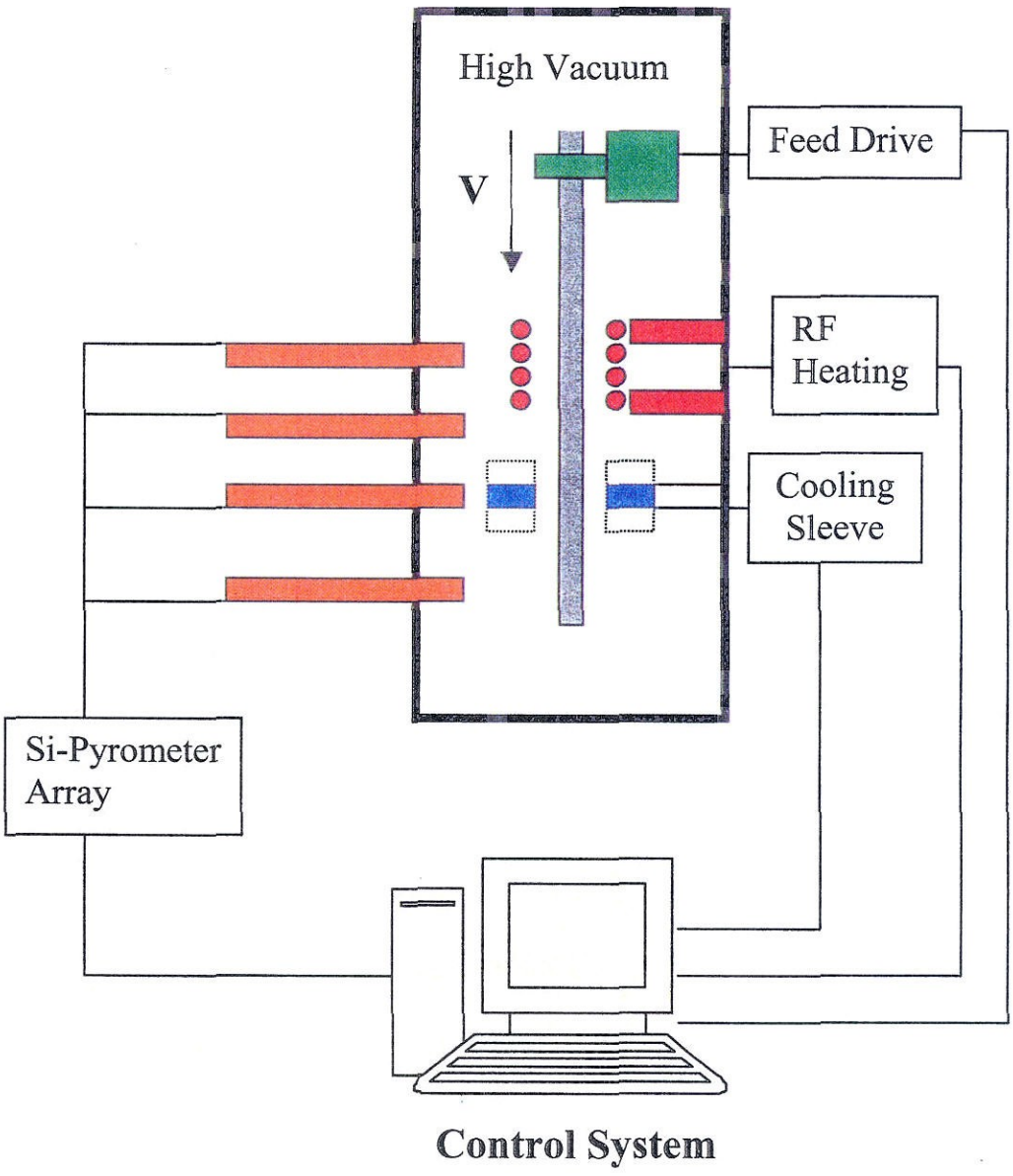

Fig. 2.13. Schematically illustrated technique for controlling orientation of the dendritic structure formed during chemical partitioning of a ductile metal phase in an amorphous matrix.

The tube then descends through one or more cooling sleeves which extract heat from the tube and alloy to initially cause partitioning and precipitation of dendrites of crystalline metal alloy from the melt. Upon further cooling the remaining melt solidifies to form an amorphous matrix surrounding the particles of ductile refractory metal. The resulting composite has dendrites oriented preferentially due to the directional solidification along the length of the metal contained in the tube. The dendrites are more or less coherent in that the principal directions of the dendrites are roughly aligned.

If desired, an additional induction heating zone may be included before the cooling sleeve for holding the alloy at a processing temperature where formation of dendrites proceeds at a controlled rate. Thus, particle size, spacing, periodicity and orientation can be controlled by both the rate of descent from the molten zone to the cooling zone and also by holding at an intermediate elevated temperature between the liquidus and solidus of the alloy.

Other techniques may be used for assuring or controlling a temperature gradient in the alloy as it cools from the melt. For example, an entire volume of metal may be melted and a temperature gradient applied by differential cooling in different portions of the melt, particularly as the alloy passes through the temperature region between the liquidus and solidus. This could take the form of cooling from only a selected surface area, for example, or by extracting heat from different areas of the surface at different rates. A plate- or sheet-like casting may be cooled preferentially from one face for selectively orienting dendrites in the composite structure, for

example, or an elongated article may be cooled from an end face for axial orientation.

This gives an opportunity to control dendrite morphology in composits with complex geometry by controlling not only the chemistry of the alloy, but also the cooling rate and direction in the temperature range between the liquidus and solidus. By increasing cooling rate, the strain to failure can be increased and by controlling direction, the orientation of dendrites can be biased toward orientations that enhanced properties of the composite and make them non-isotropic. Cold working the composite, such as by cold rolling, can also induce desirable texture.

2.6 Discussion

It is important for the crystalline phase to be ductile to support shear band propagation through the crystalline phase. Addition of small amounts of Nb (replacing Ti) in these alloys results in stabilization of the bcc-phase. If the second phase in the amorphous matrix is an intrinsically brittle ordered intermetallic compound or a Laves phase, for example, there is little ductility produced in the composite material. Ductile deformation of the particles is important for initiating and propagating shear bands. It may be noted that ductile materials in the particles may work harden, and such work hardening can be mitigated by annealing, although it is important not to exceed a glass transition temperature. This would cause the amorphous phase to crystallize.

The particle size of the dendrites of crystalline phase can also be controlled during the partitioning. If one cools slowly through the region between the liquidus and processing temperature, few nucleation sites occur in the melt and relatively

larger particle sizes can be formed. On the other hand, if one cools rapidly from a completely molten state above the liquidus to a processing temperature and then holds at the processing temperature to reach near equilibrium, a larger number of nucleation sites may occur, resulting in smaller particle size.

The particle size and spacing between particles in the solid phase may be controlled by the cooling rate between the liquidus and solidus, and/or time of holding at a processing temperature in this region. This may be a short interval to inhibit excessive crystalline growth. The addition of elements that are partitioned into the crystalline phase may also assist in controlling particle size of the crystalline phase. For example, addition of more niobium apparently creates additional nucleation sites and produces finer grain size. This can leave the volume fraction of the amorphous phase substantially unchanged and simply change the particle size and spacing. On the other hand, a change in temperature between the liquidus and solidus from which the alloy is quenched can control the volume fraction of crystalline and amorphous phases. A volume fraction of ductile crystalline phase of about 25% appears to be an optimum.

Partitioning may be used to obtain a small proportion of dendrites in a large proportion of amorphous matrix all the way to a large proportion of dendrites in a small proportion of amorphous matrix. The proportions are readily obtained by varying the amount of metal added to stabilize a crystalline phase. By adding a large proportion of niobium, for example, and reducing the sum of other elements that make a good bulk metallic glass forming alloy, a large proportion of crystalline

particles can be formed in a glassy matrix.

2.7 Conclusion

A method for forming composite materials comprising ductile crystalline metal particles in an amorphous metal matrix is provided. An alloy is heated above its liquidus temperature. Upon cooling from the high temperature melt, the alloy chemically partitions; i.e., undergoes partial crystallization by nucleation and subsequent growth of a crystalline phase. The remaining liquid, after cooling below the glass transition temperature (considered as a solidus) freezes to glassy state, producing a two-phase microstructure containing crystalline particles (or dendrites) in an amorphous metal matrix; i.e., a bulk metallic glass matrix.

This technique may be used to form a composite amorphous metal object having all of its dimensions greater than one millimeter. Such an object comprises an amorphous metal alloy forming a substantially continuous matrix, and a second ductile metal phase embedded in the matrix. For example, the second phase may comprise crystalline metal dendrites with a primary length in the range of from 30 to 150 micrometers and secondary arms with spacing between adjacent arms in the range of from 1 to 10 micrometers, more commonly in the order of about 6 to 8 micrometers.

In a preferred embodiment the second phase is formed *in situ* from a molten alloy having an original composition in the range of from 52 to 68 atomic percent zirconium, 3 to 17 atomic percent titanium, 2.5 to 8.5 atomic percent copper, 2 to 7

atomic percent nickel, 5 to 15 atomic percent beryllium, and 3 to 20 atomic percent niobium. Other metals that may be present in lieu of or in addition to niobium are selected from the group consisting of tantalum, tungsten, molybdenum, chromium and vanadium. These elements act to stabilize bcc structure in Ti- and Zr-based alloys.

References

1. Y.J. Kim, R. Busch, W.L. Johnson, A.J. Rulison, and W.K. Rhim, Appl. Phys. Lett. **65**, 2136 (1994).
2. H.A. Bruck, T. Christman, A.J. Rosakis, and W.L. Johnson, Scripta Metallurgica Et Materialia. **30**(4),429 (1994).
3. H.A. Bruck, A.J. Rosakis, and W.L. Johnson, Journal of Materials Research. **11**(2),503 (1996).
4. A.T. Alpas and J.D. Embury, Scripta Metallurgica. **22**(2), 265 (1998).
5. R.B. Dandliker, R.D. Conner, and W.L. Johnson, J.Mater. Res. **13**, 2896 (1998).
6. R.D. Conner, R.B. Dandliker, and W.L. Johnson, Acta Mater.**46**,6089 (1998).
7. H. Choi-Yim, R.Busch, U. Koster, and W.L. Johnson, Acta Mater.**47**,2455 (1999).
8. H. Choi-Yim and W.L. Johnson, Appl. Phys. Lett.**26**,3808 (1997).
9. R.D. Conner, H. Choi-Yim, and W.L. Johnson, J. Mater. Res.**14**,3292 (1999).
10. H. Choi-Yim, R. Busch, and W.L. Johnson, J.Appl. Phys.**83**, 7993 (1998).
11. J. Schroers, K. Samwer, F. Szuecs, and W.L. Johnson, J. Matr. Res.**15**, 1617 (2000).
12. C.C. Hays, C.P. Kim, and W.L. Johnson, Physical Review Letters.**84**(13), 2901 (2000).
13. F. Szuecs, C.P. Kim, and W.L. Johnson, accepted for publication in Acta Mat. (2000).
14. L. Azaroff and M.J. Buerger, The Power Method in X-Ray Crystallography, McGraw-Hill, New York, 238 (1958).

15. R. Dandliker, Ph.D. thesis, "Bulk Metallic Glass Matrix Composites-Processing, Microstructure, and Applications", California Institute of Technology, submitted October 1997.

Chapter 3. Mechanical Properties of Composite Materials

3.1 Introduction

The $Zr_{41.2}Ti_{13.8}Cu_{12.5}Ni_{10}Be_{22.5}$ (Vit1) bulk metallic glass exhibits an exceptional glass forming ability with a critical cooling rate of ~ 1 K/s, which makes it a very interesting material for structural applications.[1] This has motivated a series of investigations of its mechanical properties.[2-4] The Vit1 alloy shows a tensile strength of 1.9 GPa, and an elastic strain limit of 2% under compressive or tensile loading. Plain strain fracture toughness measurements on Vit1 have revealed values between K_{1C} = 18 to 55 MPa$\sqrt{m}$ [4-6], depending on purity and residual stresses of the tested materials. However, Vit1, as all other metallic glasses, fails by the formation of highly localized shear bands, which leads to catastrophic failure under unconstraint conditions without much macroscopic plasticity.[2,3,7] This quasi-brittle deformation behavior has limited the application of bulk metallic glasses as an engineering material so far. The preparation of bulk metallic glass matrix composites with ductile metal and refractory ceramic particles as reinforcements has yielded improvements in tensile and compressive strains to failure.[8-10] The increase in compressive toughness has been attributed to the following: 1) restricting shear band propagation, 2) the generation multiple of shear bands, and 3) creation of additional fracture surface area.[5] The composite reinforcement was added to the bulk metallic glass alloy by melting the glass-forming metal and introducing pieces of reinforcement into the molten alloy, which is then solidified at a rate sufficiently high that the metal matrix is

amorphous. Alternatively, a mass of pieces of the reinforcement material are infiltrated under positive gas pressure by the molten glass-forming alloy and then cooled; e.g., high volume fraction tungsten fiber composites with a Vit1 matrix. Both of these methods lack sufficient control of the secondary reinforcing particle size and spacing needed to adequately constrain the bulk metallic glass matrix such that multiple shear bands are formed during mechanical loading. The interfaces between the particles and matrix are not chemically homogeneous, leading to higher internal energy and less effective strain transfer. Recent work by Leonard et al. for a Zr-based amorphous alloy shows that the ductility of as-cast specimens with two-phase, amorphous and crystalline, microstructures are seriously degraded. In an annealed $Zr_{57}Ti_5Cu_{20}Ni_8Al_{10}$ alloy with micrometer sized intermetallic crystalline precipitates, it was observed that the brittle fracture was initiated at the crystals when the precipitate size was larger than the shear band width, W.[11]

Multiple shear bands are observed when the catastrophic instability is avoided by mechanical constraints. In this chapter a new ductile metal reinforced bulk metallic glass material is prepared via an cost effective *in-situ* processing method[12,13], and this composite exhibits large compressive and tensile strains to failure and a strongly improved impact toughness compared to other metallic glass materials. In the niobium enriched Zr-Ti-Cu-Ni-Be system, the microstructure resulting from dendrite formation from a melt comprises a stable crystalline Zr-Ti-Nb alloy, with β phase (body centered cubic) structure, in a Zr-Ti-Nb-Cu-Ni-Be amorphous metal matrix. These ductile crystalline metal particles distributed in the amorphous metal matrix

impose intrinsic geometrical constraints on the matrix that leads to the generation of multiple shear bands under mechanical loading.

3.2 Experimental Procedure

Mechanical test specimens, (C, M, and B) were prepared in the form of 25g rods with 10 mm diameter and 50 mm length by plasma arc melting in a Ti-gettered argon atmosphere on a water-cooled copper plate. Then, these specimens are machined into the geometry with dimensions proportional to ASTM standard of each mechanical testing. The sample "C" is plasma arc melted composite material, "M" is monolithic matrix alloy, and "B" is monolithic β phase alloy. The chemical compositions of monolithic matrix and β phase were determined using a JOEL JXA-73 electron microprobe analyzer with the elements of Zr, Ti, Nb, Cu and Ni as standards, whereas the Be content was calculated by difference.

Also, commercially cast 3.3 mm thick plates, labeled as material "H", with the same composition as for alloy "C" was used. All investigated compositions are shown in Table 3.1 together with a summary of X-ray diffraction and ultrasonic sound velocity measurements results. Scanning electron microscopy (SEM) was used for the analysis of the as-cast microstructure and of fracture surfaces using a Camscan Series II.

Ultrasonic sound velocity measurements were performed to obtain room-temperature Young's modulus, shear modulus and Poisson ratios of the specimens

using the standard procedure, and the mass densities were measured according to the hydrostatic weighing technique. Measurements were made on a 7 mm diameter cylindrical rod 10 mm in length whose ends were mechanically polished with 600 grit SiC abrasive paper using a V-block to insure flat and parallel surfaces. Ultrasonic measurements were made using a Parametrics Model 5052UA ultrasonic analyzer connected to an oscilloscope for data analysis. Two ultrasonic transducers were placed on the ends of the rod. One transducer was used to measure the dilatational wave speed while the other measured shear wave speeds. The wave speeds were calculated by measuring the time it took for a pulse to travel from one end of the specimen to the other and back, and then dividing by twice the specimen length.

Elastic properties can be calculated from the measured wave speeds using the following equations.[14]

$$c_S = \sqrt{\frac{\mu}{\rho}}$$

$$c_L = \sqrt{\frac{\lambda + 2\mu}{\rho}}$$

Where C_S is the shear wave speed, C_L is the dilatational wave speed, μ is the shear modulus, λ is Lame's constant, and ρ is the density. The elastic properties are often given in terms of Young's modulus, $E = \frac{\mu(3\lambda + 2\mu)}{(\lambda + \mu)}$, and Poisson's ratio, $\upsilon = \frac{\lambda}{2(\lambda + \mu)}$.

Sample	Composition [at.%]	Phases	C_S [m/s]	C_L [m/s]	δ [g cm^{-3}]	E [GPa]	μ [GPa]	ν
Vit1	$Zr_{41.2}Ti_{13.8}Cu_{12.5}Ni_{10}Be_{22.5}$	BMG	2426	5118	6.1	97.2	35.9	0.355
C and H	$Zr_{56.2}Ti_{13.8}Nb_{5.0}Cu_{6.9}Ni_{5.6}Be_{12.5}$	BMG + bcc	2132	4771	6.3	78.8	28.6	0.375
M	$Zr_{47}Ti_{12.9}Nb_{2.8}Cu_{11}Ni_{9.6}Be_{16.7}$	BMG	2270	4990	6.3	89.2	32.6	0.369
B	$Zr_{71}Ti_{16.3}Nb_{10}Cu_{1.8}Ni_{0.9}$	bcc	1870	4604	6.5	63.3	22.7	0.401

Table 3.1: Phases analyzed by X-ray diffraction (bcc: body centered cubic, BMG: bulk metallic glass), mass densities by the Archimedes method, Young's modulus, shear modulus and Poisson ratios resulting from ultrasonic sound velocity measurements for samples with given chemical compositions. Materials C, M, and B were prepared at Caltech, H and Vit1 at Howmat Corporation.

3.3 Mechanical Properties

3.3.1 Compression Test

An Instron 4202 load frame was used to test two or three specimens of each type at room-temperature under uniaxial compression loading. The compression test specimens were machined to 6 mm in length, either cylindrical with 3 mm diameter or rectangular with 3 x 3 mm cross section and polished plane to parallel to promote an accuracy. The compression specimens were sandwiched between two WC platens in a loading fixture designed to guarantee axial loading. Also, the ends of the compression specimens were lubricated with "Molygraph Extreme Pressure Multi-

purpose" grease to prevent "barreling" of the sample. All of the compression tests were conducted using constant strain rates varying between 10^{-6} and 10^{-4} /sec.

Fig. 3.1 shows uniaxial compressive stress strain curves typical for the composite material H and the single phase materials M and B. Under quasi-static compressive loading, all materials exhibit a Young's modulus very close to the results measured with the ultrasonic sound method (Table 3.1). The ultrasonic Young's moduli decrease from 97.2 GPa for Vit1 to 89.2 GPa for the monolithic matrix composition M and to 78.8 GPa for the composite sample C. For the monolithic β phase sample B the drop in Young's modulus (63.3 GPa) is even more pronounced and especially the shear modulus of 22.7 GPa reaches a very low value. This indicates that the β phase structure is unstable against shear.

The stress strain curve for the composite lies between the obtained results for the corresponding monolithic matrix and bcc phase materials as shown in Fig.3.1. While the matrix material (M) fails without showing significant plastic deformation, the monolithic bcc phase material (B) yields already at 550 MPa followed by a plastic region with significant work hardening behavior. Much higher average fracture strains of ~ 8% in compression were reached for the composite samples C and H. The yield stress of 1500 MPa were achieved for sample H in compression with corresponding elastic limit of 2.02%. This yield stress of composite material is approximately 14% lower than the yield stress for Vit1 of 1.74 GPa; however, the strains in this

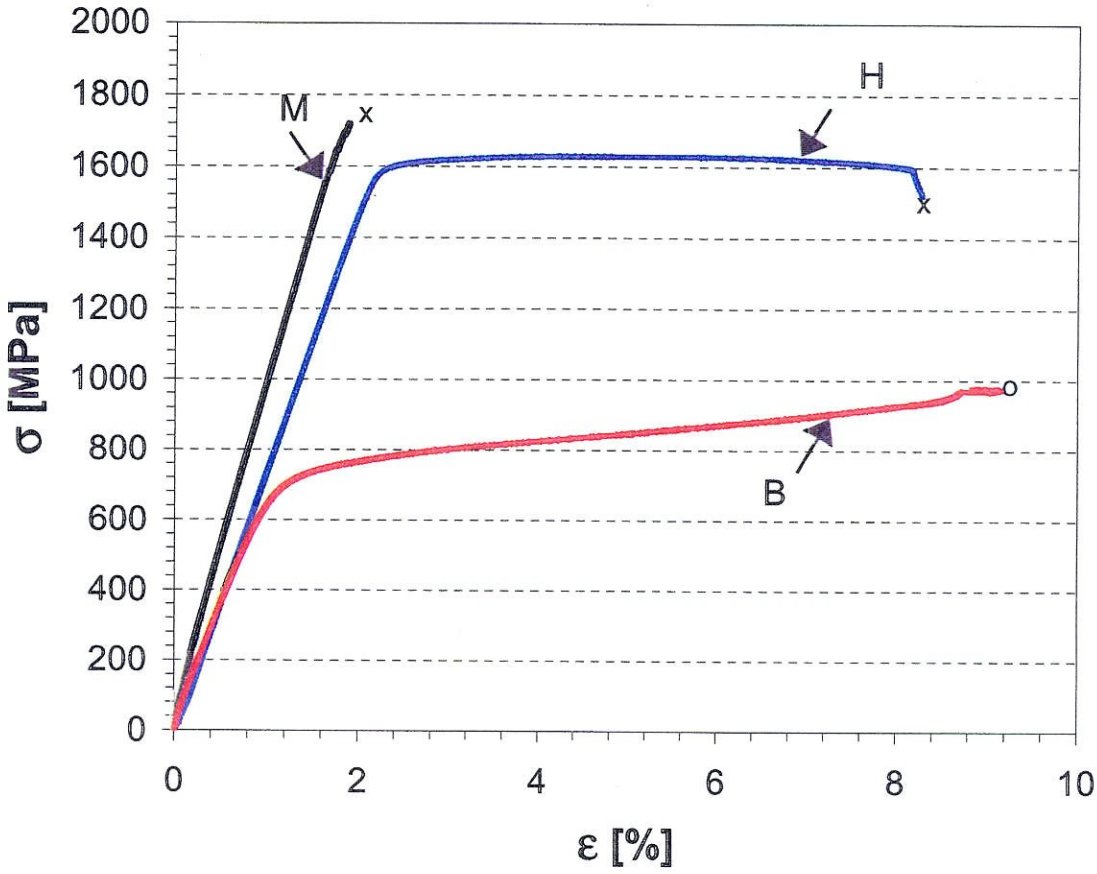

Fig. 3.1. Uniaxial compressive stress strain curves for the composite material H and the monolithic phase materials M and B. Symbol x on the M and H specimens represents fractured point, and symbol o on the specimen B represents stopped experiment without fracturing the sample.

composite material exhibit enormous increase in ductility leading to a failure strain of 8.26%. Note that the strain at yield point of composite material is almost same for the Vit1 of 2%. Under the same testing condition, the Vit1 sample fails catastrophically along a single or small number of shear bands with no plasticity. Beyond the elastic strain limit of 2.02%, the β phase yields and deforms, and shear bands patterns develop, as the glassy matrix is locally loaded beyond its critical shear stress. We believe that critical loading of the glass develops when plastic yield of the β phase transfers local stress concentrations to the surrounding glass. On further deformation, an apparent strain hardening behavior is seen. We presume this to be related to the strain hardening behavior of the β phase which tends to arrest local deformation. The apparent work hardening above a strain of 2% follows a linear behavior until ultimate compressive strength of 1670 MPa. This behavior is not observed in bulk metallic glasses, which normally show strain-softening behavior beyond the elastic limit.

The monolithic bulk metallic glass materials (samples Vit1 and M) show linear elastic behavior up to yield stresses of 1600 to 1750 MPa in compression test with elastic strain limit of 2%. They fail quasi-brittle showing only minor plasticity up to fracture strains of ~ 3.3% in compression. Compared to Vit1, the matrix sample M has slightly degraded mechanical properties with lower Young's modulus, yield and fracture stress, and lower fracture strains.

Measurements on the monolithic β phase material B show high ductility. The yield stress is only 540 ~ 550 MPa. After extended work hardening, an ultimate

strength of ~ 1000 MPa at a strain of ~13% is measured. The compressive test runs on specimen B were stopped at total strains of 9% without reaching fracture, because the test specimen were losing their cylindrical shape.

A unique feature of the stress strain data was observed for material B in the plastic region. The stress values plotted over time show slight sinusoidal fluctuation of the yield stress with ongoing plastic deformation (Fig. 3.2.), which is clearly a material specific behavior and not caused externally. Such a behavior is commonly called serrated flow, but it clearly differs from the serrated flow observed in bulk metallic glasses, which is characterized in sudden load drops at each progression of a slip band (Fig. 3.3.). The composite materials H and C also show similar yield stress fluctuations with ongoing deformation as material B, but at much higher stress levels (Fig. 3.4.). Table 3.2 summarizes the compression test results.

The SEM analysis of plastically deformed regions and the fracture surfaces show significant differences for the composite materials compared to monolithic bulk metallic glasses. As shown in Fig. 3.5, the fracture surfaces are still oriented under a global 45 ^{o} angle to the loading axis. However, in higher magnification we see that the fracture surface of the composite is more complex showing some regions with "vein pattern" morphology characteristic, as also seen for Vit1, together with other large regions (~ 50 – 100 μm) which appear to have undergone extensive melting (larger melt pools) and resolidification. This provides evidence of enormous heat

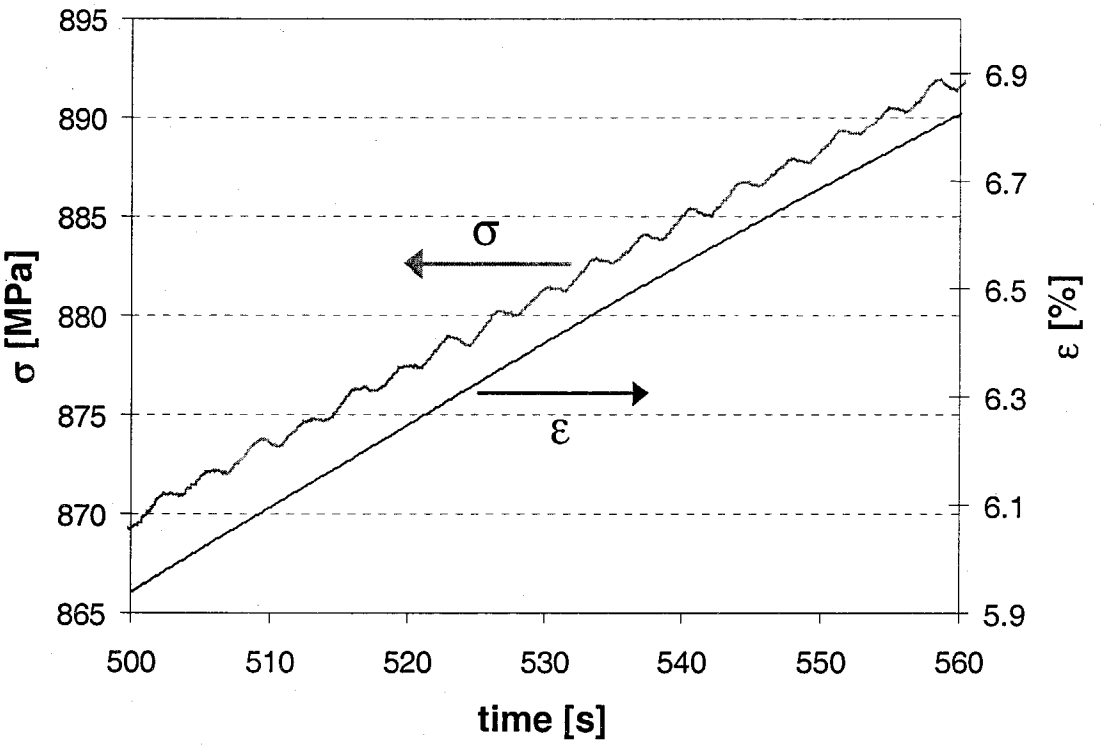

Fig. 3.2. Compressive stress and strain data of the plastic region plotted over time for the monolithic β phase sample B. Work hardening behavior with fluctuations in the yield stress is observed with ongoing plastic deformation.

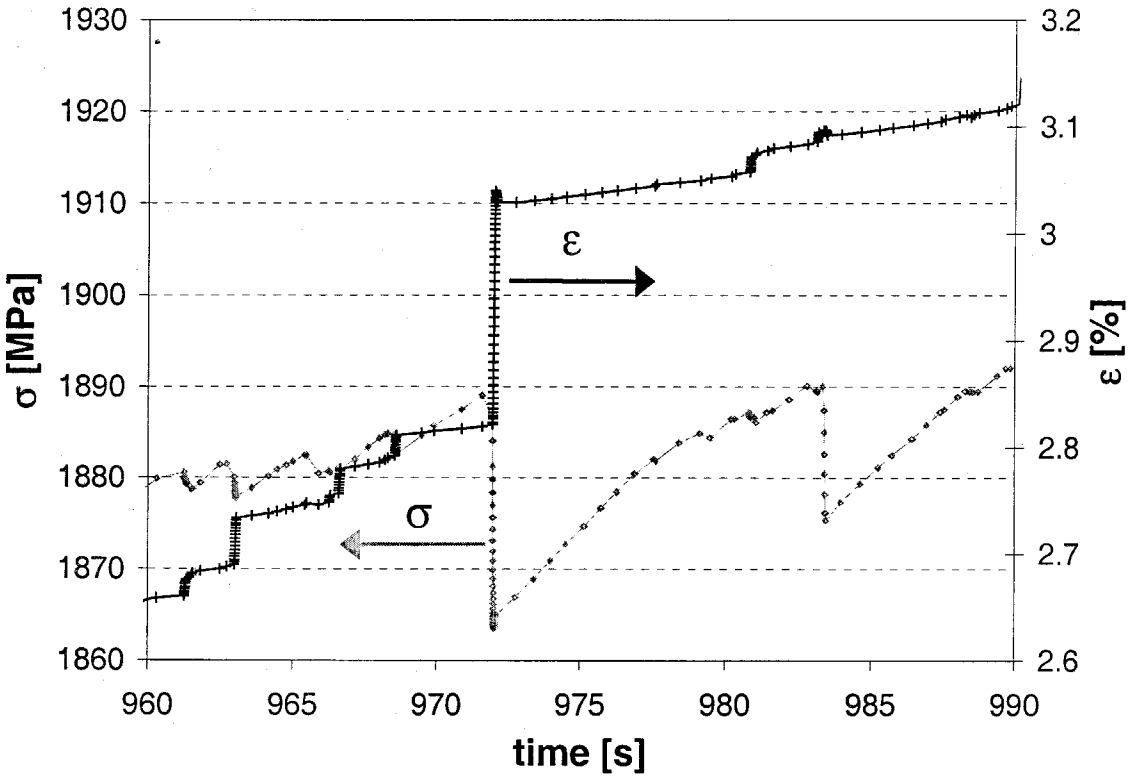

Fig. 3.3. Compressive stress and strain data of the plastic region plotted over time for the monolithic matrix sample M. Serrated flow behavior with sudden stress drops during single slip events is observed.

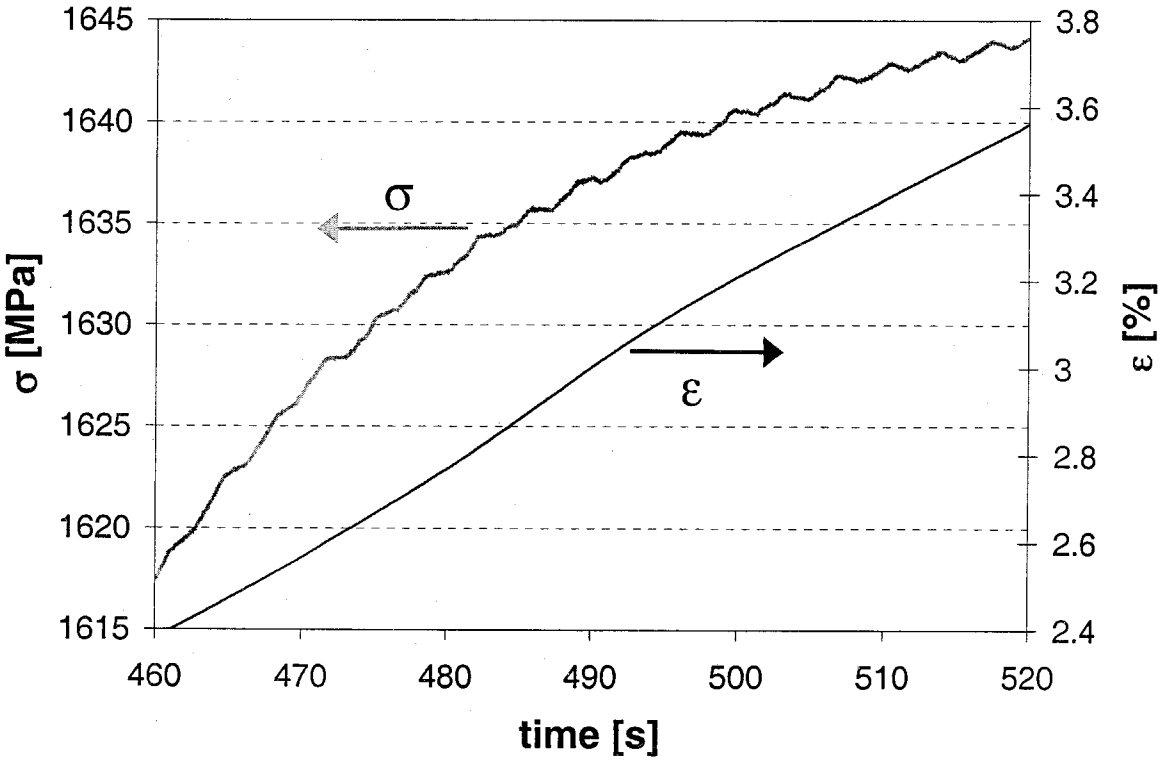

Fig. 3.4. Compressive stress and strain data of the plastic region plotted over time for composite sample H. Same fluctuations in yield stress as for material B is observed, but at much higher stress values.

	Sample	E [Gpa]	σ_y [Mpa]	ε_y [%]	σ_{max} [Mpa]	$\varepsilon_{@max}$ [%]	ε_f [%]	$(d\varepsilon/dt)_{pl}$ [s^{-1}]
Compression	Vit1-4	96.3	1637	1.83	1755	2.09	2.09	---
	Vit1-5	98.4	1742	1.76	1899	3.33	3.33	$3.2\ 10^{-5}$
	H-4	80.1	1545	1.90	1669	4.70	Stopped	---
	H-5	78.4	1520	1.97	1646	4.04	6.32	$1.3\ 10^{-4}$
	H-6	75.0	1480	2.02	1628	5.90	8.26	$9.5\ 10^{-5}$
	M-1	92.5	1588	1.67	1715	1.89	1.89	---
	M-2	84.0	1593	1.60	1644	1.66	1.66	---
	B-1	65.2	550	0.80	Stopped at $\varepsilon \sim 9\%$			$1.7\ 10^{-4}$
	B-2	60.5	540	0.87	1006	13.4	Stopped	$5.2\ 10^{-4}$

Table 3.2: Summary of compressive test data. Samples of C,M and B were prepared at Caltech, Vit1 and composite H were cast at Howmet Corporation. Young's modulus E, yield stress σ_y, strain at the yield point ε_y, ultimate strength σ_{max} and strain at ultimate stress $\varepsilon_{@max}$, as well as fracture strain ε_f are listed. For samples with pronounced plasticity, the average strain rate in the plastic region $(d\varepsilon/dt)_{pl}$ is given as well. Test runs on samples H-4, B-1, and B-2 were stopped without reaching fracture.

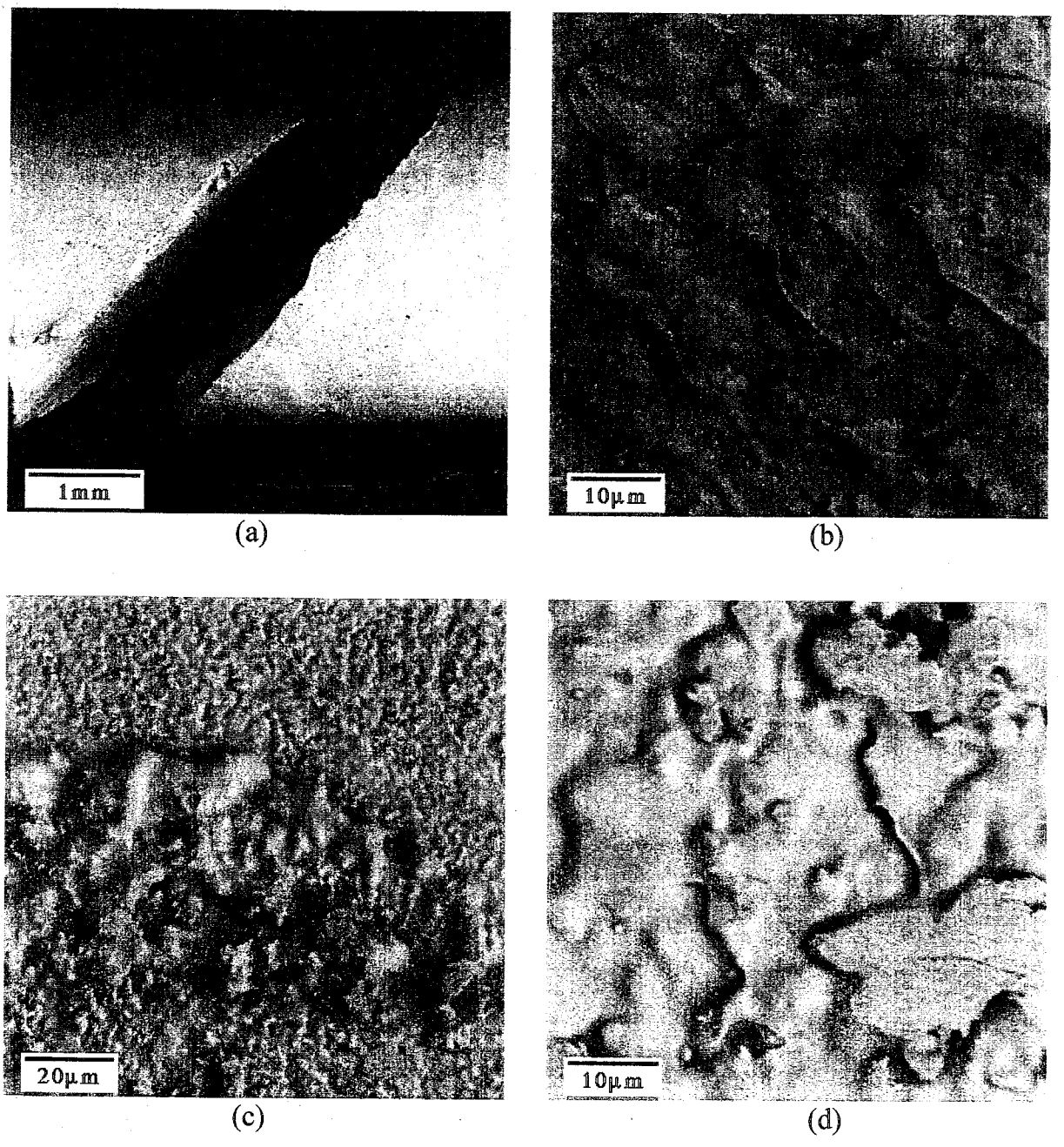

Fig. 3.5. SEM images of fractured composite material after compression test. (a) fracture angle is oriented under a global 45° to the loading axis, (b) vein pattern morphology, (c) and (d) large regions are undergone extensive melting and resolidification when it fractured.

dissipation in relatively large (100 μm) local areas along the failure surface.

A shear band pattern develops on the fractured side of the compression test specimens as the glassy matrix is locally loaded beyond it's critical shear stress. The critical loading of the glass matrix develops when plastic yield of the β phase transfers local stress concentrations to the surrounding glass. The side view on a prior to testing polished surface of a compression specimen shows increasingly dense patterns of multiple shear bands as we come close to the fracture surface as shown on Fig. 3.6.

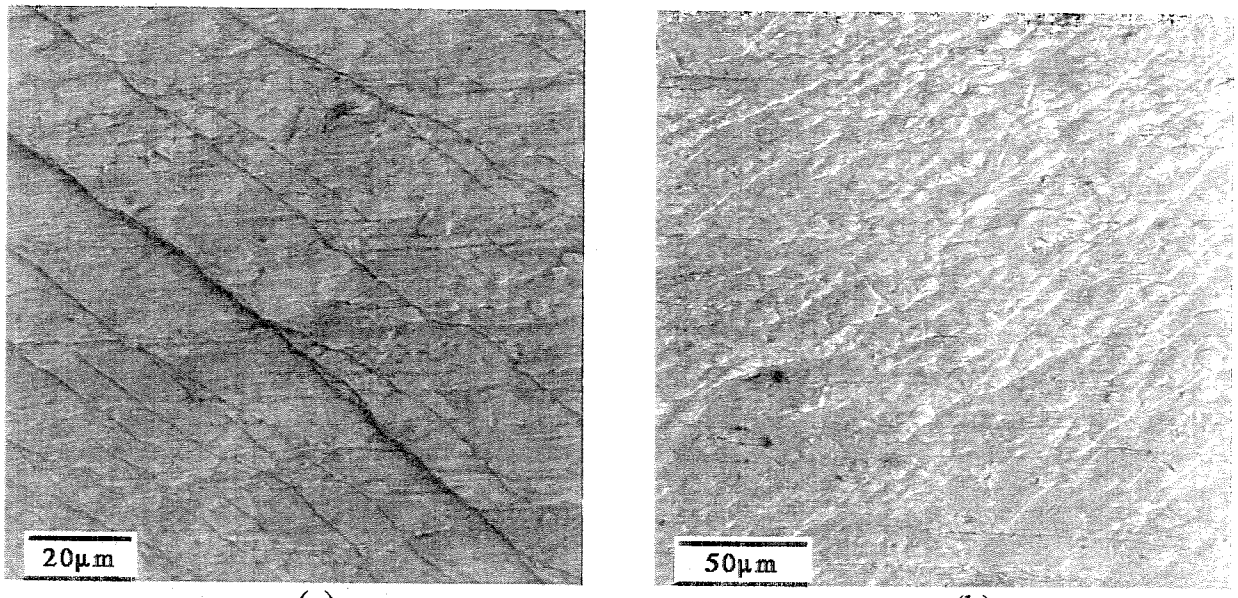

(a) (b)

Fig. 3.6. SEM images of side view on a composite compression test specimen.
(a) many small cracks showing on the surface of specimen, and (b) multiple shear bands formed on the surface of specimen.

3.3.2 Tensile Test

The tensile test specimens were prepared in the form of 25g rods with 10 mm diameter and 55 mm length by plasma arc melting in a Ti-gettered argon atmosphere on a water cooled copper plate. These rods were machined into a dog-bone geometry with dimensions proportional to ASTM standard E8-68 for tension testing. Howmet tensile test specimens were machined to pin hole dog-bone shape with rectangular cross section area. Uniaxial strain gages from Micromeasurements Group were glued on the surface of the specimen's gage section in order to obtain one-dimensional surface strains.

The tension tests were performed in the same Instron 4202 load frame as used to conduct quasi-static compression test. However, the tensile specimens were connected by universal joints to the load frame in order to reduce the bending moments transmitted to the specimen. All of the tensile tests were conducted using constant crosshead velocities which resulted in strain rates varying from 10^{-6} to 10^{-5} /sec.

Fig. 3.7 shows three different tensile stress strain curves for Howmet Corporation cast Vit1, the $(Zr_{75}\ Ti_{18.34}Nb_{6.66})_{75}((Cu_{55}Ni_{45})_{50}Be_{50})_{25}$ composite produced by plasma arc melting "C," and the Howmet Corporation cast composite of same composition "H." Compared to the monolithic Vit1, which exhibits essentially no ductility and fails catastrophically by the propagation of a single shear band with plastic strain of 0.1% or less, a dramatically enhanced

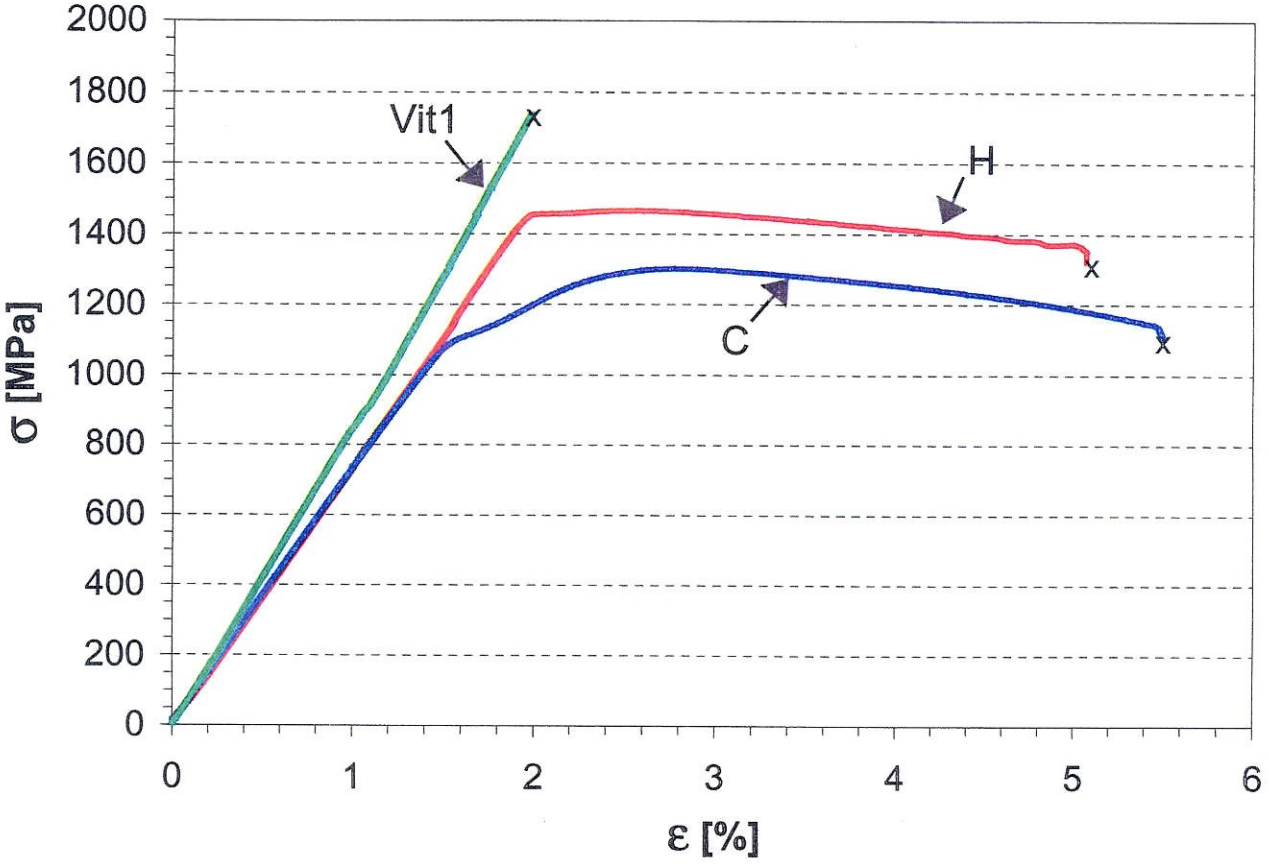

Fig. 3.7. Tensile stress strain curve for Vit1 and the two composite materials C and H. Symbol x on the plot represents fractured point.

total strain of up to 5.5% was observed in tension prior to failure. Clear necking of the tensile specimen was observed, with a plastic strain of 15% at the necked region. Fig. 3.8 shows SEM image of necked region of test specimen after loading.

The composite material produced by plasma arc melting (C) exhibits a Young's modulus E= 73 GPa and yields at σ_Y = 1.1 GPa, with a corresponding elastic strain limit ε_Y = 1.6% whereas the Howmet Corporation cast composite of the same composition (H) exhibits higher yield stress of 1.4 GPa with a corresponding elastic strain of ε_Y = 1.97%. Table 3.3 shows summarized tensile test results of Vit1 and β phase containing BMG composites. A work hardening behavior is observed on the composite sample test. In the range of applied strain rates no significant strain rate sensitivity is detected.

The side view of a mirror polished surface of a tensile specimen prior to testing shows increasingly dense patterns of multiple shear bands as we come closer to the fracture surface (Fig. 3.8). The shear band pattern arrays were observed over the entire surface of the deformed tensile specimen. The shear band patterns were oriented on habit planes at ± 45° from the tensile axis. The pattern periodicity as viewed normal to the slip direction was λ_s = 6 – 7 μm, similar to those observed in the bend and compression test specimens. Deformation under uniaxial tension apparently occurs in the same manner as under bending and compressive loading.

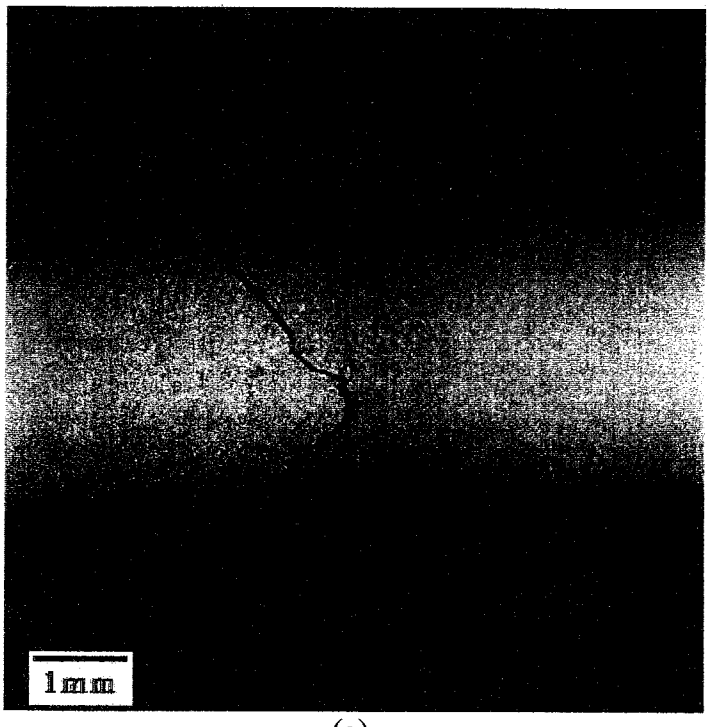

(a)

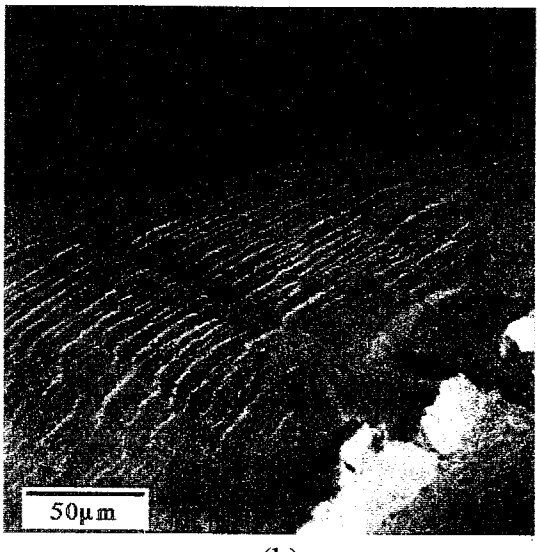

(b)

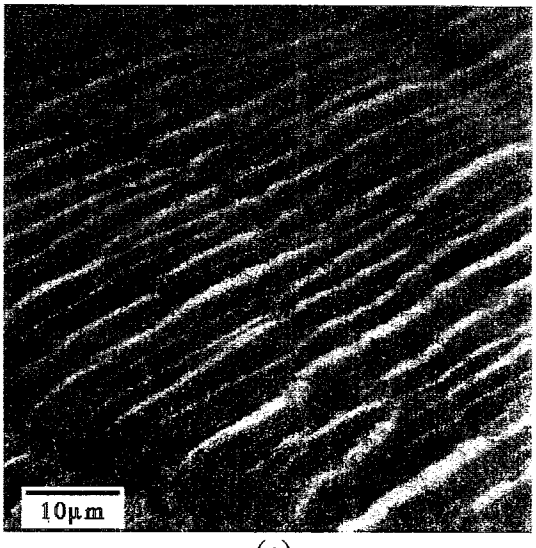

(c)

Fig. 3.8. SEM images of composite specimen after tensile test. (a) fractured region shows necking when it deformed, (b) multiple shear bands are formed on the side of the specimen, and (c) magnified image of multiple shear bands formed during deformation.

	Sample	E [Gpa]	σ_y [Mpa]	ε_y [%]	σ_{max} [Mpa]	$\varepsilon_{@max}$ [%]	ε_f [%]	$(d\varepsilon/dt)_{pl}$ [s^{-1}]
Tension	Vit1-1	86.9	---	---	1737	1.98	1.98	---
	Vit1-2	88.4	---	---	1571	1.80	1.80	---
	Vit1-3	84.3	---	---	1525	1.80	1.80	---
	H-1	71.4	1450	2.07	1486	3.03	4.54	$9.4\ 10^{-5}$
	H-2	72.6	1420	1.97	1487	2.93	4.85	$8.0\ 10^{-6}$
	H-3	74.2	1410	1.90	1465	2.57	5.07	$9.3\ 10^{-5}$
	C-1	71.1	1114	1.58	1296	2.64	4.74	$8.8\ 10^{-5}$
	C-2	72.7	1100	1.53	1327	2.82	5.00	$8.8\ 10^{-5}$
	C-3	72.4	1064	1.48	1302	2.70	5.49	$1.0\ 10^{-4}$

Table 3.3: Summary of tensile test data. Sample C was prepared at Caltech. Vit1 and composite H were cast at Howmet Corporation. Young's modulus E, yield stress σ_y, strain at the yield point ε_y, ultimate strength σ_{max} and strain at ultimate stress $\varepsilon_{@max}$, as well as fracture strain ε_f are listed. For samples with pronounced plasticity the average strain rate in the plastic region $(d\varepsilon/dt)_{pl}$ is given as well.

For the metallic glass containing materials Vit1, C, and H, the Young's moduli determined from the tensile stress strain curves are constantly about 10% lower compared to results from compression testing and ultrasonic sound measurements. The differences in the elastic modulus can possibly be explained by a mean stress dependence of the elastic behavior for metallic glasses. The yield stresses in

compression are constantly higher than in tension, which again indicates a mean stress sensitivity. Bruck et al.[1] have established that there is no difference between compressive and tensile yield strengths and concluded a von Mises yield criterion, whereas Donovan[15] investigated a Pd glass and concluded that it follows a Mohr-Coloumb yield criterion. Our results confirm that the investigated bulk metallic glass materials do not follow a von Mises yield criterion.

3.3.3 Three Point Bend Test

Non-instrumented three point bend test specimens are prepared from both composite materials "C" and "H." Bend test specimens are tested in the form of 2 mm by 10 mm by 30 mm beam shaped plate on the fixture shown on Fig. 3.9. The test results show that the *in situ* composite undergoes a plastic strain ε_p = 5% before failure as determined by the permanent radius of curvature of the sample following fracture. A monolithic metallic glass specimen of this size fails catastrophically by the propagation of a single shear band with no measurable global plasticity under identical loading. The mechanism responsible for this plasticity is seen in the SEM images of Fig. 3.10. Fig. 3.10.a. shows a low magnification image of the bend test specimen viewed normal to the bending direction. The permanent bend radius is seen along with a very rough fracture surface exhibiting mode I and mode II (45° shear failure) failure surfaces. Fig. 3.10.b. shows a higher magnification image of a region near the failure surface.

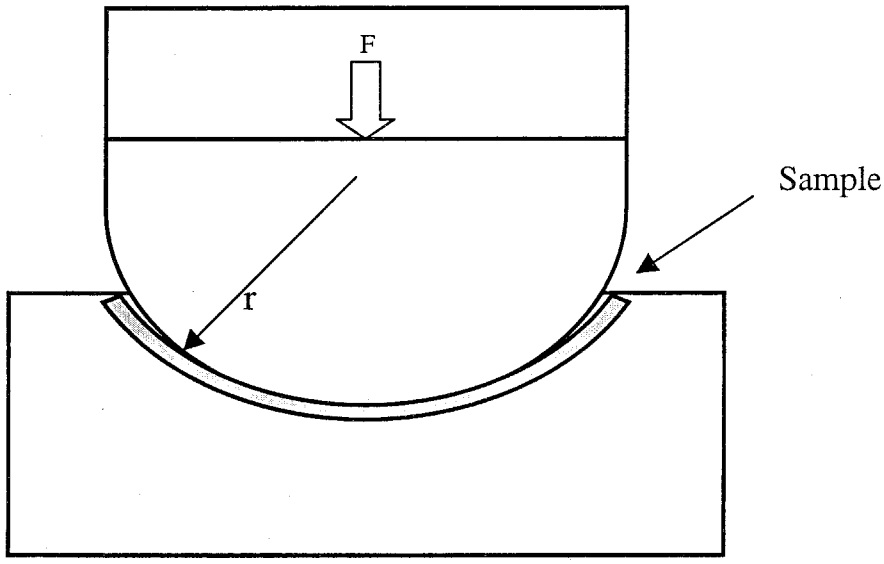

Fig. 3.9. Geometry of bend test fixtures. A specimen is bent between the concave and convex molds of radius r. The maximum strain in the specimen is: E = t / 2r where t is the thickness of the specimen. A series of molds of 0.5", 0.75", 1.0", and 1.5" radii's are used.

Patterns of regularly spaced shear bands are seen throughout the region. Pattern domains have a spatial extent of ~ 100 μm. Within each domain, a regular array of parallel shear bands is observed at a spacing of typically $\lambda = 7 \sim 8$ μm. This spacing coincides with the secondary arm spacing of the β phase dendrites. The bands occur on habit planes oriented roughly at 45° to the tensile and compressive surfaces of bending (directions of maximum resolved shear stress in bending). Note that in areas where dendrite arms are normal to the surface, the shear bands preferentially propagate through the arms with slip apparently localized in a plane cutting through the arms. A variety of geometrical correlations can be seen between the shear bands and dendrites. Fig. 3.10.c. shows a still higher magnification image of a "domain" of shear bands where the dendrite arms are predominantly normal to the surface. The shear bands propagate preferentially through many successive dendrite arms (often over the entire domain), occasionally initiate or terminate within the arms, and clearly propagate as localized bands through the β phase arms. Coalescence voids are observed along individual shear bands (see point A on Fig. 3.10.c.) and at the interface between the ductile particle and the glassy matrix (see point B on Fig. 3.10.c.). Shear offsets at the ductile particle/glassy matrix interface of 0.5 μm are observed with shear band widths W of the same order (see point C on Fig. 3.10.c). Therefore, the plastic strains within a single typical shear band are $\varepsilon_p^{band} = 1$. The total plastic strain can be estimated as $\varepsilon_{total} = W/\lambda_s = 4\%$, in excellent agreement with the overall plastic strain in the specimen as determined by the plastic bend radius. In a

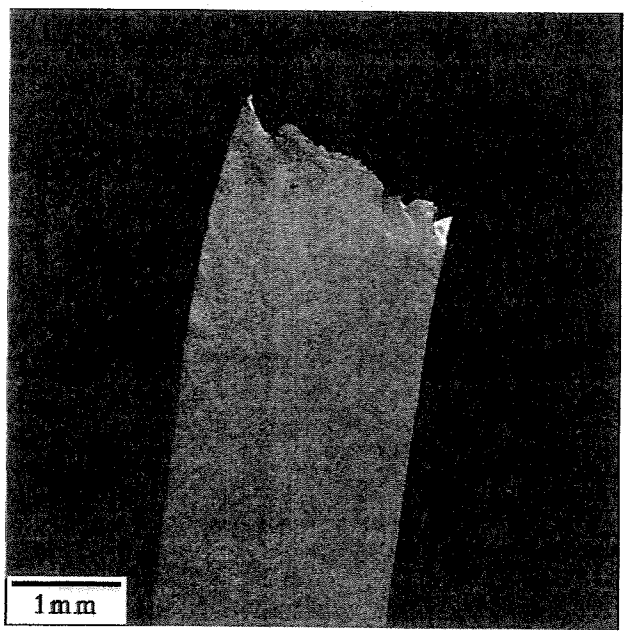

(a)

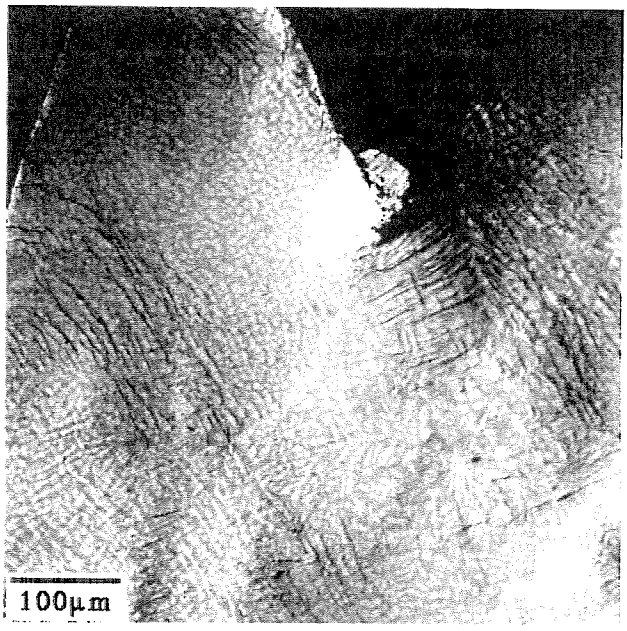

(b)

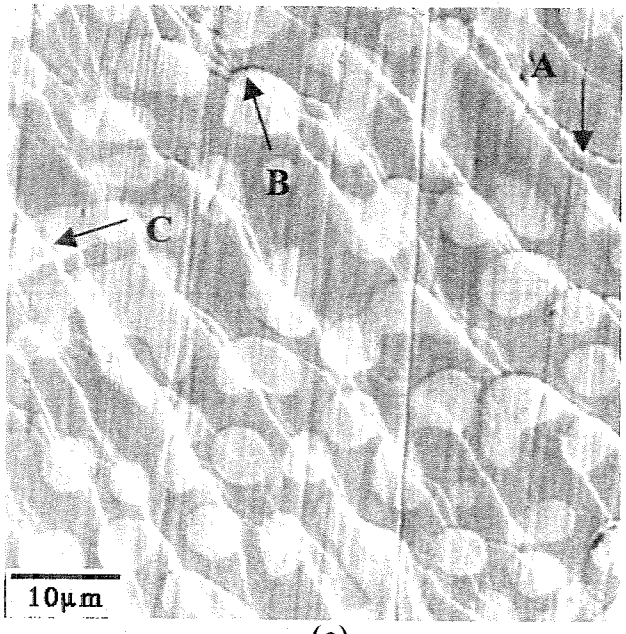

(c)

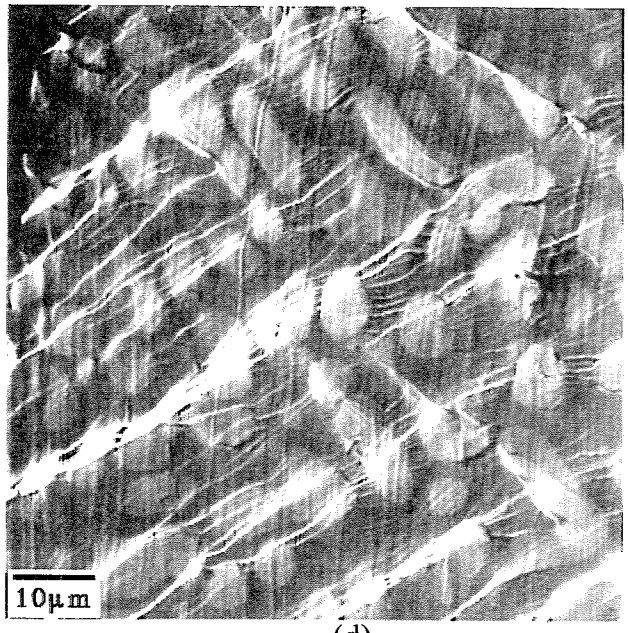

(d)

Fig. 3.10. SEM images of bend test results. (a) view normal to bend direction, (b) tensile failure region of specimen, (C) compressive failure region, and (d) tensile failure region of shear band pattern array.

specimen after straining, shear bands can be seen traversing both the amorphous metal matrix phase and the ductile metal dendrite phase. The directions of the shear bands differ slightly in the two phases due to different mechanical properties and probably because of crystal orientation in the dendritic phase.

In some cast plates from Howmet Corporation with a faster cooling rate, plastic strain to failure in bending has been found to be about 5%. In such a composite, the shear bands are denser than in the composite material "C" with smaller and more widely spaced dendrites as shown on Fig. 3.11. It is estimated that in the "C" composite material about four to five percent of the volume is in shear bands, whereas in the "finer grained" Howmet "H" composite material the shear bands are two to five times denser. This means that there is a greater amount of deformed metal, and this is also shown by the higher strain to failure in the Howmet composite material.

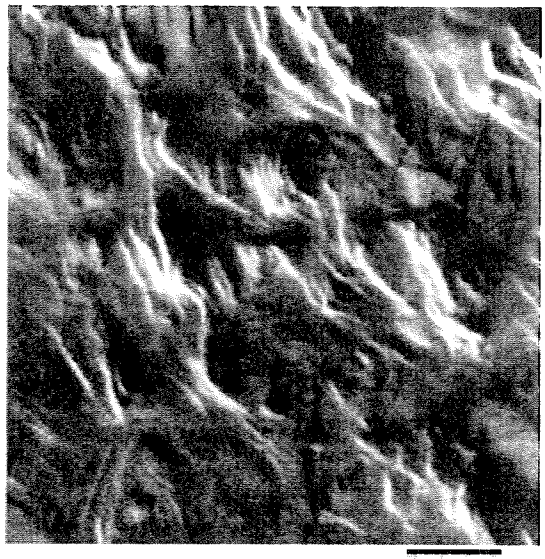

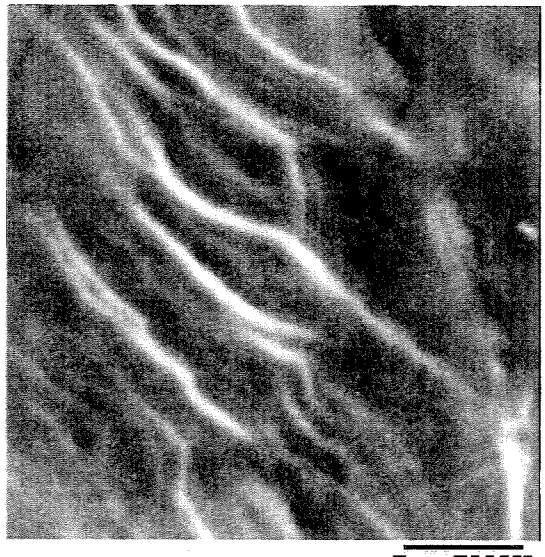

Fig. 3.11. SEM images of bend test results on Howmet composite material.

3.3.4 Charpy Impact test

Sub-standard size Charpy impact test specimens followed by the ASTM standard Designation E23-82 were machined from composite materials to have dynamic impact testing. The sub-standard sized Charpy specimen has a square cross section (5 x 5 mm) and contains a 45° V-notch, 1 mm depth with a 0.25 mm root radius. The specimen is supported as a beam in a horizontal position and loaded behind the notch by the impact of a heavy swing pendulum. The specimen is forced to bend and fracture at a high strain rate on the order of 10^3/sec.

Fig. 3.12 shows the composite fracture surface showing mixed fracture mode of I and II with distinct shear lips near the edges of the specimen under the dynamic loading condition of the Charpy test. The central region of the Charpy specimen is relatively flat corresponding to plane-strain, mode I fracture. High magnification images of the fracture surface show the classic veinlike fracture morphology characteristic of the monolithic glass mixed with regions of ductile fracture. The ductile regions have a characteristic "dimple" type of morphology, indicating the coalescence of microvoids. The average value of the angle between the slip plane and the loading axis was 45°. The higher energy absorption during fracture can be explained that deformation by shear band pattern formation is operant under the dynamic loading conditions of the Charpy test. One of the best composite materials shows sub-standard sized Charpy impact resistance of 24.0 J, which is higher by a factor of 3 than the test result for Vit1 (8.0 J). Fig. 3.13 and Fig. 3.14 show the Charpy

impact test result of various composite materials including Vit1 material.

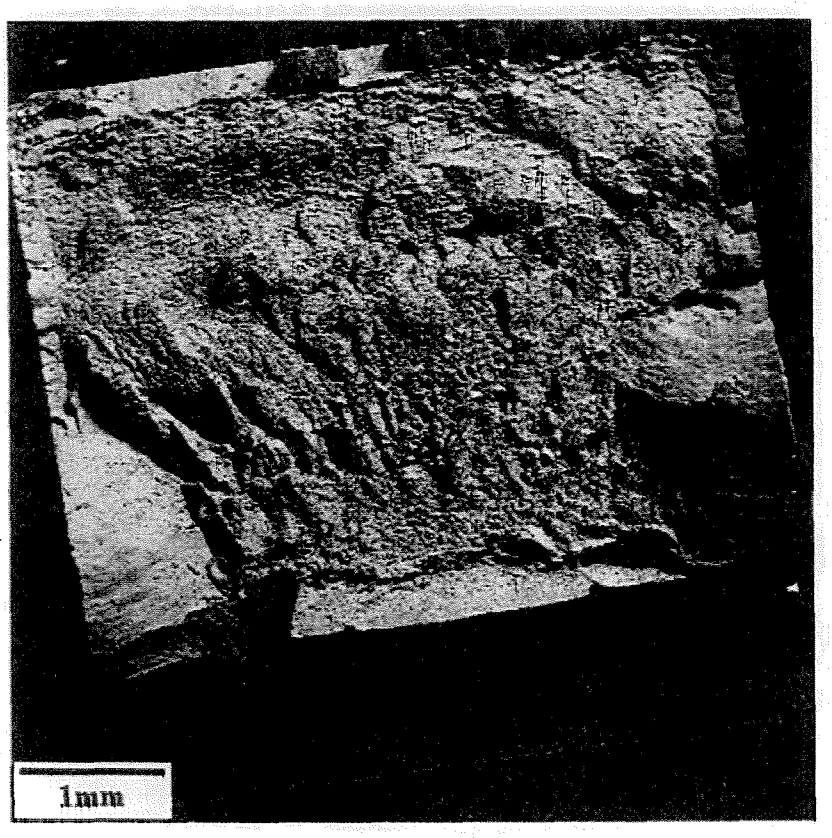

Fig. 3.12. SEM images of a composite after Charpy impact test. Distinct shear lips around the edges of the specimen can be found.

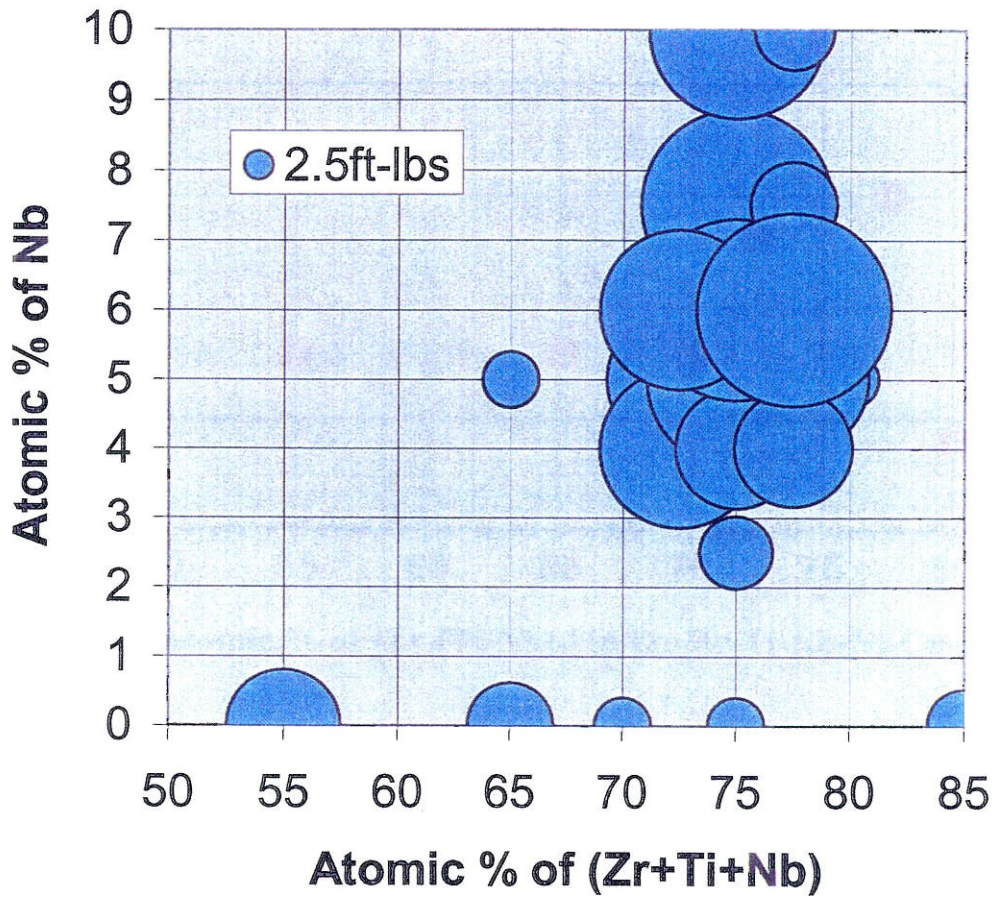

Fig. 3.13. Charpy impact test results of $(Zr_{75}Ti_{25-Z}Nb_Z)_{100-Y}\ X_Y$ alloy series. Z is the amount of Nb added, and Y is the ratio of X, ($Be_9Cu_5Ni_4$). The size of each bubble represents the Charpy impact toughness of each specimen.

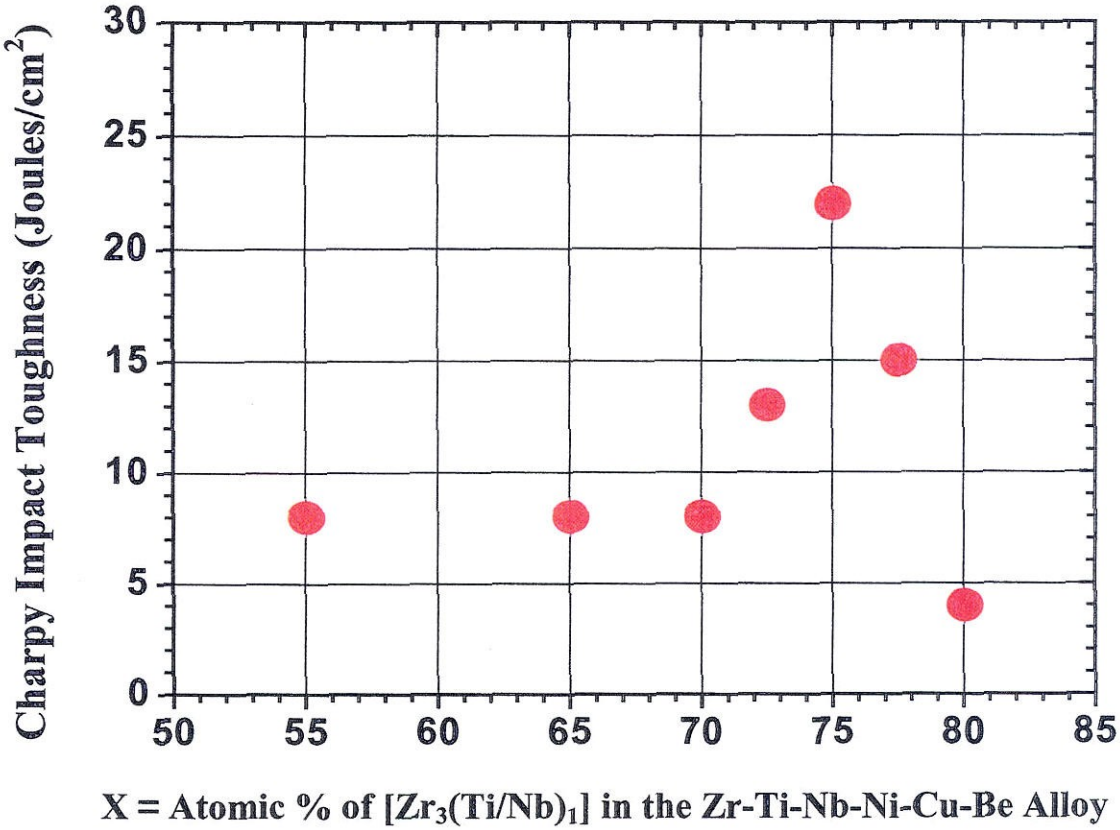

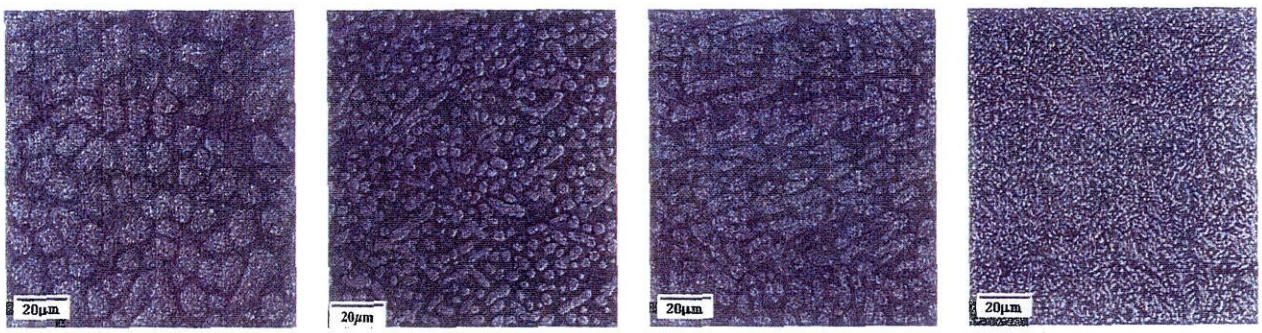

72.5/27.5 75/25 77.5/22.5 80/20

Fig. 3.14. Charpy impact test results of $(Zr_{75}Ti_{20}Nb_5)_{100-X}(Be_9Cu_5Ni_4)_X$ composite series and their microstructure. By changing the ratio of X, mechanical properties are changed dramatically.

The relative volume fraction of the β phase present in the *in situ* composite can be varied greatly by control of the chemical composition and the processing conditions. By varying the relative proportion of the early- and late-transition metal constituents, the resultant microstructure and mechanical behavior exhibited on mechanical loading can be change dramatically.

3.4 Discussion

The initiation and propagation of localized shear deformation in metallic glasses has been the subject of both theoretical and experimental investigations for a number of years.[16,17] It is generally accepted that the initiation of a shear band in a monolithic metallic glass is dictated by the local stress distribution and variations in the local yield condition arising from statistical fluctuations in the metallic glass structure which lead to heterogeneous and local initiation of slip. While dislocations have not been experimentally observed in metallic glasses, the variation in local free volume; i.e., density fluctuations, could induce local variations in stress distribution that serve to heteogeneously nucleate slip as discussed in the early work of J. C. M. Li.[18] Localization of shear during the evolution of deformation is also a natural instability which arises from the competition between strain hardening (or softening), strain-rate hardening, and thermal softening which accompanies local adiabatic heating. In metallic glasses, where models predict strain softening[19], and adiabatic heating produces dramatic thermal softening near the glass transition, one expects

shear localization be incipient and extreme, as is experimentally observed. Whether shear localization leads to failure is dictated by geometrical and loading constraints imposed on the propagation individual shear bands. The idea of shear band "confinement" in metallic glass composites was first addressed in the work by Courtney *et al.*, where thin metallic glass ribbons were sandwiched between thin brass plates.[20] Courtney argued that the confinement of shear bands in the glass layers by the ductile brass layers provided a mechanism for multiple shear banding and enhancement of plastic strain to failure under tensile loading.

In the new *in-situ* composite of this thesis, the dendritic microstructure of the β phase acts to seed the initiation of organized shear band patterns, confines the propagation of individual shear bands to domains having a spatial scale of the order of the primary dendrite axes length in the range of from 30 to 150 micrometer, and leading to a shear band spacing which is related to the dendrite secondary arms having a spacing between adjacent arms in the range of from 1 to 10 micrometers, more commonly in the order of about 6 to 8 micrometers. The size of and spacing between the dendritic arms of ductile crystalline phase preferably produces a uniform distribution of shear bands having a width of the shear bands in the range of from about 100 to 500 nanometers. Typically, the shear bands involve at least about four volume percent of the composite material before the composite fails in strain. Small spacing is desirable between shear bands since ductility correlates to the volume of material within the shear bands. Thus, it is preferred that there be a spacing between

shear bands when the material is strained to failure in the range of from about 1 to 10 micrometers.

A natural variation of the local condition for slip initiation is imposed by the dendritic microstructure which then results in formation of the shear band arrays. The heterogeneous variation of the local yield condition and local stress fields created either by difference in elastic properties of the β phase and the matrix, or by difference in yield criteria of the two phases and transfer of stress during yielding of the β phase replaces the image potentials of the 1D case or the 2D thin brass plates of the Courtney experiments. From the observed shear band width W = 0.3 - 0.5 μm, the pattern spacing $\lambda = 6 - 7$ μm, and the observation that the total slip across a band, S, is roughly equal to W (total strain within a shear band is of order unity) , we can estimate the global plastic strain arising from the shear band patterns to be , $W/\lambda = 1/20 = 5\%$ in excellent agreement with the "global" plastic strain observed in the various mechanical tests above.

Also, it is desirable that the crystalline phase has a modulus of elasticity approximately the same as the modulus of elasticity of the amorphous metal. This assures a reasonably uniform distribution of the shear bands. If the modulus of the particles is too high, the interface between the particles and amorphous matrix has a high stress differential and may fail in shear. Particles with high modulus can break out of the matrix when the composite is strained.

The volumetric proportion of the ductile metal particles in the amorphous

matrix is also significant. The ductile particles are preferably in the range of from 15 to 35 volume percent for the best improvements in mechanical properties. When the volume fraction of ductile crystalline metal phase is low, the effects on properties are minimal and little improvement over the properties of the amorphous metal phase may be found. On the other hand, when the volume fraction of the second phase is large, its properties dominate and the valuable assets of the amorphous phase are unduly diminished.

It is noteworthy that the matrix/dendrite interface in the present composites is atomically sharp, intimate, and apparently strong. This is evident from the fact that most interfaces remain intact during loading and yielding. This allows effective transfer of stress from the β-phase to the amorphous matrix when yielding occurs initially in the β-phase and may play a key role in seeding the formation of multiple shear bands. In crystalline composite materials it is well known that shear localization can have microstructural or thermal origins.[21] The thermal and/or mechanical coupling between phases provides a driving force for shear localization, and thus promotes the formation of shear bands at specific microstructural sites. The ductile phase in the new in-situ composite may have a dual role in the response to mechanical loading; they may serve as heterogeneous sites for the initiation of individual shear bands, while at the same time act as attraction or pinning centers during shear band propagation.

3.5 Conclusion

Earlier ductile metal reinforced bulk metallic glass matrix composite materials have not shown large improvements in the Charpy numbers or large plastic strains to failure in tension. This is due at least in part to the size and distribution of the secondary particles mechanically introduced into the bulk metallic glass matrix. The substantial improvements observed in the new *in situ* formed composite materials are manifest by the dendritic morphology, particle size, particle spacing, periodicity, interface homogeneity, and volumetric proportion of the ductile β phase controlled by chemical composition and/or processing conditions. This dendrite distribution leads to a confinement geometry that allows for the generation of a large shear band density, which in turn yields a large plastic strain within the material. The best improvements in mechanical properties of an *in situ* composite as compared with other metallic glasses, are achieved when the ductile crystalline phase distributed in the amorphous matrix has a natural strain limit above which a significant increase in stress is required for additional strain.

The present results for the *in situ* ductile phase/BMG matrix composite are unique and demonstrate a new physical phenomena which arises when the microstructural length scale (dendrite tip radius, arm spacing, etc.) and critical mechanical length scales (shear band width and spacing, etc.) are suitably chosen. The shear band pattern formation into regular arrays as controlled by the microstructure illustrates the cooperative interplay of the microstructure with the mechanism of mechanical deformation. This opens the possibility of producing an entirely new class

of high strength, tough, impact and fatigue resistant materials which combine the high strength of metallic glass with the ability to undergo plastic deformation under unconfined or otherwise unstable loading conditions.

References

1. A. Peker and W.L. Johnson, Appl. Phys. Lett. **63**,2342 (1993).
2. H.A. Bruck, T. Christman, A.J. Rosakis, and W.L. Johnson, Scripta Metallurgica Et Materialia. **30**(4),429 (1994).
3. H.A. Bruck, A.J. Rosakis, and W.L. Johnson, Journal of Materials Research. **11**(2),503 (1996).
4. C.J. Gilbert, R.O. Ritchie, and W.L. Johnson, Applied Physics Letters. **71**(4),476 (1997).
5. R.D. Conner, A.J. Rosakis, W.L. Johnson, and D.M. Owen, Scripta Materialia. **37**(9),1373 (1997).
6. P. Lowhaphandu, and J.J. Lewandowski, Scripta Materialia. **38**(12), 1811 (1998).
7. A.T. Alpas and J.D. Embury, Scripta Metallurgica. **22**(2),265 (1988).
8. H, Choi-Yim, and W.L. Johnson, Applied Physics Letters. **71**(26), 3808 (1997).
9. R.D. Conner, R.B. Dandliker, and W.L. Johnson, Acta Mater. **46**, 6089 (1998).
10. H, Choi-Yim, R. Busch, U. Koster, and W.L. Johnson, Acta Materialia. **47**(8), 2355 (1999).
11. A. Leonard, L.Q. Xing, M. Heilmaier, A. Gebert, J. Eckert, and L. Schultz, Noanstruct. Mater. **10**, 805 (1998).
12. C.C. Hays, C.P. Kim, and W.L. Johnson, Physical Review Letters. **84**(13), 2901 (2000).
13. C.P. Kim, F. Szuecs, and W.L. Johnson, accepted for publication in Journal of Metastable and Nanocrystalline Materials, 2000.

14. L.E. Malvern, Introduction to the Mechanics of a Continuous Medium, Prentice-Hall Inc., Englewood Cliffs, NJ (1969).

15. Donovan, Acta Metall. **37**(2), 445(1989).

16. F. Spaepen and D. Turnbull, Scripta Metall. **8**, 563 (1974).

17. J.J. Gilman, J. Appl. Phys, **46**, 1625 (1975).

18. J.C.M. Li, in Metallic Glasses, Proceedings of the Materials Science Division of the American Society for Metals (American Society for Metals, Metals Park, OH, 1976).

19. S. Schneider, W.L. Johnson, and P. Thiyagarajan, Appl. Phys. Lett. **68**, 493 (1996).

20. Y. Ling and T.H. Courtney, Met. Trans A. **21**, 2159 (1990).

21. M.A. Meyers. J. de Physique. **4** C8, 597 (1994).

Chapter 4. TEM Study

4.1 Introduction

In situ straining transmission electron microscopy (TEM) experiments were performed in collaboration with Dr. Evgenia Pekarskaya to study the propagation of the shear bands in the $Zr_{56.3}Ti_{13.8}Cu_{6.9}Ni_{5.6}Nb_{5.0}Be_{12.5}$ bulk metallic glass based composite. Contrast in TEM images produced by shear bands in metallic glass and quantitative parameters of the shear bands are analyzed.

A new class of materials emerged with the discovery of the multicomponent systems with exceptional glass forming ability, which made possible the synthesis of metallic glasses at large thicknesses.[1,2] Two regimes of plastic deformation have been observed, viscous or homogeneous deformation, which occurs at high temperatures and low strain rates, and inhomogeneous flow at low temperatures and high strain rates.[3] Inhomogeneous deformation manifests itself in the formation of shear bands at a 45 degree angle with respect to the applied stress in uniaxial loading. Deformation mechanisms of metallic glasses attracted a lot of attention from both theoretical and experimental sides.[e.g., 3-9] It is believed that changes in the chemical short-range order and increase of free volume occurs within the shear bands. Most of the experimental work, however, was done using scanning electron microscopy (SEM). TEM studies of shear bands were not very successful so far due to the relatively small structural changes in the shear bands, frequently undetectable by TEM. The most successful approach in studying shear bands in metallic glasses turned out to be *in situ*

straining experiments or deformation of thin films of material without successive thinning.[10,11] Propagation of a shear band in a thin film creates a step at the surface and changes the mass-thickness contrast in the TEM in the region of the shear band.

This chapter describes the TEM analysis of shear bands in a two-phase composite material, $Zr_{56.3}Ti_{13.8}Cu_{6.9}Ni_{5.6}Nb_{5.0}Be_{12.5}$, which consists of amorphous and crystalline phases. Such multiphase materials and composites based on a glassy matrix were developed in attempt to improve ductility and toughness of metallic glasses.[12] The presence of the second phase particles of crystalline phase was found to hinder shear band propagation and promote formation of multiple shear bands.[13] The goal of our study was to understand the deformation mechanisms of such multiphase material using TEM.

4.2 Experimental

The specimens for TEM were prepared by ion milling the composite material processed by arc melting. *In-situ* straining (tensile) experiments were performed at the Center for Microanalysis of Materials in the University of Illinois at Urbana-Champaign. A JEOL 4000EX TEM operating at 300kV was used. The experiments were performed at room temperature. The test was interrupted several times in order to analyze the changes in the microstructure during different stages of deformation. In addition, a Philips EM430 TEM operating at 300 kV (at California Institute of Technology) was used to study the specimens after deformation.

4.3 Results and Discussion

4.3.1 Shear bands in metallic glass

The microstructure of the alloy prior to deformation is presented in Fig. 4.1. The alloy consists of the amorphous matrix and crystalline β phase, which forms dendritic structure. Most of the dendrites have a bcc structure with lattice parameters of 3.5 Å. Extra reflections in diffraction patterns indicate ordering (see inset in Fig. 4.1), as well as a "spotty" contrast, which most likely originates from the ordered domains.

During the *in situ* tensile tests, the failure of the specimens occurred in the direction normal to the applied stress. The specimens frequently failed mainly by cracking rather than by slip, which is a typical failure for thin films. A localized deformation was observed mainly in the vicinity and ahead of the cracks, where shear bands were formed.

Fig. 4.2 shows bright field TEM images of the shear bands which were formed at the edge of the specimen. Depending on the orientation of the shear direction with respect to the electron beam, the shear band appears either lighter (Fig. 4.2a) or darker (Fig. 4.2b) compared to the surrounding material.[12] Shear band branching frequently occurs, which can be seen in Fig. 4.2.

In most cases in the present study, dark field imaging of the shear bands, with the objective aperture centered on the first halo, produced very faint, almost undetectable contrast. Therefore, in the present work, analysis of shear bands was

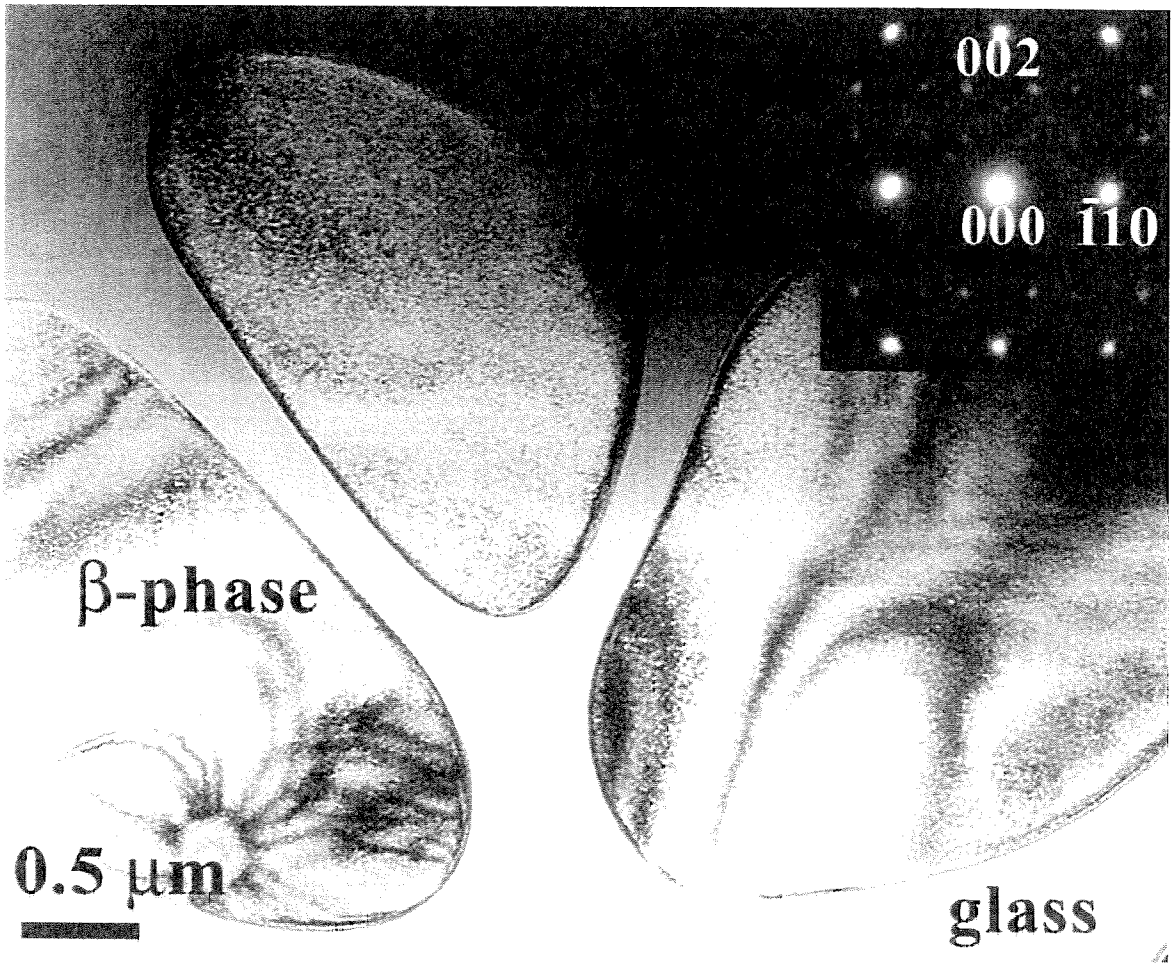

Fig. 4.1. Bright field image of the composite material. Diffraction pattern in the inset is a [110] zone axis of the β phase. Extra reflections indicate ordering.

(a)

(b)

Fig. 4.2. Bright field images of the shear bands formed during *in situ* deformation at the edge of the specimen; (a) and (b) represent the same area of the specimen at different tilt angles. Shear band branching is indicated by arrows.

done mainly using bright field imaging conditions. This contradicts the observations made by Donovan et al.[10] and Glezer et al.[11], who found that the contrast from shear bands in the dark field images was more pronounced.

The changes in the microstructure can sometimes be detected in the shear bands in the glassy phase. Fig. 4.3a shows a crack propagating in the glassy matrix. At the tip of the crack and crack branches, as well as in the narrow region around the crack, a sheared region can be observed, represented by a lighter contrast compared to the rest of the material. A magnified bright field image in Fig. 4.3b shows a less dense structure in the shear band compared to the undeformed material. In the dark field images with the objective aperture centered on the first halo (Fig. 4.3c), the shear band appears dark which means that this region is thinner compared to the surrounding material (less scattered electrons). No noticeable changes could be detected in the electron diffraction patterns, probably due to the fact that the diffraction patterns with the available selected area apertures give combined information from the deformed and undeformed regions. Nonetheless, the bright field and dark field images suggest the reduction in density/thickness of the material in the shear band.

Shear bands frequently change their "plane," which results in the change of the contrast from light to dark. The thickness of the shear band which is defined as the dimension in the direction orthogonal to the slip "plane," where as the width is the size of the shear band in the shear "plane," can be measured at the point at which the shear band is oriented edge-on.[11] It should be noted that only the width of shear bands

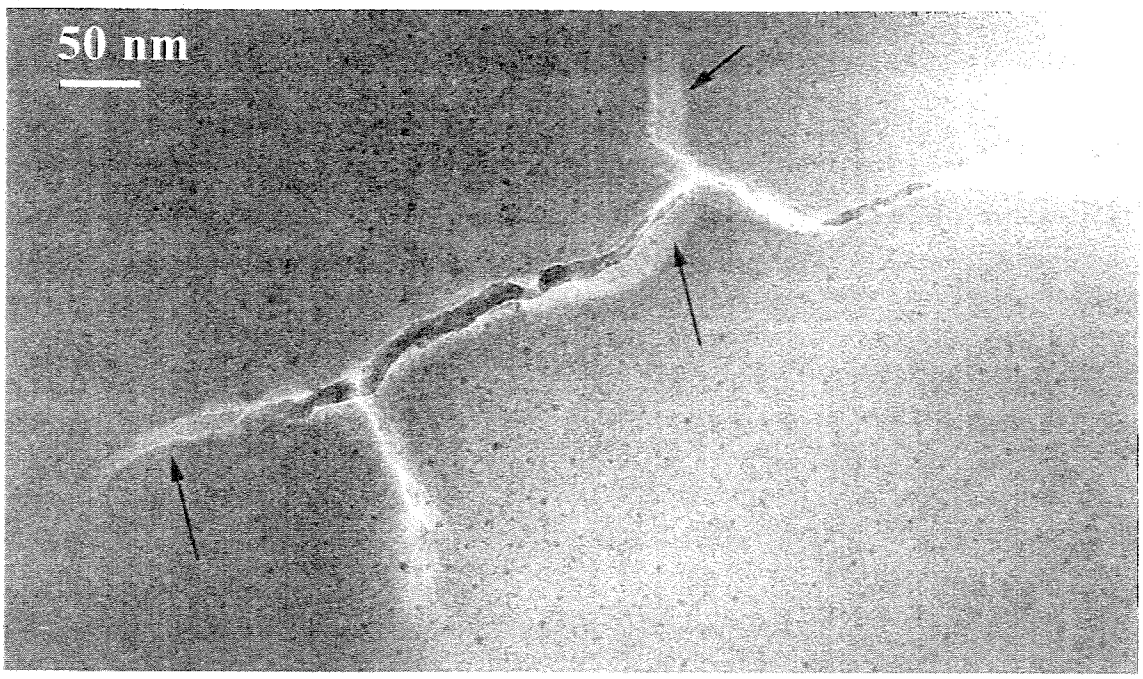

(a)

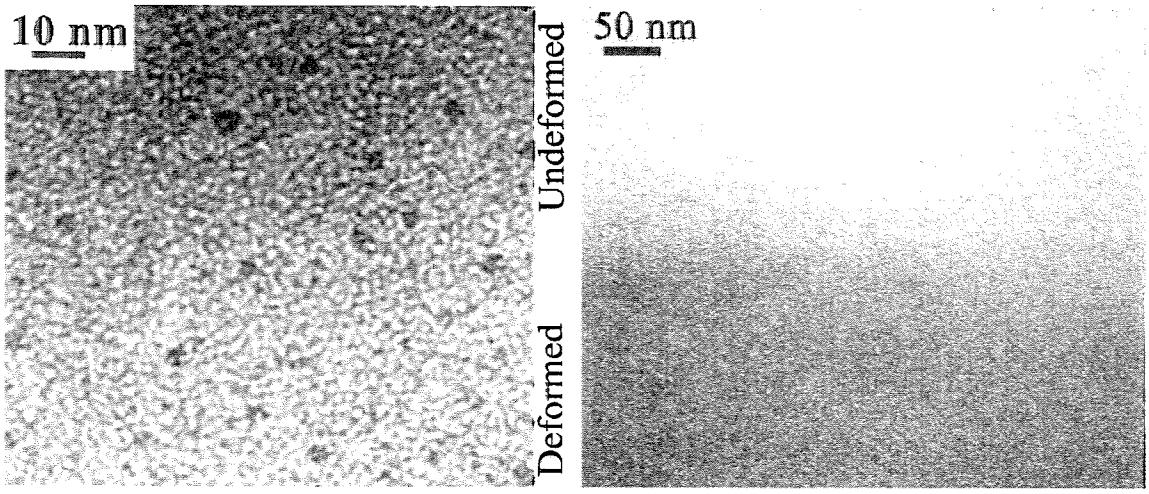

(b) (c)

Fig. 4.3. (a) Crack propagating in the glassy phase. Shear bands can be observed at the tip of the crack, indicated by arrows. Magnified bright field (b) and dark field (c) images show the structure in the deformed and undeformed regions of the material.

is possible to measure from the SEM images, whereas TEM enables measurements of the other dimension. This is illustrated in Fig. 4.4. Two shear bands can be seen in this image formed in the glassy phase, acting as stress concentrators at the glass/crystal interface. The point, where the shear band is "edge-on" is indicated by the arrowhead. The maximum thickness of the shear bands, measured this way in TEM, do not exceed 10 nm. Donovan and Stobbs also reported 10 and 20 nm thickness of shear bands formed in $Fe_{40}Ni_{40}B_{20}$ metallic glass.[10] The projected width of shear bands that are formed during our *in situ* experiments is around 120 - 200 nm. These are slightly smaller values than that obtained from the SEM images (around 200-300 nm). However, it should be borne in mind that the parameters of shear bands can be effected by the thickness of the deformed material. Also, in cases when shear bands are not parallel to the specimen surface, we can measure only the projected width of the shear band and this is determined by the specimen thickness.

4.3.2 Slip transfer between the glassy and the crystalline phases

An interaction of the shear bands with the β-phase dendrites is illustrated in Fig. 4.5. In the top left corner of the micrograph a crack is visible, which was formed along the path of the shear band, as shown by video recording of the straining experiments. Crack (as well as the shear band) changes its mode to a shear at a 45 degree angle and terminates. The second shear band and crack is formed ahead of the first crack at a 45 degree angle. A very interesting phenomenon can be observed here,

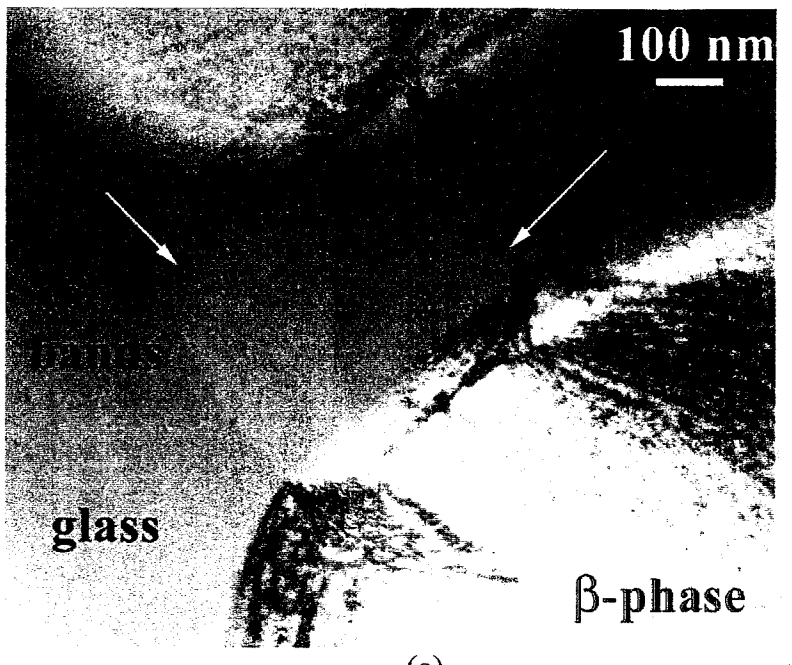

(a)

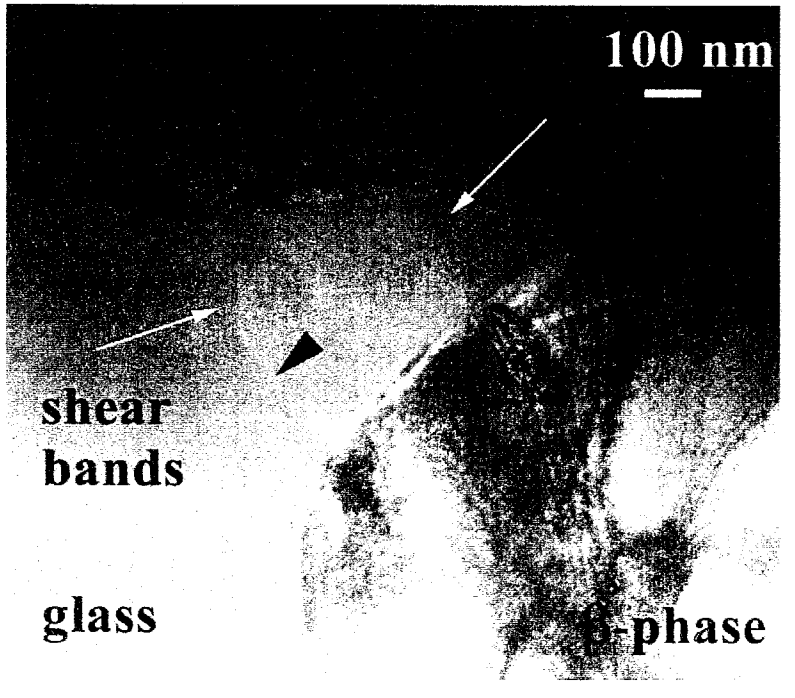

(b)

Fig. 4.4. TEM images of the same area at different tilt angles, illustrating changes in the shear band contrast. Shear bands are indicated by white arrows. The point where the shear band is in the "edge-on" position is marked by the black arrowhead (b).

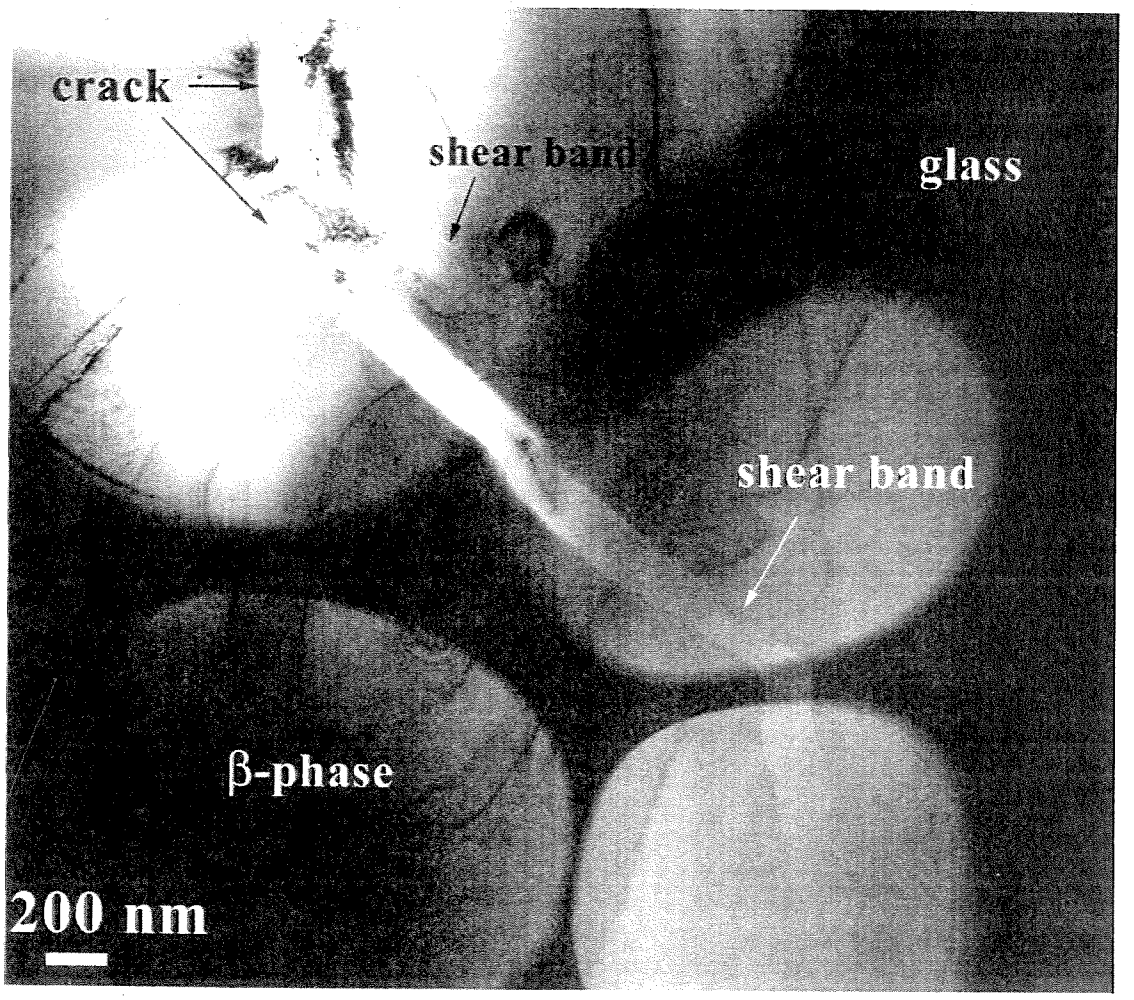

Fig. 4.5. TEM images of the shear band propagating through the two-phase region. Localization of deformation is observed in the β phase.

namely localization of the deformation in the crystalline phase, evidently imposed by the geometry of slip in the amorphous matrix. This result is in an excellent agreement with the SEM analysis of shear bands in this alloy, which suggested the localization of deformation in the crystalline dendrites.[12]

Tilting experiments revealed that dislocations are responsible for the localized deformation in the crystalline phase. This is illustrated in Fig. 4.6, where dislocations formed in the shear band in the β-phase can be observed. Analysis of Burgers vectors suggests that they are of <111> type.

However, localization of deformation in the β-phase occurs only at a large amount of shear in the amorphous phase. Small amount of shear leads to the delocalization of deformation in the crystalline phase. The later is shown in Fig. 4.7, where shear bands are formed in the region of the crack tip. Slip transfer from the amorphous matrix to the crystalline phase results in the formation of dislocations in the β-phase, which are not confined to a band.

4.3.3 Amount of Shear

When the individual dislocations can be easily resolved in the deformed region of the β-phase (e.g., Fig. 4.7), it is possible to estimate the amount of shear produced. The magnitude of shear is equal to (n * b), where n is the number of dislocations formed due to the slip transfer from the glassy phase to the β-phase and b is a Burgers vector of the dislocations. In cases such as in Fig. 4.7, it gives us the value of about

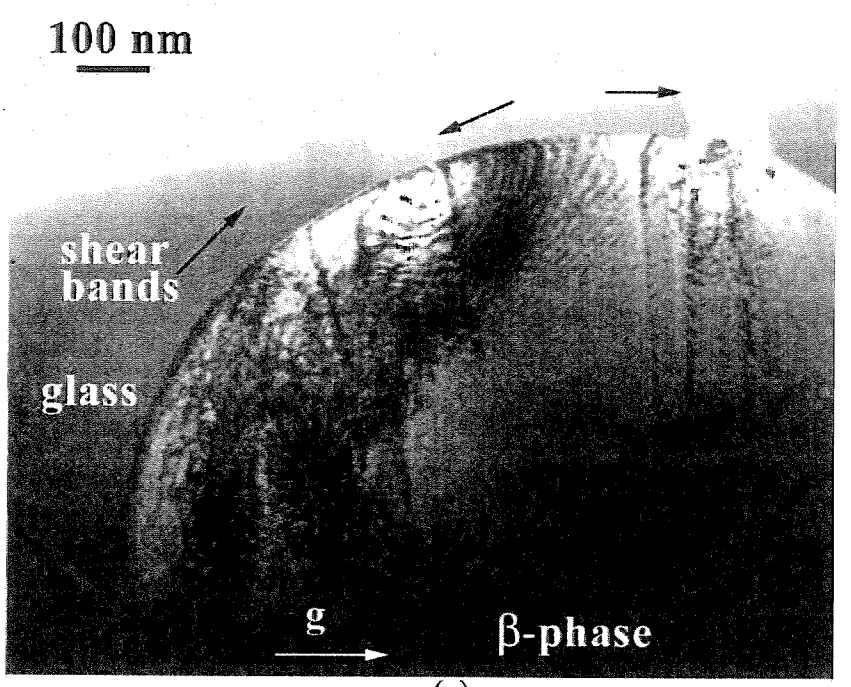

(a)

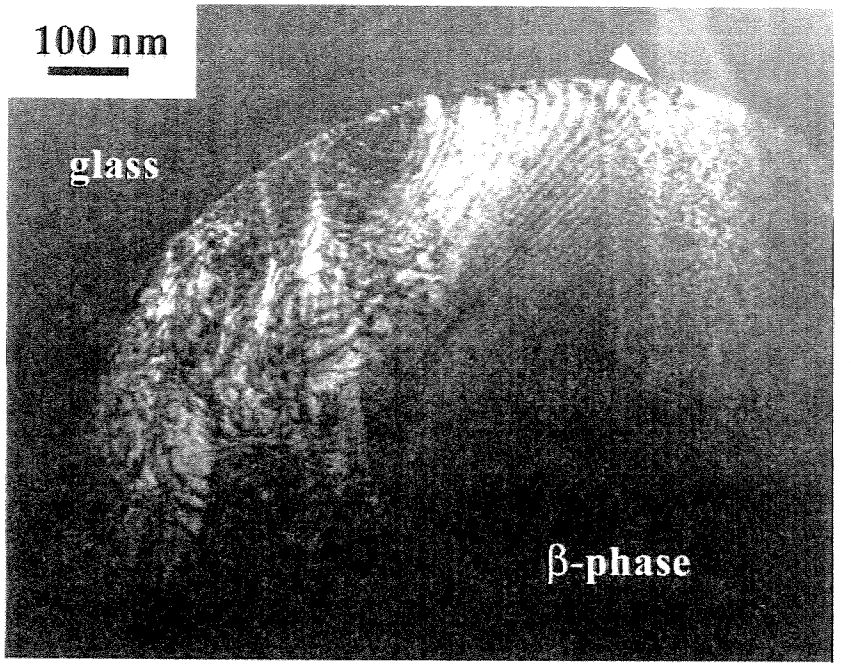

(b)

Fig. 4.6. (a) Bright field and (b) dark field (g=110) images, illustrating the slip transfer across the interface in the bulk metallic glass based composite. Shear bands are indicated by arrows in (a). A shear offset, marked by the arrowhead in (b), is visible at the glass/crystal interface.

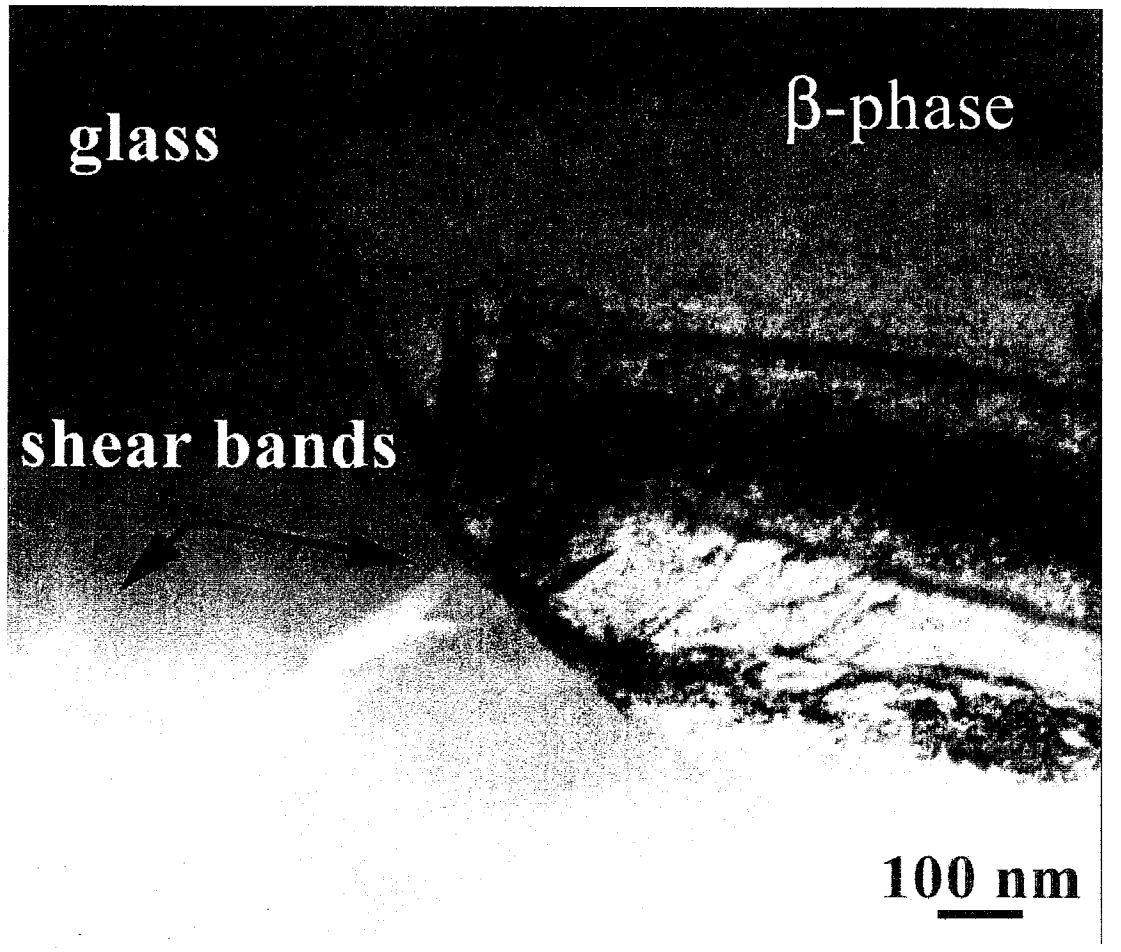

Fig. 4.7. TEM micrograph illustrating delocalization of deformation in the β phase at small amount of shear in the glass.

4 nm. Such cases are associated with the delocalization of deformation in the crystalline phase.

The magnitude of shear can be also measured by the shear displacement at the interface, when the direction of shear does not coincide with the electron beam. An example of such offset produced by the shear bands can be seen in Fig. 4.2 and Fig. 4.6, where much stronger localization of deformation is observed. These measurements give the value of 20-50 nm, which is lager than that obtained above from the dislocation analysis in the β-phase.

Analysis of the contrast produced by shear bands in TEM images (strong or faint) and the degree of localization of deformation in the β phase in these two cases support this result. The larger the amount of shear in the glass the more pronounced is the localization of deformation in the crystalline phase. The localization of deformation in the β-phase in the latter cases supports the larger magnitude of shear, compared to the cases where separate dislocations can be resolved in the shear band. Therefore, we can estimate a threshold value of the shear for the localization of deformation to occur in the β-phase, which is around 10 nm.

Measurements of the shear offsets using SEM images give larger values, from 500 nm[12] up to 2 μm[5]. Also, the shear displacements, that we measured in TEM in the specimens deformed in a bulk form, is around 150 nm. This result again indicates the influence of the film thickness on the dimensions of the shear bands.

4.4 Summary

TEM studies of shear bands formed during *in situ* straining in a two phase composite, based on a bulk metallic glass, are presented. Contrast produced by the shear bands was found to be more pronounced in the bright field images rather than in the dark field. It has been observed that a shear band path is not confined to one "Plane." The shear bands are 120-200 nm wide and around 10 nm thick. Localization of deformation was observed in the crystalline β-phase, which is in an excellent agreement with the SEM analysis of shear bands in the same material. It is established that dislocations are responsible for the deformation of the β-phase.

References

1. A. Inoue, T. Zhang, and T. Masumoto, Mater. Trans. JIM **31**, 177 (1990).

2. A. Peker and W.L. Johnson, Appl. Phys. Lett. **63**, 2342 (1993).

3. A.S. Argon, J. Phys. Chem. Solids. **43** (10), 945 (1962).

4. F. Spaepen and D. Turnbull, Scripta Met. **8**, 563 (1974).

5. P.G. Zielinski and D.G. Ast, Phil. Mag. A **48** (5) 811 (1983).

6. E.D. Tabachnikova, P.Diko, V. Ocelik, and P. Duhaj, Solid State Phen. **35-36**, 569 (1994).

7. T.C. Hufnagel, P. El-Deiry, and R.P. Vinci, Scripta Mater. **43**, 1071 (2000).

8. P. Lowhaphandu, L.A. Ludrosky, S.L. Montgomery, and J.J. Lewandowski, Intermetallics. **8**, 487 (2000).

9. A. Inoue, Intermetallics. **8**, 455 (2000).

10. P.E. Donovan and W.M. Stobbs, Acta Met. **29**, 1419 (1981).

11. A.M. Glezer and B.V. Molotilov, "*Structure and mechanical properties of amorphous alloys*" (Metallurgiya, Moskva, Russia, 1992) p.90, in Russian.

12. C.C. Hays, C.P. Kim, and W. L. Johnson, Phys. Rev. Lett. **84**(13),2901 (2000).

13. R.D. Conner, R.B. Dandliker, and W.L. Johnson, Acta Mater. **46** (17),6089 (1998).